

CENTER FOR RADAR ASTRONOMY

12



STANFORD ELECTRONICS LABORATORIES
DEPARTMENT OF ELECTRICAL ENGINEERING
STANFORD UNIVERSITY · STANFORD, CA 94305

LEVEL II

SEL-79-022

ADA 078834

**REMOTE SENSING OF OCEAN SURFACE
CURRENT AND CURRENT SHEAR BY
HF BACKSCATTER RADAR**

by

Eng-Chong Ha

August 1979

DDC
RECEIVED
DEC 18 1979
E

DDC FILE COPY

Technical Report No. D415-1

Prepared under

Office of Naval Research
Contract N00014-75-C-0356

This document has been approved
for public release and sale; its
distribution is unlimited.

79 12 18 002

14 SU - SEL-79-022,
TR-D415-1

6 REMOTE SENSING OF OCEAN SURFACE CURRENT AND
CURRENT SHEAR BY HF BACKSCATTER RADAR.

12

by

10 Eng-Chong Ha

DDC
RECEIVED
DEC 21 1979
REGISTRY
E

11 August 1979

12 15φ

9 Technical Report, No. D415-1

Prepared under

Office of Naval Research
Contract N00014-75-C-0356
15

This document has been approved
for public release and its
distribution is unlimited.

Radioscience Laboratory
Stanford Electronics Laboratories
Stanford University Stanford, California

332 400 Gus

ABSTRACT

The Doppler spectrum of radar return from the sea at HF contains two narrow lines displaced upward and downward from the carrier frequency, resulting from backscatter off ocean surface waves moving toward and away from the radar, respectively. These Bragg lines indicate resonant backscatter which occurs for the ocean waves of length one-half the radio wavelength. The phase velocity of these gravity waves consists of two components; the first is determined by the wavelength and the second by the current component in the direction of wave propagation averaged over depth with an exponential weighting function that has a characteristic scale proportional to the wavelength. The Doppler shift of the radar carrier is determined by the wave phase velocity. Its variation with carrier frequency is thus related to the vertical profile of the current component in the radar direction by a Laplace transform; therein lies the principle of radio measurement of ocean current and its vertical shear.

Radio backscatter experiments to verify the feasibility of such measurements were conducted ~~at Pescadero on the California coast,~~ using the ^aStanford Radar operating at four frequencies covering the range from 3 to 30 MHz. The depth-averaged radial current deduced from the centroid of the Doppler-shifted sea echo ~~in the January 1978~~ experiments at 6.8, 13.3, 21.7, and 29.8 MHz showed fluctuations on the order of 1 cm/sec superimposed on temporal trends that reached maximum values of ^{about} ~40 cm/sec. Concurrent in-situ measurements were obtained by tracking spar buoys ^{→ next para!} 1, 3, 6, and 12 m long, using a microwave ranging system. Both radar- and buoy-inferred currents agree generally in their variation with time and depth; the discrepancy between them was no larger than the difference in the currents measured by buoys deployed at different locations within the same range cell, typically from a few to 10 cm/sec. Inversion of the Laplace transform relating the radar-inferred Doppler velocity as a function of frequency to the vertical profile of the current is achieved numerically by seeking a solution that simultaneously minimizes a mean-square error and a mean-square deviation from an initial estimate. Two estimators of Bragg-line width based on the area of the spectral curve and the second moment about its centroid, respectively, are applied to

over 100 hours of radar data. The observed width in units of current is found to vary in inverse proportion to frequency raised to a power of approximately 0.4. Its dependence on pulse width, range, and wind conditions is significantly weaker.

→ It is concluded that multifrequency backscatter ground-wave radar at HF constitutes a powerful technique for mapping current and its vertical profile in the top few meters of the ocean. Measurement resolution of a few centimeters per second is attainable with a coherent integration time of ~15 minutes. Large areas of the ocean surface can be scanned by range gating and beam forming, with grid resolution on the order of kilometers.

Accession For	
NTIS <input checked="" type="checkbox"/>	
DDC TAB	
Unannounced	
Justification	
By _____	
Distribution	
Availability	
Dist.	Availability
A	special

CONTENTS

	<u>Page</u>
I. INTRODUCTION	1
A. Motivation	1
B. Historical Background	2
C. Contributions	3
D. Organization	4
II. PHASE VELOCITY OF FIRST-ORDER OCEAN GRAVITY WAVES IN THE PRESENCE OF OCEAN CURRENTS WITH VERTICAL SHEAR	7
A. Derivation of the Orr-Sommerfeld Equation	9
B. Boundary Conditions at the Free Surface	13
C. Wave Phase Velocity Determined from Solutions of the Orr-Sommerfeld Equation	15
D. Summary	22
III. STATISTICAL DESCRIPTION OF OCEAN WAVES	25
A. Practical Spectral Estimation	26
B. Relationships among Various Power Spectra Used by Radio Oceanographers	28
IV. THEORETICAL STUDIES OF FIRST-ORDER BACKSCATTER FROM OCEAN SURFACE WAVES OF DECAMETER WAVELENGTH	37
A. Physical Theory of First-Order HF Backscatter	38
B. First-Order Doppler Spectrum	44
1. Effects of Finite Coherent Length of Long-Crested Waves	46
2. Higher Order Ocean-Wave Interactions	46
V. PESCADERO EXPERIMENTS	49
A. Stanford Four-Frequency Radar	49
B. Data Reduction	55
C. System-Introduced Artifacts	59
1. Effects of Transmit-Antenna Motion	59
2. Local-Oscillator Instability	61
3. Nonlinear Amplification	63
4. Finite Range-Cell Size	64

CONTENTS (Cont)

	<u>Page</u>
D. In-Situ Measurements of Ocean Current by Spar Buoy	64
VI. DETERMINATION OF AVERAGED OCEAN CURRENT FROM DOPPLER SPECTRA	69
A. Estimator of Current-Induced Doppler Velocity	70
B. Statistical Analysis of the Doppler-Velocity Estimator	70
C. Experimental Results and Interpretations	75
VII. ESTIMATION OF DRIFT PROFILE FROM CURRENT-INDUCED DOPPLER VELOCITIES	83
A. Comparisons between Radar-Inferred Drift Profile and In-Situ Drift Measurements for Logarithmic Profile	84
1. Resolution Limitations	86
2. Statistical Uncertainties	87
B. Estimate of Friction Velocity U_*	90
C. Drift-Profile Estimation from Numerical Inversion	91
1. Reduction to Gaussian Quadratures	91
2. Direct Inversion and the Instability Problem	96
3. Stabilized Inversion	97
VIII. BANDWIDTH OF THE BRAGG SIGNAL	107
A. Bandwidth Estimators	107
B. Determination of First-Order Region	108
C. Results	109
1. Dependence on Wind Conditions (First Data Set)	113
2. Dependence on Radar Pulse Width (First Data Set)	114
3. Dependence on Range from Radar (First Data Set)	114
4. Dependence on Radar Frequency	114
5. Correlation with Radar-Inferred Current (Second Data Set)	115

CONTENTS (Cont)

	<u>Page</u>
6. Correlation with Width Estimated from In-Situ Current Measurements (Second Data Set)	115
D. Summary	117
IX. CONCLUSIONS AND RECOMMENDATIONS	119
A. Conclusions	119
B. Recommendations	120
Appendix A. DEGREE OF FREEDOM OF HAMMING-WINDOWED SPECTRAL ESTIMATOR	123
Appendix B. SPAR-BUOY DRIFT IN A CURRENT THAT VARIES WITH DEPTH	125
Appendix C. PARSEVAL'S THEOREM AND ITS EXTENSIONS	127
Appendix D. RELATIONSHIP BETWEEN THE WINDOWED TRANS- FORMS OF A FUNCTION AND ITS DERIVATIVE	129
BIBLIOGRAPHY	131

TABLES

<u>Number</u>	<u>Page</u>
5.1 Characteristics of Bragg-selected ocean waves	54
7.1 Comparison of numerical-integration results obtained by Gaussian quadrature and exact calculations	95
7.2 Examples of instability in direct inversion	97
8.1 Normalized widths of Bragg lines	113
8.2 Comparison of width Δ_C estimated from beamwidth effect (uniform current is assumed) and width \bar{w}_C estimated from radar data (third range cell, 19 January 1978)	116

ILLUSTRATIONS

<u>Figure</u>	<u>Page</u>
2.1 Geometry of wave/current interactions	8
2.2 Sea surface in the plane of wave propagation	14
3.1 Magnitude squared of filter function vs normalized frequency fT_a	28
3.2 Directional wave-height spectrum $S_{r1}(k)$ for ideal sea conditions	32
3.3 Directional wave-height spectra for ideal sea conditions	33
3.4 Directional wave-height spectrum $S_o(k)$ for ideal sea conditions	34
3.5 Comparisons of various wave-height directional spectra	35
4.1 Radar illumination of the ocean surface	37
4.2 Definition of the coordinate system	39
4.3 Integration zones	42
4.4 Theoretical Doppler spectra of radar return	44
5.1 Measured 3 dB full width of composite antenna beam vs radar operating frequencies	51
5.2 Propagation paths over land	51
5.3 Timing sequence of the radar	51
5.4 Receiver system for the Stanford four-frequency radar	52
5.5 Smoothed Doppler spectra at four radar frequen- cies and four range cells	58
5.6 Retrieval of first-order signal from Doppler spectrum of sea echo	59
5.7 Fine-scale structures of receding and approaching Bragg lines	62
5.8 Locations of spar buoys and range stations	65

ILLUSTRATIONS (Cont)

<u>Figure</u>	<u>Page</u>
6.1 Radar-inferred depth-averaged current at four range cells vs time during 19 January 1978	76
6.2 Radar-inferred depth-averaged current at four range cells vs time during 20 January 1978	77
6.3 Radar-inferred depth-averaged current at four range cells vs time during 24 January 1978	78
6.4 Radar-inferred depth-averaged current at four range cells vs time during 25 January 1978	79
7.1 Comparison of radar-inferred drift and spar-buoy drift (cluster 2) obtained on 19 January 1978	85
7.2 Comparison of radar-inferred drift and spar-buoy drift (cluster 1) obtained on 24 January 1978	86
7.3 Comparison of radar-inferred drift and spar-buoy drift (cluster 1) obtained on 25 January 1978	87
7.4 Comparison of radar-inferred drift and spar-buoy drift (cluster 1) obtained on 27 January 1978	88
7.5 Variance in drifts of spar buoys released in the same range cell	89
7.6 Logarithmic current shear measured by the four-frequency radar	90
7.7 Inversion of simulated Doppler data, linear profile assumed in the initial estimates	101
7.8 Inversion of simulated Doppler data, logarithmic profile assumed in the initial estimates	102
7.9 Inversion of simulated Doppler data with 5 percent noise, logarithmic profile assumed in the initial estimates	103
7.10 Inversion of radar Doppler-velocity data averaged over time	104
8.1 Locations of anemometers	111
8.2 Wind-direction classifications	114
8.3 Backscatter geometry	115

SYMBOLS

a	arbitrary constant
a_i	wind speed classified in four categories
$A(\underline{k}, \omega)$	ocean-wave component at wave number \underline{k} and radian frequency ω
B_+, B_-	amplitudes of waves propagating toward and away from the radar
c	speed of light in free space; phase velocity of gravity waves
c_0	phase velocity of gravity waves in the absence of current
$c^{(1)}$	phase-velocity contribution from current, to first order
c_j	current at probed depth $z(x_j)$ multiplied by weight w_j
$C_g(\)$	autocovariance function
$C(\)$	autocovariance function for homogeneous and stationary process
$d\underline{k}$	incremental wave number
dr	incremental distance along radial direction
dt	incremental time
dx, dy	incremental distances in x, y directions, respectively
$d\omega$	incremental radian frequency
$d\theta$	incremental angle
f	frequency
f_B	Bragg frequency
f_c	radar carrier frequency
f_i	$2\hat{U}/s_i$; one of four radar frequencies used; Doppler frequency at bin i
$f(x)$	arbitrary function of x
g	gravity (981 cm/sec^2)
$g(t)$	pulse envelope
$G(\theta)$	antenna directivity
H^2	mean-squared wave height

i	$\sqrt{-1}$; index
j	index
\underline{k}	wave-number vector of ocean surface wave
k	magnitude of \underline{k} ; index
k_x, k_y	x,y components of \underline{k}
k_0	normalizing wave number
K	von Karman's constant
l	index; length of spar buoy immersed in water
l^*	weighted scale length of vertical profile of current
L	ocean surface-wave wavelength
L_k	radar pulse width
L_x	radial extent of ocean patch illuminated by radar
L_y	azimuthal extent of ocean patch illuminated by radar
m	index
n	number of quadrature points
$P_{n-1}(x)$	polynomial of order $n-1$
$P(\underline{k}, \omega)$	power spectrum
P_m	power spectral value at frequency bin m
$P(t)$	power spectral value at time t
P_0	mean value of $P(t)$; hydrostatic pressure
P_1	wave-induced dynamic pressure
P_a	ambient atmospheric pressure
P_T	total pressure
$Q_i(x)$	sampling polynomial of order $n-1$
$\underline{r}, \underline{r}_1, \underline{r}_2$	horizontal position vectors
r	magnitude of \underline{r}
r_m	one of four discrete values of range of scattering surface from radar

r_0	range of scattering surface from radar
R	Reynolds number
$R_P(t)$	autocovariance function of the process $P(t)$
$R_U(t)$	autocovariance function of the process $U(t)$
$s(t)$	time series; received signal
\bar{s}	average value of $s(t)$
s_i	β_i/k_0
$s_n(t)$	n^{th} radar pulse transmitted
$\hat{S}(\)$	finite-time Fourier transform
$S(f)$	infinite-time Fourier transform
\bar{S}	average value of $S(f)$
S_{r1}, S_{r2}	ocean-wave directional spectra obtained by Rice
S_+, S_-	ocean-wave directional spectra obtained by Barrick
S_0	ocean-wave directional spectrum
t, t_1, t_2	time
t_u	correlation time of $U(t)$
t_p	correlation time of $P(t)$
T	coherent integration time
T_a	averaging interval
T_{DLY}	time delay measured from leading edge of transmit pulse
u	x component of \tilde{v}
U	magnitude of \underline{U}
U_c	current-induced Doppler velocity
U_*	friction velocity
\hat{U}	depth-averaged ocean current in radar direction
\underline{U}	horizontal current vector
U_x	current in x direction

U_{β}	current in direction toward radar
U_0	current at mean sea level
v	y component of \tilde{v}
\tilde{v}	wave-induced fluid velocity
v_T	fluid velocity
V_g	group velocity
w	z component of \tilde{v}
w_c	spectral width converted into cm/sec
\bar{w}_c	average width
\hat{w}_c	normalized width
w_i	weight for gaussian quadrature formula
$w(t)$	power spectral value normalized by its time average
w_1	second-moment spectral width
w_2	spectral area width
x	one of the horizontal coordinate axes
\hat{x}	unit vector in x direction
x_j	quadrature point
y	one of the horizontal coordinate axes
\hat{y}	unit vector in y direction
z	vertical coordinate
\hat{z}	unit vector in z direction
z_p	effective depth probed by radar, assuming logarithmic current profile
z_0	roughness scale
$z(x_j)$	depth probed as a result of gaussian quadrature formula

β	radio-wave wave number
δ_{ij}	Kronecker delta
$\delta(\)$	Dirac delta distribution
Δ	current-induced Doppler shift
$\underline{\varepsilon}$	noise vector
$\eta(x,y)$	surface wave height above mean sea level
η'	$\partial\eta/\partial r$
θ	angle off radar beam axis
λ	radio wavelength; Lagrange multiplier
π	3.1415927
ρ	density of water
σ_p^2	variance of $P(t)$
ω	radian frequency
∇	gradient operator
∇_x	curl operator

ACKNOWLEDGMENTS

I wish to express my sincere gratitude to Professor G. L. Tyler and Dr. C. C. Teague for their patient guidance, to Professors V. R. Eshleman and A. M. Peterson for their encouragement and comments, to all members of the Stanford Center for Radar Astronomy (SCRA) for their support, to Professor C. S. Williams for his thorough reading of this manuscript, to Dr. R. H. Stewart of the Scripps Institution of Oceanography (SIO) for his most useful criticisms throughout the course of this work, and to Dr. B. J. Lipa of SRI International and Dr. D. E. Barrick and Dr. B. L. Weber of the NOAA Wave Propagation Laboratory for their suggestions and advice. Discussions with my colleagues, especially Dr. C. D. Chang, Mr. B. Haugstad, and Mr. A. Elabdalla, have been of tremendous value to my intellectual growth in general and to this research in particular.

Experiments described in this work were the efforts of many members of SCRA and SIO. I would like to express my special appreciation to Professor H. T. Howard, Mr. W. Crosby, and Mr. W. Faulkerson for making the measurements possible. Special thanks go to Mr. F. Orabona for rendering my experience with the Sigma Five Computing Facility enjoyable and fruitful.

Careful editorial assistance by Hortense Shirley and the expert typing of the final draft by Inga Lof and the first draft by Irene Stratton are gratefully acknowledged. I wish to thank Wei-Yue for her moral support and patience that made these years enjoyable.

Financial support for this research was provided by the Office of Naval Research through Contract No. N00014-75-C-0356 and by the National Aeronautics and Space Administration through Grant No. NGL 05-020-014.

Chapter I

INTRODUCTION

A. Motivation

This research investigates the feasibility of remotely monitoring the ocean surface current and its vertical distribution using a four-frequency pulsed radar operating in the High-Frequency (HF) region of 3 to 30 MHz. Both the theoretical and experimental aspects of this remote-sensing technique will be studied in detail.

The term "current" as applied in this work refers to the bulk motion of the water mass in the ocean. This motion is generated, in part, by pressure and temperature differences and by tidal forces. It can also be caused by local wind blowing over the sea surface, with the direct effect of a wind-drag-generated shear current and the indirect effect of a wave-drag-generated Stokes current [Wu, 1975]. Shear current is expected to follow a logarithmic variation with depth, similar to the logarithmic wind profile immediately above the sea surface [Bye, 1965; Wu, 1975]. Stokes current is the result of nonlinearities in the dynamics of the wave, and it decreases exponentially with depth [Phillips, 1966].

Measurements of current in the upper layers of the ocean are important in the study of momentum and mass transfer across the air/sea interface, and these processes significantly influence the global weather pattern. Such measurements also have direct practical applications. For example, to minimize the adverse effects of oil spills, the direction and magnitude of the drift of these pollutants must be known. This drift is partly the result of the underlying ocean current. Actually, any particle that floats in the ocean waters will be advected by the bulk motion of the water masses; some important examples being fish larvae and food.

Conventional methods of current measurement rely on either moored current meters or drifters. In the first measurement, the fluid velocity at one fixed location is averaged over time which results in a Eulerian estimate. The second measurement is Lagrangian in nature because each drifter follows the mean drift of a group of water particles. When the current field is not uniform over the ocean surface, a large number of drifters or current meters must be deployed to obtain statistically

significant measurements. The hostile sea environment renders such operations extremely difficult.

In the radio method, a radar is employed, covering distances up to 40 km. The ocean surface waves act as tracers, and their advection by the underlying current is detectable by the radar. The radar-inferred current is thus Lagrangian in nature. Operating with narrow pulses and a small beam width, the spatial resolution of a given ocean-surface patch illuminated by the radar is approximately 10×10 km. By range gating, portions of the ocean surface at various radial distances from the radar can be examined simultaneously. Concurrent coverage in the azimuthal direction can be achieved by electronically steering the antenna beam formed by an antenna array. After being proven feasible, this radio-measurement technique can be of great utility to oceanographers.

B. Historical Background

Sea state here refers to ocean surface roughness. The ocean wave slope at a given wavelength is commonly used as a perturbation parameter in the analysis of both surface-wave dynamics and the scattering of radio waves from the sea surface.

Since Crombie [1955] first identified the physical mechanism responsible for the first-order HF sea echo, significant advances have been made in the use of HF radar for the remote sensing of sea state. A closed-form relation between the radar cross section and ocean wave-height spectrum has been developed theoretically on the basis of perturbation analysis [see, for example, Barrick, 1970; Barrick, 1972; Johnstone, 1975], and the first-order results have been experimentally verified [Barrick et al, 1974; Teague et al, 1975]. HF measurements of the wave-height directional spectrum by a synthetic-aperture technique [Tyler et al, 1974] and by inversion of the second-order Doppler spectrum [Barrick, 1977a; Lipa, 1978] compared favorably with in-situ buoy measurements. Mapping of wind fields in the ocean at long ranges (a few thousand kilometers) by means of the first-order Doppler spectrum has also proven possible [Long et al, 1973; Barnum et al, 1977].

Use of the first-order sea echo to probe the ocean-surface current depends on the fact that, in the absence of current, the echo Doppler

spectrum consists of narrow lines symmetrically displaced from the radar carrier frequency by a known amount. The observed small displacement of the Bragg lines from the known position is attributed to current and is referred to as current-induced Doppler frequency. Stewart and Joy [1974] derived an integral relation between this measured Doppler frequency at any radar frequency and the actual ocean-current distribution with depth. By simplifying the result to that for a linear current profile, they observed that the measured current-induced Doppler frequency was equivalent to that produced by uniform ocean bulk motion at a velocity equal to the actual current at a depth of approximately $1/24$ of the radio wavelength. Based on this result, they obtained favorable comparisons between radar-inferred ocean current and in-situ measurements by a parachute drogue.

Barrick et al [1976,1977b] described a current-mapping HF radar system that measures the depth-averaged ocean current at one radar frequency. They extended a novel approach of Crombie [1972] to measure the direction of signal arrival by comparing the phases of the signal on adjacent receiving antennas. This method eliminates the need for a large antenna array to obtain spatial resolution in the azimuthal direction. They have been able to produce two-dimensional maps of radar-inferred ocean current over a portion of the Gulf Stream [Barrick et al, 1977b] and at the lower Cook Inlet in Alaska [Barrick, 1978a].

C. Contributions

The major contributions of this investigation are as follows:

- critical examination of the perturbation approach used by Stewart and Joy [1974] to derive the ocean-wave dispersion relationship in the presence of a current that varies with depth; their first-order result is extended here to second order for an exponential drift profile
- derivation of the first-order Bragg-scatter theory for a pulsed monostatic radar, based on simple wave-propagation concepts, to demonstrate the current-measuring capability of backscatter radar and to investigate the limitations of the radar technique in a straightforward manner
- analysis of data collected at Pescadero on the California coast in January 1978, using a four-frequency HF backscatter

radar to produce ocean-current estimates with a consistency of a few centimeters per second, corresponding to an accuracy of typically a few percent

- deduction of the vertical profile of ocean current from the radar data at four frequencies and comparison to the profile estimated from in-situ drift measurements of spar buoys of four different lengths, assuming that the profile is logarithmic with depth; similar features in the deduced profiles have been observed
- development of a stabilized numerical inversion algorithm to obtain the vertical profile of ocean current from the Doppler velocity measurements at four frequencies without requiring the profile to be logarithmic in depth
- study of the behavior of the width of the Bragg lines based on over 100 hours of data collected at Pescadero, using a four-frequency HF backscatter radar, spanning a period of four years

D. Organization

Chapter II investigates the hydrodynamics of waves on an ocean current that varies with depth. The ocean-wave dispersion relation is derived, based on basic principles and the perturbation approach of Stewart and Joy [1974]. Their perturbation result is extended to second order for an exponential current profile.

The concept of ocean-wave spectra is discussed in Chapter III. Various definitions of the directional wave spectrum are examined and compared.

In Chapter IV, the first-order Bragg scatter theory is derived, based on simple wave-propagation concepts. The result is then used to consider the effects of an ocean current that exhibits horizontal and vertical variations.

Chapter V describes the Stanford four-frequency radar system and the signal-processing procedure involved in producing Doppler spectra from the radar data collected. A filtering scheme is developed to isolate the first-order Bragg signal from the second-order effects and system noise. Included is a discussion of possible system-introduced artifacts that are shown to have negligible effects on the data. In-situ current measurements obtained by drifters are also described.

The centroid estimator of the current-induced Doppler velocity is analyzed in Chapter VI. It is demonstrated that, under appropriate conditions, the estimator produces an unbiased and consistent measure of the ocean-current component in the direction of the radar averaged over depth and over the radar range cell. The temporal characteristics of the averaged current thus estimated will be examined from four days of data collected at Pescadero in January 1978.

The problem of recovering the actual current distribution with depth from the radar-inferred averaged current at the four radar frequencies is studied in Chapter VII. A logarithmic current profile is assumed to facilitate comparisons between the radar-inferred and buoy-inferred profiles. The instability problem in the numerical inversion of the integral equation needed to reconstruct the current profile from the radar-inferred depth-averaged current is then examined; an algorithm constructed to resolve this problem is computerized, and its performance is evaluated.

Chapter VIII presents the estimated bandwidths of the Bragg lines for the entire set of radar data obtained from May 1975 through January 1978. The behavior of the observed width as a function of radar frequency and pulsewidth, range from radar, and wind speed and direction is studied to achieve an understanding of the underlying causes of the finite Bragg width.

Chapter IX is a summary of the results of this work, and areas for future research are recommended.

Chapter II

PHASE VELOCITY OF FIRST-ORDER OCEAN GRAVITY WAVES IN THE PRESENCE OF OCEAN CURRENTS WITH VERTICAL SHEAR

As will be demonstrated in Chapter IV, HF radars can detect ocean surface waves having wavelengths from a few meters to a few tens of meters. The characteristics of these waves are not significantly controlled by capillary forces; their natural modes are determined only by gravity and, for this reason, they are called "gravity waves."

This investigation is concerned primarily with gravity waves whose average height h (the height from crest to trough) is small compared to their length L (crest-to-crest distance), especially those with longer wavelengths because waves over a few meters high are not frequently encountered. Ocean waves also break if h/L is larger than approximately $1/7$ [Kinsman, 1965]. The discussion in this chapter, therefore, is limited to first-order waves, and all terms higher than first order in h/L are neglected in the mathematical derivations to follow. Consequently, the resulting equations are linear in the wave-perturbed quantities so that the individual plane waves (called long-crested waves) can be considered. Only the effects of perturbations that have a single horizontal wave-number vector \underline{k} and one radian frequency ω need be investigated.

This analysis is limited to deep-water waves. Because the ocean depth is assumed to be much larger than the wavelength L of interest, the ocean bottom is considered to be infinitely far away from the air/sea interface.

The terms "fluid element" and "water particle" are used interchangeably. A fluid element is a volume element small enough to be considered a particle and is large enough to contain sufficient molecules so that the concepts of local density and local pressure are applicable.

Wind is one of the dominant forces that generates ocean waves. The emphasis of this study, however, is not focused on the wave-generation mechanisms but on the natural modes of gravity waves. On the other hand, understanding of the wind generation of waves depends on the measurements of relevant ocean parameters, among which is the wind-produced current shear in the upper layers of the ocean. A mean horizontal current $\underline{U}(z)$ is assumed to exist in the surface layers--produced by wind drag or

otherwise. Here, z is the positive vertical axis, where $z = 0$ represents the mean sea surface (see Fig. 2.1). It will be demonstrated in Section A that only the component of current in the direction of wave propagation will influence the wave phase velocity.

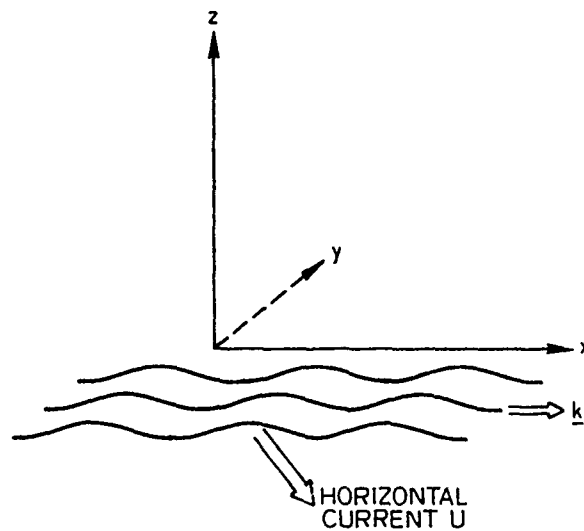


Fig. 2.1. GEOMETRY OF WAVE/CURRENT INTERACTIONS.

In the following calculations, \underline{U} is assumed to be constant in time t and in the horizontal coordinates (x,y) . The results obtained under this assumption are valid for a wave period short compared to the actual time scale of the ocean-current variation and for a wavelength small compared to the scale length of the ocean-current variation.

Viscous effects are neglected; they are important only when the Reynolds number R is comparable to or smaller than 50 ($R = UL/\nu$, where U is a representative fluid velocity, L is a representative spatial scale, and ν is the kinematic viscosity). For water, R is very large compared to unity in most flow systems of importance [Batchelor, 1970].

Based on the above assumptions, the expression for the ocean-wave phase velocity c is derived in the following section in terms of the wave number k and ocean current \underline{U} . Beginning with the equation of motion, the inviscid Orr-Sommerfeld equation for the vertical component

of the wave-induced fluid velocity will be derived. Boundary conditions at the free surface will be linearized, and then a solution is obtained for the case where the vertical profile of the ocean current is linear. The problem of relating the wave phase velocity to a general current profile is solved by a perturbation approach wherein the current profile is assumed to have a small vertical shear.

A. Derivation of the Orr-Sommerfeld Equation

The restoring forces on gravity-wave systems are pressure gradients and gravitational pull. The equation of motion for each water particle is

$$\frac{d}{dt} \underline{v}_T = - \frac{\nabla P_T}{\rho} - \nabla(gz) \quad (2.1)$$

where

\underline{v}_T = fluid velocity in an inertial frame

P_T = scalar pressure in the water

g = gravitational acceleration

ρ = water density

∇ = vector gradient

z = vertical Cartesian coordinate of the water particle

Note that these restoring forces are all irrotational. The equation of motion yields the following form when the curl of both sides is taken:

$$\nabla \times \left(\frac{d}{dt} \underline{v}_T \right) = 0 \quad (2.2)$$

Because \underline{v}_T describes the spatial velocity distribution in the water, acceleration of the particle is

$$\frac{d}{dt} \underline{v}_T = \frac{\partial}{\partial t} \underline{v}_T + (\underline{v}_T \cdot \nabla) \underline{v}_T \quad (2.3)$$

The second term results from acceleration caused by the migration of water particles to a region of higher fluid velocity.

The velocity field can be separated into two additive parts--a contribution \underline{U} that is time independent and a contribution $\underline{\tilde{v}}$ that is not; therefore,

$$\underline{v}_T = \underline{U} + \underline{\tilde{v}}$$

where \underline{U} is the time-averaged fluid velocity to be called ocean current or mean water drift. This discussion is also limited to ocean currents of such large horizontal scales that their local variations in the x, y directions are negligible and, as a result,

$$\underline{U}(x, y, z) = \underline{U}(z)$$

The remaining contribution $\underline{\tilde{v}}$ is the wave-induced perturbation in the fluid velocity decomposed into plane-wave components,

$$\underline{\tilde{v}} = \underline{\tilde{v}}_0(z) \exp[i(\underline{k} \cdot \underline{r} - \omega t)] \quad (2.4)$$

where

\underline{k} = horizontal wave-number vector of a specific plane wave

ω = radian frequency of the plane wave

\underline{r} = horizontal vector $x\hat{x} + y\hat{y}$, where \hat{x}, \hat{y} are the unit vectors in the x, y directions, respectively

$i = \sqrt{-1}$

Here, the averaged wave height is small compared to wavelength so that the terms in Eq. (2.2) of a higher order than $\underline{\tilde{v}}$ can be neglected. Because this assumption linearizes Eqs. (2.2) and (2.3), the plane-wave components can be considered individually.

In this section, the x coordinate axis is chosen to lie parallel to the direction of the ocean current and, assuming purely horizontal current,

$$\frac{d}{dt} \underline{v}_T = -i(\omega - \underline{k} \cdot \underline{U}) \underline{\tilde{v}} + \hat{x}w \frac{\partial}{\partial z} U \quad (2.5)$$

where u, v, w are the three Cartesian components of \tilde{v} . After some algebraic manipulation, the linearized version of Eq. (2.2) is

$$(\omega - \underline{k} \cdot \underline{U}) \nabla_x \tilde{v} = (-\hat{x}v + \hat{y}u) (\underline{k} \cdot \underline{U}') - i\hat{y}(wU'' + w'U') - \hat{z}(\underline{k} \cdot \hat{y}) wU' \quad (2.6)$$

where the primes indicate differentiation with respect to the vertical coordinate z . This vector equation contains three scalar components, and only two are independent. For convenience, the x and y components are chosen,

$$(\omega - k_x U) (ik_y w - v') + k_x U' v = 0 \quad (2.7a)$$

$$(\omega - k_x U) (u' - ik_x w) - k_x U' u + i(wU'' + w'U') = 0 \quad (2.7b)$$

where k_x, k_y are the components of \underline{k} in the x, y directions, respectively.

The continuity condition is that the rate of change of density within an infinitesimal volume must be balanced by the net incoming mass flow, and this condition is expressed as

$$\frac{\partial \rho}{\partial t} = -\nabla \cdot (\rho \underline{v}_T)$$

which can be rewritten as

$$\frac{d\rho}{dt} + \nabla \cdot \underline{v}_T = 0$$

where $d\rho/dt$ is the rate of change of density of a fluid element moving with the water particles. Because the fluid is essentially incompressible under motions induced by gravity waves of decameter wavelength, this rate of change is zero which results in the incompressibility condition,

$$\nabla \cdot \underline{v}_T = \nabla \cdot \tilde{v} = 0$$

The second part of this equation is a result of the assumption that the current \underline{U} is horizontal and varies with depth only. For each plane-wave

component with wave number $\underline{k} = (k_x, k_y)$, the above incompressibility condition can be expressed as

$$-ik_x u = ik_y v + w' \quad (2.8)$$

Note that this is the continuity equation for incompressible fluid, used here to eliminate U and U' from Eqs. (2.7). After straightforward manipulations,

$$ik_y w - v' + \frac{k_x U' v}{\Delta} = 0 \quad (2.9a)$$

$$ik_y v' + w'' - k_x^2 w - \frac{ik_y (k_x U' v)}{\Delta} + \frac{k_x \dot{U}'' w}{\Delta} = 0 \quad (2.9b)$$

where $\Delta = \omega - k_x U$.

Equation (2.9a) is now multiplied by ik_y and the result is added to Eq. (2.9b). The resulting second-order differential equation for the vertical component of the wave-induced velocity perturbation is

$$w'' + \left(\frac{k_x U''}{\omega - k_x U} - k^2 \right) w = 0 \quad (2.10)$$

Because \underline{U} and the \hat{x} axis are parallel,

$$k_x U = \underline{k} \cdot \underline{U}$$

and Eq. (2.10) can be rewritten as

$$w'' + \left[\frac{(\underline{k} \cdot \underline{U})''}{(\omega - \underline{k} \cdot \underline{U})} - k^2 \right] w = 0 \quad (2.11)$$

which is a form of the Orr-Sommerfeld equation for inviscid fluid. Because the scalar product is invariant under coordinate rotation, it can be concluded that, for an arbitrary ocean-current direction in the horizontal plane, this equation is still valid. It should be noted that only

the component of the mean horizontal drift in the direction of wave propagation affects the coefficients of Eq. (2.11), which implies that the ocean-wave dispersion relation $\omega = \omega(k)$ is independent of currents orthogonal to the propagation direction. It is thus possible to align the wave-number vector \underline{k} with one of the horizontal axes and reduce the wave-propagation problem to two dimensions; such a reduction is attributed to Squires [1933].

B. Boundary Conditions at the Free Surface

The dynamic boundary at the ocean surface can be determined by examining the vertical component of Eq. (2.1). Based on the assumption of purely horizontal mean drift with only a vertical gradient, this component simplifies to

$$-i(\omega - \underline{k} \cdot \underline{U}) w = -\frac{1}{\rho} \frac{\partial P_T}{\partial z} - g \quad (2.12)$$

for each plane wave.

The pressure P_T can be separated into two components,

$$P_T = P_0 + P_1$$

where P_0 is the hydrostatic pressure in the absence of waves, and P_1 is the dynamic pressure induced by surface waves. The zeroth-order component of Eq. (2.12), therefore, is

$$P_0(z) = P_a - \rho g z$$

where z is measured from the mean sea surface (positive upward), and P_a is the atmospheric pressure considered here as an ambient condition because no attempt is made to analyze the generation of waves by wind turbulence.

The first-order component can be obtained by multiplying each side of Eq. (2.12) by η which is the surface height above the mean level $z = 0$ (see Fig. 2.2) and dropping terms nonlinear in the wave-perturbed quantities. The result is

$$P_1 \Big|_{z=0} = \rho g \eta \quad (2.13)$$

which is the dynamic condition at the free surface $z = \eta$, where η is assumed to be small enough for the vertical pressure gradient to be approximated linearly as

$$\frac{\partial P_1}{\partial z} \approx \frac{P_1 \Big|_{z=\eta} - P_1 \Big|_{z=0}}{\eta} = \frac{-P_1 \Big|_{z=0}}{\eta}$$

Pressure is continuous at the interface $z = \eta$. Because no wind/sea interaction is assumed, there is no first-order pressure at the surface.

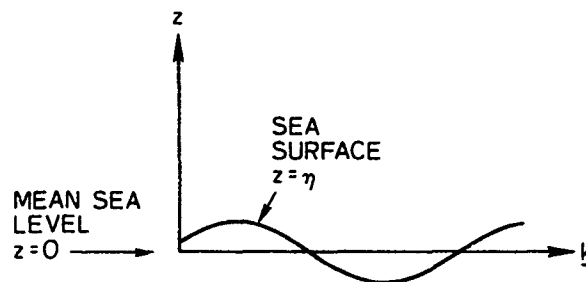


Fig. 2.2. SEA SURFACE IN THE PLANE OF WAVE PROPAGATION.

The second condition at the air/sea interface is the restriction of an unbroken surface. If z describes the vertical coordinate of a water particle, this condition can be stated [see Lamb, 1932] as

$$\left[\frac{d}{dt} (z - \eta) \right]_{z=\eta} = 0$$

Now, dz/dt is the vertical particle velocity w . This condition indicates that the vertical velocity of any particle at the surface equals the vertical velocity of the surface seen by the same particle,

$$w \Big|_{z=0} = -i[\omega - \underline{k} \cdot \underline{U}(0)] \eta \quad (2.14)$$

This is called the kinematic boundary condition wherein the terms nonlinear in the wave-perturbed quantities have been dropped. Combining the dynamic and kinematic conditions to eliminate the surface-height variable η results in

$$-i[\omega - \underline{k} \cdot \underline{U}(0)] P_1 \Big|_{z=0} = \rho g w \Big|_{z=0}$$

The x component in Eq. (2.1) is now used to eliminate the dynamic pressure P_1 . After some straightforward algebra,

$$-i[\omega - \underline{k} \cdot \underline{U}(0)]^2 u \Big|_{z=0} + w \Big|_{z=0} U'_x(0) [\omega - \underline{k} \cdot \underline{U}(0)] = g k_x w \Big|_{z=0} \quad (2.15)$$

For simplicity, the x axis is now chosen to lie parallel to the wave-number vector \underline{k} . The component of ocean current in the x direction is denoted by U_x .

The continuity equation for incompressible fluid [Eq. (2.8)] requires that

$$iku = -w'$$

which, when substituted into (2.15), obtains the linearized boundary condition at the free surface,

$$\left[\omega - k U_x(0) \right]^2 w' \Big|_{z=0} + k U'_x(0) \left[\omega - k U_x(0) \right] w \Big|_{z=0} = g k^2 w \Big|_{z=0} \quad (2.16)$$

C. Wave Phase Velocity Determined from Solutions of the Orr-Sommerfeld Equation

The phase velocity c of the ocean surface wave with wave number k and radian frequency ω is

$$c = \frac{\omega}{k}$$

As in Section B, \underline{k} is in the positive x direction and U_x is the x component of the total current vector. The Orr-Sommerfeld equation [Eq. (2.11)] for the vertical component w of the wave-induced particle motion can now be written as

$$w'' + \left(\frac{U''}{c - U_x} - k^2 \right) w = 0 \quad (2.17)$$

where the double primes indicate differentiation with respect to the distance z above the mean sea level. The linearized boundary condition as defined in Eq. (2.16) is now

$$(c - U_{x0})^2 w'_0 + U'_{x0} (c - U_{x0}) w_0 = g w_0 \quad (2.18)$$

where 0 denotes evaluation at the mean sea level $z = 0$.

Equations (2.17) and (2.18) are solved below for the following cases. It should be noted that, in cases 1 and 2, $U''_x = 0$ so that the solution to the Orr-Sommerfeld equation [(2.17)] is

$$w = a \exp(kz) \quad (2.19)$$

because $w = 0$ at the rigid ocean bottom $z = -\infty$.

Case 1: A Constant Current Profile $U_x(z) = U_0$.

In this case, an expression is obtained for wave phase velocity c_0 in the absence of current, and the intuitively obvious Doppler shift in the phase velocity in the presence of a uniform current is introduced.

Based on the solution in Eq. (2.19), the linearized boundary condition becomes

$$(c - U_0)^2 = \frac{g}{k} \quad (2.20)$$

If there is no mean drift, the gravity wave with wave number k has a phase velocity of

$$c = \pm c_0 \triangleq \pm \left(\frac{g}{k} \right)^{1/2} \quad (2.21a)$$

where + and - indicate waves propagating in the positive and negative x directions, respectively.

In the presence of a uniform horizontal drift U_0 , the wave radian frequency is Doppler shifted by an amount equal to kU_0 --a result obtainable from (2.20),

$$c = \pm c_0 + U_0 \quad (2.21b)$$

When waves move with the ocean current, the sum of c_0 and U_0 is observed and, when they move opposite to the ocean current, the difference of c_0 and U_0 is observed.

Case 2: A Linear Current Profile $U_x(z) = U_0 + (U_1/\ell) z$.

This is the only profile that yields an exact expression for the wave velocity c .

Again, Eq. (2.19) is the general solution to the Orr-Sommerfeld equation. The boundary condition [(2.18)] reduces to the quadratic equation,

$$(c - U_0)^2 + \frac{U_1}{k\ell} (c - U_0) - (c_0)^2 = 0$$

whose solution is

$$c = U_0 - \frac{U_1}{2k\ell} \pm c_0 (1 + s^2)^{1/2} \quad (2.22)$$

where $s = [1/(2k\ell)] \cdot U_1/c_0 = [U_1/(2kc_0)]$.

If the term quadratic in U_1/c_0 is neglected, the result is identical to that obtained by Stewart and Joy [1974] who observed that the difference between c and the still-water phase velocity c_0 is the value of the current at depth $1/2k$ below the mean sea level. If the quadratic term is dropped, the magnitude of this difference is the same for waves propagating upstream and downstream relative to the current. Equation (2.22) indicates that, for waves propagating downstream, this difference is

$$\delta_+ = U_x \Big|_{z=-1/(2k)} + c_0 (1 + s^2)^{1/2} - c_0$$

and, for waves propagating upstream, it is

$$\delta_- = U_x \Big|_{-1/(2k)} - c_0 (1 + s^2)^{1/2} - (-c_0)$$

Waves propagating downstream, therefore, are Doppler shifted more than those propagating upstream by an amount Δ (rad/sec),

$$\Delta = k(\delta_+ - \delta_-) = 2kc_0 \left[(1 + s^2)^{1/2} - 1 \right] \quad (2.23)$$

Because the quadratic term in Eq. (2.22) always adds to c_0 , the waves are speeded up by that term.

Case 3: General Current Profile in the Weak-Interaction Regime.

In this case, the maximum magnitudes of U_x/c_0 , U'_x/kc_0 , and U''_x/k^2c_0 are all on the order of ϵ where $0 \leq \epsilon \ll 1$. Following Stewart and Joy [1974], the perturbation approach is adopted. Their first-order result will be confirmed by the following independent derivations, and a second-order result will be obtained for an exponential profile.

Equation (2.17) will now be solved by perturbation expansion. Only cases are considered where the maximum magnitudes of U_x , U'_x/k , and U''_x/k^2 are small compared to the wave phase velocity c_0 in the absence of current. The perturbation expansions for the phase velocity c and for the vertical component w of the wave-induced particle velocity are

$$c = c^{(0)} + c^{(1)} + c^{(2)} + \dots$$

$$w = w^{(0)} + w^{(1)} + w^{(2)} + \dots$$

and the perturbation parameter is

$$\epsilon = \max |r| \quad 0 \leq \epsilon < 1$$

where $r = U_x/c_0$.

The n^{th} derivative of U_x is assumed to have a magnitude of order $k^n \epsilon c_0$. Writing $p_i = c^{(i)}/c_0$, with $p_0 = 1$, Eqs. (2.17) and (2.18) can be expressed as

$$w'' - k^2 w = -r'' \left[1 - (p_1 - r) + \dots \right] w \quad (2.24a)$$

with the condition that

$$\left[1 + (p_1 - r) + p_2 + \dots \right]^2 w' + r' \left[1 + (p_1 - r) \right] w = kw \quad (2.24b)$$

at $z = 0$.

To first order in ϵ , Eqs. (2.24) simplify to

$$w^{(1)''} - k^2 w^{(1)} = -r'' a \exp(kz) \quad (2.25a)$$

with the condition that

$$p_1 = \frac{-\left[w^{(1)'} - k w^{(1)} + (r' - 2kr) a \right]}{2ka} \quad (2.25b)$$

at $z = 0$. The second-order terms can be similarly extracted:

$$w^{(2)''} - k^2 w^{(2)} = r'' \left[(p_1 - r) a \exp(kz) - w^{(1)} \right] \quad (2.26a)$$

with the condition at $z = 0$ that

$$p_2 = \frac{-\left[w^{(2)'} - k w^{(2)} + 2(p_1 - r) w^{(1)'} + r' w^{(1)} + ka(p_1 - r)^2 + ar'(p_1 - r) \right]}{2ka} \quad (2.26b)$$

First-Order Solutions

The general solution to Eq. (2.25a) is the sum of the complementary solution $d \exp(kz)$ and the particular solution $w_p^{(1)}(z)$, where d is

an arbitrary constant. The solution proportional to $\exp(-kz)$ is rejected because it diverges at $z = -\infty$. The particular solution can be written as

$$w_p^{(1)} = -b(z) a \exp(-kz) \quad (2.27)$$

This is substituted into Eq. (2.25a) to arrive at the following differential equation for $b(z)$:

$$b'' - 2kb' - r'' \exp(2kz) = 0$$

whose solution

$$b' = r' \exp(2kz)$$

can be obtained by inspection.

The first-order solution to the Orr-Sommerfeld equation is

$$w^{(1)} = d \exp(kz) - a \exp(-kz) \int_{-\infty}^z \frac{U'_x(z)}{c_0} \exp(2kz) dz$$

The first term will not affect the first-order phase velocity c . Direct substitution of the above expression for $w^{(1)}$ into the boundary condition in Eq. (2.25a) yields

$$c^{(1)} = U_{x0} - \int_{-\infty}^0 \frac{U'_x(z)}{c_0} \exp(2kz) dz$$

Alternately, after integration by parts,

$$c^{(1)} = 2k \int_{-\infty}^0 U_x(z) \exp(2kz) dz \quad (2.28)$$

which is the same result obtained by Stewart and Joy [1974] except that their final result has misplaced parentheses and their U is the normalized current r .

It can be concluded that the current-induced Doppler velocity is the ocean-current component U_x averaged over depth with $\exp(2kz)$ as the

weighting function. The integral in Eq. (2.28) can also be interpreted as a Laplace transform evaluated on the real axis. These observations will be used to extract ocean-current and current-shear information from HF backscatter data.

Second-Order Solutions

Because the general solution to Eq. (2.25b) is complicated and difficult, only a special case is presented to illustrate the method and provide an interesting result.

A current profile

$$U_x(z) = U_0 \exp(mz)$$

decaying with depth and with a scale length of m^{-1} is assumed. After much algebra,

$$c = c_0 + \frac{2kU_0}{2k+m} + \frac{c_0}{2} s^2 \frac{k}{m+k} \quad (2.29)$$

where $s = (U_0/c_0) \cdot m/(2k+m)$, which is valid for waves propagating in the direction of U_0 (downstream). For waves propagating upstream, c_0 is replaced by $-c_0$, and the phase velocity of these waves is

$$c_{\text{upstream}} = -c_0 + \frac{2kU_0}{2k+m} - \frac{c_0}{2} s^2 \frac{k}{m+k}$$

To verify this result, consider the case where the magnitude of m is much smaller than k ; in other words, the current profile varies slowly (on the order of one wavelength) on the spatial scale. This profile and the phase velocity can then be approximated by a Taylor series expansion, thus yielding

$$c = U|_{z=-1/(2k)} \pm c_0 \left(1 + \frac{1}{2} s^2\right) \quad (2.30)$$

where $s = U'|_{z=0}/(2kc_0)$.

For a linear current profile, Eq. (2.22) is an exact expression for phase velocity c . If the square-root term is expanded, the result will agree with Eq. (2.30) to order s^2 .

D. Summary

Still-water phase velocity of ocean surface waves of decameter wavelength has been shown to be

$$c_0 = \pm \sqrt{\frac{g}{k}} \quad (2.31)$$

where g is gravitational acceleration and k is the wave number. The + and - indicate propagation along the positive and negative x axes, respectively (the x axis is aligned with the wave-number vector \underline{k}).

In the presence of a uniform horizontal current whose component in the direction of the x axis is U_0 , the waves are Doppler shifted so that the phase velocity becomes

$$c = \pm c_0 + U_0$$

When ocean current \underline{U} varies linearly with depth, c becomes

$$c = U_x \Big|_{z=-1/(2k)} \pm c_0 (1 + s^2)^{1/2}$$

where $s = U'_x / (2kc_0)$. Here, U_x denotes the current component in the x direction and U'_x is its derivative with depth. The signs are associated with the propagation direction with respect to the x axis.

Comparison of the second-order solution [Eq. (2.30)] to the above exact expression for c (for linear \underline{U}) suggests a scale length ℓ^* where

$$\ell^* = \min \left| \frac{4\pi c_0}{U'_x} \right| \quad (2.32)$$

for checking the validity of the perturbation approach. Here, \min indicates the minimum over an effective depth on the order of L . To first order in ℓ^*/L ,

$$c = \pm c_0 + 2k \int_{-\infty}^0 U_x(z) \exp(2kz) dz \quad (2.33)$$

which, from the definition of c , can be expressed in terms of the temporal frequency of oscillation $f = \omega/(2\pi)$. As a result,

$$f = \pm f_B + \left[\frac{k}{2\pi} \right] 2k \int_{-\infty}^0 U_x(z) \exp(2kz) dz \quad (2.34)$$

where

$$f_B = \frac{kc_0}{2\pi} = \frac{(gk)^{1/2}}{2\pi}$$

is the frequency of oscillation of the ocean surface wave in the absence of current.

Roughly speaking, the effective Doppler shift is caused by current in the uppermost ocean layer having a thickness on the order of one wavelength, which is evident in the exponential weighting factor $\exp(2kz)$. The requirements of incompressibility and continuity demand a divergence-free wave-induced velocity field for the fluid. Because this velocity field has a horizontal scale of variation equal to the wavelength L , its vertical scale of variation must also be equal to L . This being true, it is influenced by the ocean current within a depth on the order of one wavelength.

The ocean-current magnitudes encountered in this investigation are, at most, approximately 40 cm/sec, and still-water wave phase velocity is at least 280 m/sec. This implies that the effective scale length defined in Eq. (2.31) is much larger than the vertical scale of variation of $U(z)$. As a result, the effects to second order in l^*/L can be ignored in most cases.

Chapter III

STATISTICAL DESCRIPTION OF OCEAN WAVES

The purpose of this chapter is threefold: first, to discuss the statistical nature of the ocean waves and the associated statistical estimation problem, second, to introduce the concept of directional spectra and, third, to compare their various definitions. The first two are of direct relevance to this work; the third, however, requires clarification and should be useful as a reference for radio oceanographers.

The highly irregular nature of the ocean surface makes detailed measurements difficult to obtain. The standard approach is to model the irregular temporal and spatial variations of any relevant quantity pertaining to surface motion as realizations of an ergodic random process. The ensemble average of a function of this quantity can be asymptotically approached by averaging the function over an increasing number of time and space samples.

The quantity of special interest is the long-crested wave component $A(\underline{k}, \omega)$ of ocean-surface motion selected by the Bragg-scattering mechanism. If η is the elevation of the surface above the mean sea level $z = 0$, then

$$A(\underline{k}, \omega) = \left(\frac{1}{2\pi}\right)^3 \iiint_{-\infty}^{\infty} d\underline{r} dt \eta(\underline{r}, t) \exp[i(\underline{k} \cdot \underline{r} - \omega t)] \quad (3.1)$$

where

\underline{k} = wave-number vector

ω = wave radian frequency

\underline{r} = horizontal spatial vector defining the spatial location of any surface element

t = time

This is a divergent integral, and the problem can be resolved by using the Dirac delta function. Note that, in practice, $A(\underline{k}, \omega)$ is a quantity that cannot be determined exactly because measurements of η for

all temporal and spatial points are not available; at best, only a close estimate of $A(\underline{k}, \omega)$ can be obtained.

Section A reviews the problems of spectral estimation and the relationship between ensemble and actual averaging. The Wiener-Khinchin theorem is derived in Section B, and various power spectra used by oceanographers and radio oceanographers are compared.

A. Practical Spectral Estimation

According to Eq. (3.1), it is not possible to measure $A(\underline{k}, \omega)$. This long-crested wave component can be estimated, however, by observing the surface elevation η over finite time duration T and finite spatial extent L .

Without neglecting any salient characteristics of the problem, this discussion is limited to a time series $s(t)$ whose finite-time transform at time τ and frequency f is

$$\hat{S}(f, \tau) = \frac{1}{2\pi} \int_{-T/2}^{T/2} s(t + \tau) w(t) \exp(-i2\pi ft) dt \quad (3.2)$$

where $w(t)$ is a window function that can be chosen to best fit this finite-time transform to the theoretical transform

$$S(f) = \frac{1}{2\pi} \int_{-\infty}^{\infty} s(t) \exp(-i2\pi ft) dt \quad (3.3)$$

Harris [1978] has reviewed the many choices of $w(t)$. In the discussion here, a rectangular window has been selected with width T , height unity, and centered at $t = 0$, and Eq. (3.2) reduces to

$$\hat{S}(f, \tau) = \frac{1}{2\pi} \int_{-T/2}^{T/2} s(t + \tau) \exp(-i2\pi ft) dt \quad (3.4)$$

Because the phase of the signal $s(t)$ is not known a priori, the above Fourier-transform kernel does not adjust itself as different segments of the signal are examined. There are the following two major differences between the theoretical transform (3.3) and its estimate (3.4).

- The rectangular time window leads to a transform that is the convolution of the theoretical transform and $\sin(\pi fT)/fT$ whose first zeros are separated by $2/T$.
- The estimate can be time-dependent.

To obtain average values of any function $F(\hat{S})$ of the estimate \hat{S} , \hat{S} and F are computed for various values of τ ($\tau = nT_a$, $n = 0, 1, \dots, N-1$), and the average is then taken. A function of \hat{S} most commonly used is its squared magnitude (power spectrum) and, to simplify the following derivations, the function F is assumed to be \hat{S} itself. Writing the average value as $\bar{S}(f)$,

$$\bar{S}(f) = \frac{1}{N} \sum_{n=0}^{N-1} \frac{1}{2\pi} \int_{-T/2}^{T/2} s(t + nT_a) \exp(-i2\pi ft) dt \quad (3.5)$$

Bringing the summation sign through the integral, it is apparent that averaging over S is equivalent to averaging over the time signal $s(t + nT_a)$,

$$\bar{S}(f) = \frac{1}{2\pi} \int_{-T/2}^{T/2} \bar{s}(t) \exp(-i2\pi ft) dt \quad (3.6)$$

where

$$\bar{s}(t) = \frac{1}{N} \sum_{n=0}^{N-1} s(t + nT_a)$$

It can be shown that the averaging process is equivalent to passing $s(t)$ through a filter with a transfer function $H(f)$ such that

$$|H(f)|^2 = \frac{1}{N^2} \frac{\sin^2(\pi fNT_a)}{\sin^2(\pi fT_a)}$$

and this filter function is illustrated in Fig. 3.1. If the average sampling time T_a is small so that the sampling rate is higher than twice the bandwidth of the signal, this discrete averaging process is equivalent to passing the signal through a lowpass filter of width $1/NT_a$.

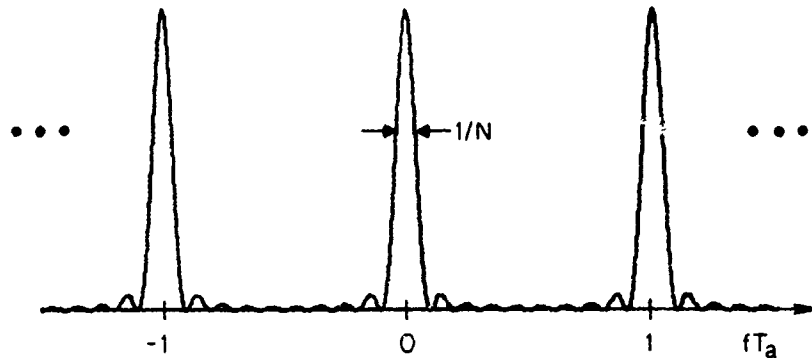


Fig. 3.1. MAGNITUDE SQUARED OF FILTER FUNCTION VS
NORMALIZED FREQUENCY fT_a .

Statistically, the average over discrete samples is a maximum-likelihood estimator of the ensemble mean if these samples are obtained from a population with a gaussian distribution. If N is large enough for the confidence level to exceed the requirements, this estimator is considered the ensemble mean and is denoted by angular brackets $\langle \rangle$. Applying this operator to Eq. (3.4),

$$\langle \hat{S}(f, \tau) \rangle = \frac{1}{2\pi} \int_{-T/2}^{T/2} \langle s(t + \tau) \rangle \exp(-i2\pi ft) dt \quad (3.7)$$

because $s(t)$ is the random process. Note the similarity between the time-average operator (denoted by the overbar) in Eq. (3.6) and the ensemble-average operator in Eq. (3.7). Both operate solely on the random process $s(t)$.

The above discussions have considered the problem of estimating the ensemble mean in practice. In the following analysis, the statistical approach is adopted for convenience.

B. Relationships among Various Power Spectra Used by Radio Oceanographers

In this section, the Wiener-Khinchin theorem is derived in a heuristic manner, based on the following assumptions.

- The random process $\eta(\underline{r}, t)$ has an ensemble mean h that is time-independent and spatially uniform. For convenience, the coordinate system is adjusted so that this mean value is zero.
- The autocovariance function defined by

$$C_g(\underline{r}_1, t_1; \underline{r}_2, t_2) = \left\langle \left[\eta(\underline{r}_1, t_1) - h \right] \left[\eta(\underline{r}_2, t_2) - h \right] \right\rangle$$

$$= \left\langle \eta(\underline{r}_1, t_1) \eta(\underline{r}_2, t_2) \right\rangle$$

is invariant under time and space translation; that is,

$$C_g(\underline{r}_1, t_1; \underline{r}_2, t_2) = C(\underline{r}_1 - \underline{r}_2, t_1 - t_2)$$

These assumptions in the time (space) domain restrict the following considerations to processes that are stationary (homogeneous) at least to second order, and a power spectrum proportional to the mean-squared spectral amplitude will be related to the autocovariance function of this process.

Note that the first assumption implies that the spectral amplitude defined by $A(\underline{k}, \omega)$ is also zero mean,

$$\langle A(\underline{k}, \omega) \rangle = 0$$

The covariance of spectral amplitudes at points (\underline{k}, ω) and $(\underline{k}', \omega')$ is thus

$$\langle A(\underline{k}, \omega) A^*(\underline{k}', \omega') \rangle$$

$$= \left(\frac{1}{2\pi} \right)^6 \int_{-\infty}^{\infty} d\underline{r} dt d\underline{r}' dt' C(\underline{r} - \underline{r}', t - t') \exp[i(\underline{k} \cdot \underline{r} - \underline{k}' \cdot \underline{r}') - i(\omega t - \omega' t')]$$

where the single integral represents the sixfold integral and the * indicates a complex conjugate. The variable set $(\underline{r}, \underline{r}', t, t')$ is now transformed to $(\underline{r}, \underline{\rho}, t, \tau)$ where $\underline{\rho} = \underline{r} - \underline{r}'$ and $\tau = t - t'$. Recall that

$$\int_{-\infty}^{\infty} dt \exp(\pm i\omega t) = 2\pi\delta(\omega)$$

where $\delta(\omega)$ is the Dirac delta function. This integral is only convergent in the sense of a Cesaro limit, and the delta function has a symbolic meaning, as discussed by Born and Wolf [1975]. Based on this relationship, the covariance function above reduces to

$$\begin{aligned} & \langle A(\underline{k}, \omega) A^*(\underline{k}', \omega') \rangle \\ &= \left(\frac{1}{2\pi}\right)^3 \int_{-\infty}^{\infty} d\underline{\rho} d\tau C(\underline{\rho}, \tau) \exp[i(\underline{k} \cdot \underline{\rho} - \omega\tau)] \delta(\underline{k} - \underline{k}') \delta(\omega - \omega') \end{aligned}$$

It has been demonstrated, therefore, that spectral amplitudes at different wave numbers or frequencies are uncorrelated. This result as applied to a wide-sense stationary time series has been discussed in detail by Helstrom [1960]. A power spectrum $P(\underline{k}, \omega)$ is now defined by

$$P(\underline{k}, \omega) \delta(\underline{k} - \underline{k}') \delta(\omega - \omega') = \langle A(\underline{k}, \omega) A^*(\underline{k}', \omega') \rangle \quad (3.8)$$

from which

$$P(\underline{k}, \omega) = \left(\frac{1}{2\pi}\right)^3 \int_{-\infty}^{\infty} d\underline{\rho} d\tau C(\underline{\rho}, \tau) \exp[i(\underline{k} \cdot \underline{\rho} - \omega\tau)] \quad (3.9)$$

is obtained. This is the Wiener-Khinchin theorem wherein the power spectrum defined by Eq. (3.8) is the Fourier transform of the autocovariance function of the homogeneous and stationary process. From the inverse relation, the mean-squared height H^2 of the ocean surface is determined to be

$$H^2 = \int_{-\infty}^{\infty} d\underline{k} d\omega P(\underline{k}, \omega) \quad (3.10)$$

From the definition in Eq. (3.8), the power spectrum is positive real. In addition, because the autocovariance function is real, it follows that

$$P(\underline{k}, \omega) = P(-\underline{k}, -\omega) \quad (3.11)$$

For first-order gravity waves in deep still water, the dispersion relation has only two roots [Eq. (2.21a)],

$$\omega = \pm \omega_{BO} = \pm \sqrt{gk}$$

so that the frequency dependence in the power spectrum P can be removed, and a wave-height directional spectrum $S(\underline{k})$ can be generated. Because there is no unique definition of $S(\underline{k})$, however, various definitions found in the literature are presented in sufficient detail for direct comparisons.

As a result of the pioneering work of Rice [1951] on scattering from random surfaces, a direct extension of his original wave-number spectrum $W(\underline{k})$ to include an added time dimension is frequently encountered. Because his spectrum is a Fourier analysis in space only, the complex-conjugate relation (3.11) reduces to

$$W(\underline{k}) = W(-\underline{k}) \quad (3.12)$$

Generally, $P(\underline{k}, \omega)$ is not symmetric about either of the two wave-number axes \hat{k}_x and \hat{k}_y . To generate a directional spectrum that obeys Eq. (3.12), it is necessary to add P to its mirror image about the origin of the wave-number axes. The new directional spectrum $S_{r1}(\underline{k})$, therefore, is

$$P(-\underline{k}, \omega) + P(\underline{k}, \omega) = \frac{1}{4} S_{r1}(\underline{k}) \left[\delta(\omega - \omega_{BO}) + \delta(\omega + \omega_{BO}) \right] \quad (3.13)$$

The factor preceding $S_{r1}(\underline{k})$ is required so as to conform with the normalization relation that Rice adopted,

$$H^2 = \frac{1}{4} \int_{-\infty}^{\infty} d\underline{k} S_{r1}(\underline{k}) \quad (3.14)$$

which can be verified by substituting Eq. (3.13) into (3.10).

To depict the various directional spectra simply, the following ideal sea conditions are assumed. A group of wave trains with a narrow spread in wavelength is propagating in the $+x$ direction while another group with a lower energy density and a smaller spread in wavelength is propagating

in the $-x$ direction. The exact dependence on wave number k is assumed to be triangular--an abrupt cutoff at the lower wave-number limit and a linear rolloff from there to the higher wave-number limit. The directional spectrum $S_{r1}(\underline{k})$ along the k_x axis, illustrated in Fig. 3.2, describes the ideal sea.

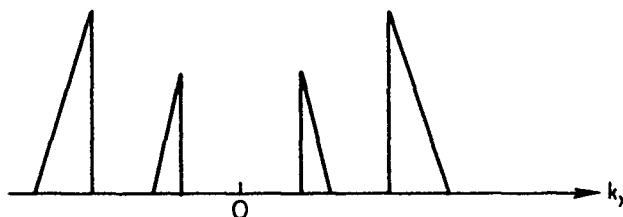


Fig. 3.2. DIRECTIONAL WAVE-HEIGHT SPECTRUM $S_{r1}(\underline{k})$ FOR IDEAL SEA CONDITIONS. The directional spectrum $S_{r1}(\underline{k})$ is shown only in the $(k_x, 0)$ plane.

The inverse relation can be obtained from Eq. (3.13) as

$$P(\underline{k}, \omega_{BO}) \Delta\omega + P(\underline{k}, -\omega_{BO}) \Delta\omega = \frac{1}{4} S_{r1}(\underline{k}) \quad (3.15)$$

by integrating over a narrow region in the frequency domain centered at $\omega = \omega_{BO}$. The choice of $\Delta\omega$ (the infinitesimal frequency interval over which P is constant) is determined by the limiting function from which the delta function is derived. In comparison to a Fourier series in the limit of infinite period T , $\Delta\omega$ should be $2\pi/T$. From Eqs. (3.11) and (3.15),

$$S_{r1}(\underline{k}) = S_{r1}(-\underline{k}) \quad (3.16)$$

which is in accordance with Rice's constraint [Eq. (3.12)].

Because there is an awkward factor of 4 in the normalizing relation in Eq. (3.14), attempts have been made to eliminate it by introducing a modified spectrum $S_{r2}(\underline{k})$ as

$$S_{r2}(\underline{k}) = \frac{1}{4} S_{r1}(\underline{k}) \quad (3.17)$$

From this definition, the volume under the $S_{r2}(\underline{k})$ surface is exactly equal to the ocean mean-squared height.

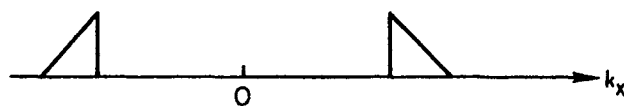
The drawback of the above two definitions [Eqs. (3.15) and (3.17)] is that the energy in the waves propagating in the $+\underline{k}$ direction is combined with the energy in the waves propagating in the $-\underline{k}$ direction to determine the height of $S(\underline{k})$. As a result, $S(\underline{k})$ cannot be interpreted as energy associated exclusively with waves moving in the $+\underline{k}$ or $-\underline{k}$ direction. To eliminate this plus-minus ambiguity, Barrick [1970] introduced the spectra $S_+(\underline{k})$ and $S_-(\underline{k})$ and defined the x axis as the direction of propagation of the radio wave incident on the ocean surface; therefore,

$$S_{\pm}(\underline{k}) = P(\underline{k}, \pm\omega_s) \Delta\omega \quad (3.18)$$

where

$$\omega_s = \begin{cases} +\omega_{BO} & \underline{k} \text{ in the plus-}x \text{ half-plane} \\ -\omega_{BO} & \underline{k} \text{ in the minus-}x \text{ half-plane} \end{cases}$$

These spectra are illustrated in Fig. 3.3 for the same ideal sea conditions described for Fig. 3.2. This is an extremely awkward definition because the energy associated with waves propagating in the positive k_x half-plane is contained in $S_+(\underline{k})$ and the energy for negative k_x is



a. $S_+(\underline{k})$ in the $(k_x, 0)$ plane



b. $S_-(\underline{k})$ in the $(k_x, 0)$ plane

Fig. 3.3. DIRECTIONAL WAVE-HEIGHT SPECTRA FOR IDEAL SEA CONDITIONS.

contained in $S_{-}(\underline{k})$. It is not clear if a long-crested wave in the $\pm y$ direction (for which $k_x = 0$) should be included in S_{+} or S_{-} .

A simple modification of Eq. (3.17) produces a directional spectrum S_o free of the above ambiguities,

$$P(\underline{k}, \omega) = \frac{1}{2} S_o(\underline{k}) \delta(\omega - \omega_{BO}) + \frac{1}{2} S_o(-\underline{k}) \delta(\omega + \omega_{BO}) \quad (3.19a)$$

or, equivalently,

$$P(\underline{k}, \omega_{BO}) \Delta\omega = \frac{1}{2} S_o(\underline{k}) \quad (3.19b)$$

Again for the same ideal sea conditions described for Fig. 3.2, this definition of the directional spectrum is illustrated in Fig. 3.4. It can

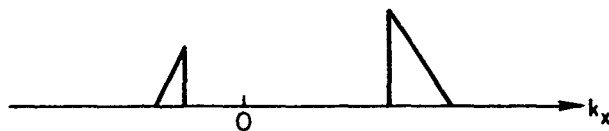


Fig. 3.4. DIRECTIONAL WAVE-HEIGHT SPECTRUM $S_o(\underline{k})$ FOR IDEAL SEA CONDITIONS. $S_o(\underline{k})$ is shown only in the $(k_x, 0)$ plane.

be verified that the complex-conjugate relation [Eq. (3.11)] is not violated; it also follows that the mean-squared height is

$$H^2 = \int_{-\infty}^{\infty} d\underline{k} S_o(\underline{k}) \quad (3.20)$$

Recalling that the Fourier-transform exponent is $i(\underline{k} \cdot \underline{r} \cdot \omega t)$, Eq. (3.19b) implies that $S_o(\underline{k})$ is the energy density associated with waves propagating in the \underline{k} direction and that $S_o(-\underline{k})$ is associated with the $-\underline{k}$ direction. The definition in Eq. (3.19a) is the corrected version of that obtained by Phillips [1966,1978], and it is identical to that of Longuet-Higgins et al [1961] except that the inverse of their power spectrum is the complex autocovariance function of a process that is the analytic-signal representation of the surface-height process η .

Figure 3.5 compares various directional spectra in the $k_x - k_y$ plane. Referring to Fig. 3.2, these spectra may represent swells propagating in opposite directions and with different mean wave numbers; however, these simplistic models serve as a basis for straightforward comparisons.

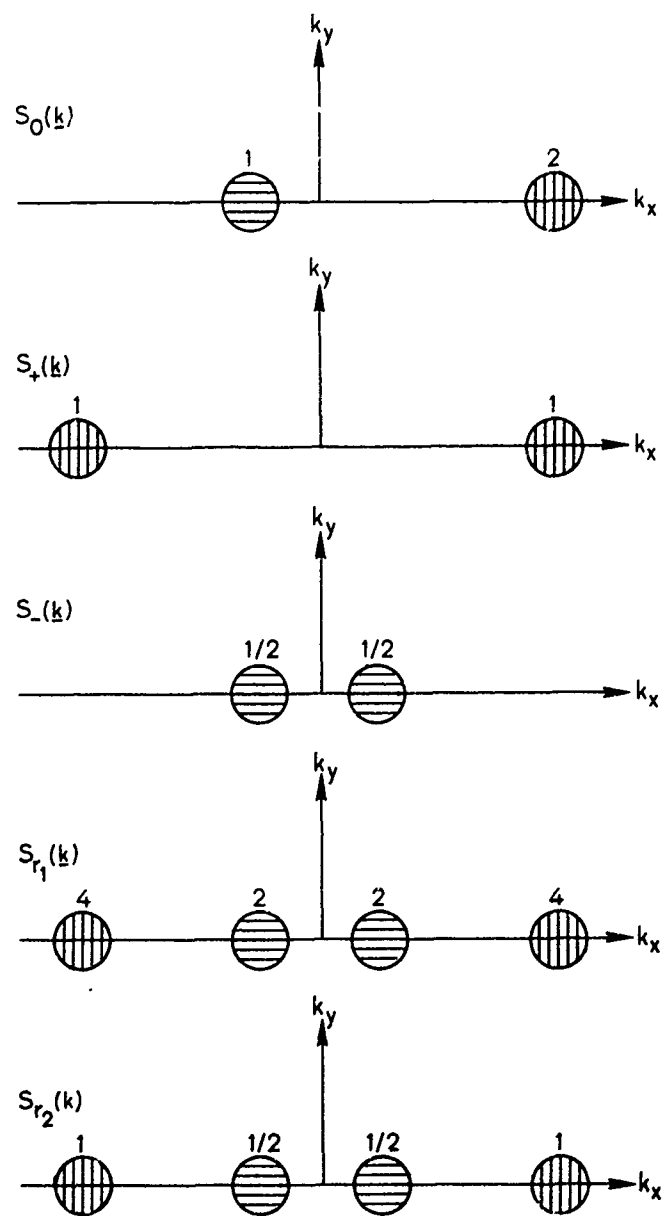


Fig. 3.5. COMPARISONS OF VARIOUS WAVE-HEIGHT DIRECTIONAL SPECTRA. Numbers beside the shaded area indicate heights of pedestal above the $k_x - k_y$ plane.

Chapter IV

THEORETICAL STUDIES OF FIRST-ORDER BACKSCATTER FROM OCEAN SURFACE WAVES OF DECAMETER WAVELENGTH

The physical processes occurring in the ocean as influenced by the presence of current and the statistical nature of the ocean surface waves have been analyzed in Chapters II and III. In this chapter, the problem of remotely sensing these ocean waves by means of an HF pulsed radar is discussed. This radar system consists of a transmitter and a receiver located in proximity to one another so that they are colocated for the theoretical considerations to be presented here.

As shown in Fig. 4.1, the radar system is situated on the coast at an elevation h much smaller than the distance r_0 from the ocean patch it is designed to probe. (In the experiments, h is approximately 40 m and r_0 is roughly 10 to 40 km.) To a good approximation, the radio wave transmitted by the radar propagates at a zero elevation angle with respect to the sea surface. The azimuthal extent L_y of the ocean patch is established by the beamwidth of the radar system in the horizontal plane; this beamwidth, in turn, is defined by the combined beam formed by the

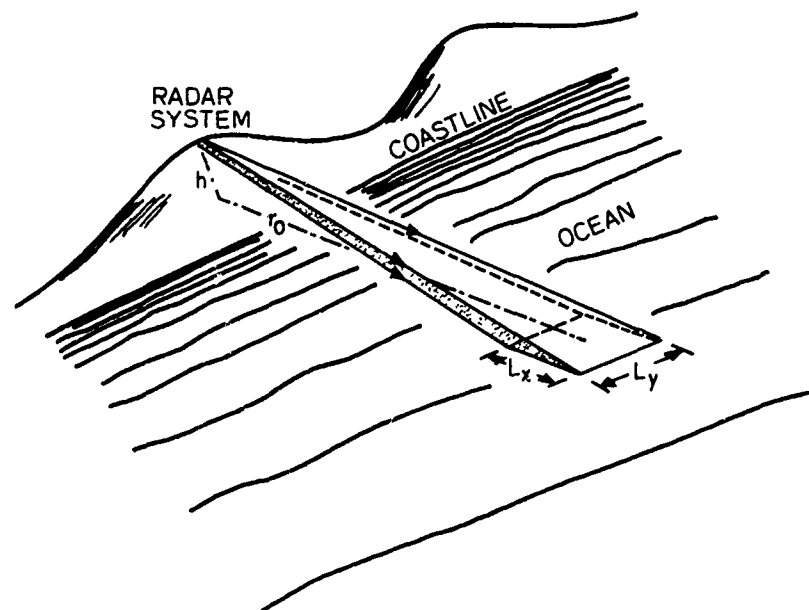


Fig. 4.1. RADAR ILLUMINATION OF THE OCEAN SURFACE.

transmit and receive antennas. To obtain spatial resolution in the radial direction, the radar is pulsed, and the width of each pulse determines the size L_x of the ocean patch in the radial direction.

Resonant radio-wave backscatter from the ocean surface occurs when the surface has a specific spatial structure; its wavelength must be one-half the wavelength of the radio wave, and its crests must be transverse to the radio-wave propagation direction. This Bragg-scattering phenomenon has been explained by detailed formulation of the scattering problem based on Rice's perturbation analysis of the boundary conditions [Rice, 1951] and the Stratton-Chu vector diffraction integral [Barrick, 1972]. To detect ocean current, the frequency of the backscattered signal but not its absolute amplitude is important. The following derivations based on simple wave-propagation concepts will demonstrate how this frequency is related to ocean current.

A. Physical Theory of First-Order HF Backscatter

Each pulse transmitted by the radar is represented by

$$s_n(t) = g(t - t_n) \exp(i2\pi f_c t)$$

where n signifies that the pulse is initiated at time $t = t_n$, and $g(t)$ is the pulse envelope with the rising edge at $t = 0$. The complex exponential is the analytic-signal representation of a sinusoidal waveform at carrier frequency f_c , and its phase is set arbitrarily to zero. Typically, many cycles of the sinusoid are contained in each pulse (a few hundred in the experiments).

The pulsed signal will propagate along the radial direction \underline{r} in the horizontal plane (see Fig. 4.2) and will scatter in all directions when it encounters the undulating sea surface denoted by $z = \eta(\underline{r}, t)$ where z is the vertical ordinate measured upward from the mean sea surface. The strength of the signal component scattered back toward the radar must be a function of the surface slope $\partial\eta/\partial r$ (henceforth denoted by η') along the general "look" direction of the radar. For small η' , the functional dependence of the backscattered signal on η' can be expressed as a Taylor series, and the leading term in this series expansion is η' . To

first order, therefore, the backscattered signal strength is proportional to η' .

In Fig. 4.2, the angle θ is measured from the beam axis of the radar, which is also the x axis. At any time t , the signal returning from the infinitesimal ocean-surface patch located at distance r and angle θ is proportional to the following factors:

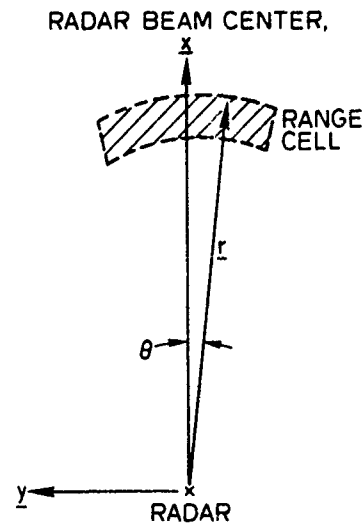


Fig. 4.2. DEFINITION OF THE COORDINATE SYSTEM.

- transmitted signal at time $t - 2r/c$, where c is the speed of light in free space, which takes into account the round-trip propagation delay of the radio wave
- ocean-wave slope $\eta'(\underline{r}, t - r/c)$, where time delay r/c signifies that the scattering surface is located distance r away
- area of the infinitesimal ocean-surface patch--namely, $rdrd\theta$
- combined directivity $G(\theta)$ of the transmit and receive antennas
- two-way propagation loss r^{-2} experienced by the radio wave

The received signal $s(t)$ is the sum of contributions from all infinitesimal ocean-surface patches covered by the radar,

$$s(t) = \int_{-\pi}^{\pi} d\theta G(\theta) \int_0^{\infty} r dr \eta'(\underline{r}, t - \frac{r}{c}) s_n(t - \frac{2r}{c}) \frac{1}{r^2}$$

The constant of proportionality has been ignored.

In the above integral, integration over r actually has finite limits as the result of the finite duration of the pulsed signal $s_n(t)$ whose pulsewidth is denoted by T_{pw} . Assume that $s_n(t)$ is zero

outside the time interval $(0, T_{pw})$; this same signal delayed by $2r/c$ will then have the following property:

$$s_n\left(t - \frac{2r}{c}\right) = \begin{cases} \exp\left(i2\pi f_c t - i2\pi f_c \frac{2r}{c}\right) g\left(t - t_n - \frac{2r}{c}\right) & t_n \leq t - \frac{2r}{c} \leq t_n + T_{pw} \\ 0 & \text{otherwise} \end{cases}$$

The expression for the received signal $s(t)$, therefore, simplifies to

$$s(t) = \exp(i2\pi f_c t) \int d\theta G(\theta) \int_{r_0 - L_x/2}^{r_0 + L_x/2} r^{-1} dr \eta'\left(\underline{r}, t - \frac{r}{c}\right) \exp(-i2\beta r) g\left(T_{DLY} - \frac{2r}{c}\right) \quad (4.1)$$

where

$$r_0 = \frac{c}{2} (T_{DLY} - T_{pw}/2) = \text{radial range of center of interrogated ocean patch measured from the radar}$$

$$L_x = \frac{c}{2} T_{pw} = \text{radial size of ocean patch}$$

$$\beta = 2\pi f_c / c = \text{free-space radio-wave wave number}$$

$$T_{DLY} = t - t_n = \text{fixed time delay}$$

As is evident above, the fixed time delay T_{DLY} is the sampling time of $s(t)$ measured from time t_n at which the most recent signal $s_n(t)$ was transmitted. The ocean patch located at range r_0 is also called the radar range cell.

Typically, r_0 varies from tens to a few hundred kilometers, and the linear dimension of the ocean patch is from a few to a few tens of kilometers; therefore, the one-way propagation delay r/c is on the order of milliseconds or less. Within this time period, no significant variation in the ocean-surface slope is expected. As a result, $\eta'(\underline{r}, t - r/c)$ can be replaced by $\eta'(\underline{r}, t)$, and the slowly varying function r^{-1} can also be replaced by r_0^{-1} . This yields

$$s(t) = r_0^{-1} \exp(i2\pi f_c t) \int d\theta G(\theta) \int_{r_0 - L_x/2}^{r_0 + L_x/2} dr \eta'(\underline{r}, t) \exp(-i2\beta r) w(r) \quad (4.2)$$

where $w(r) = g(T_{DLY} - 2r/c)$.

For ease of interpretation of this result, the circular coordinates (r, θ) are transformed into rectangular coordinates (x, y) with \underline{x} pointing in the beam-center direction (see Fig. 4.2). The beamwidth is assumed to be small so that

$$r \approx x \quad (4.3)$$

If the half-width of the antenna beam is θ_0 , the azimuthal extent L_y of the probed ocean patch is $L_y = 2r_0 \sin \theta_0$.

After integration by parts (see Appendix D),

$$s(t) = 2ir_0^{-2} \exp(i2\pi f_c t) \int_{-L_y/2}^{L_y/2} dy \int_{r_0 - L_x/2}^{r_0 + L_x/2} dx w(x) \cdot G(y) \beta \eta(x, y, t) \exp(-i2\beta x) \quad (4.4)$$

If antenna directivity $G(y)$ and the radial weighting function $w(x)$ are assumed to be constant, this twofold integral is proportional to the two-dimensional Fourier transform of the surface height at the wave-number set $(2\beta, 0)$ convolved with a two-dimensional spectral window with widths of approximately $2\pi/L_x \times 2\pi/L_y$.

In practice, both $G(y)$ and $w(x)$ are nonuniform functions and vary relatively slowly with their respective arguments. Their effects on the above integral are the same as the effects of the time window on the Fourier transform of a time series. As a result, resolutions in the spatial frequency domain are coarser than $2\pi/L_x \times 2\pi/L_y$; the degradation can be as large as a factor of 2 [Harris, 1978, for example]. The radar parameters can be chosen so that these resolution limits are much smaller than the observable spectral width, as in the Stanford four-frequency radar to be described in Chapter V. The resolution estimates $2\pi/L_x$ and $2\pi/L_y$, however, are useful order-of-magnitude approximations.

In the limits of large L_x and L_y , the integral in Eq. (4.4) representing the backscattering process becomes an infinitely sharp spatial filter at wave number $(2\beta, 0)$. Only one specific long-crested ocean-surface wave component is selected by this electromagnetic process, and this component has a wavelength L one-half the radio wavelength $\lambda = 2\pi/\beta$ and propagates along the radar beam axis. Because this radio-wave backscattering phenomenon is similar to Bragg scattering of x-rays from crystals [Brillouin, 1953], it is also called Bragg scattering.

At HF (3 to 30 MHz), the Bragg-selected ocean waves have wavelengths in the decameter range, and their slope magnitudes are smaller than unity even under fairly rough sea conditions. This, in turn, implies that $\beta\eta$ is small and that the first-order effect investigated here is dominant. This observation served as the basis for the perturbation calculations of Rice [1951].

In the expansion of r in Eq. (4.3), all terms of order higher than y/r_0 were neglected. The most important effect of these omitted higher order terms is in the phase of $\exp(-2i\beta r)$ in Eq. (4.2). An estimate of the upper bound on L_y above which Eq. (4.3) is not valid is obtained by limiting the maximum phase excursion caused by the second-order term to $\pi/4$. The result is approximately one-third the Fresnel-zone size $(r_0\lambda)^{1/2}$.

When L_y is larger than the Fresnel-zone size, the above theory can be modified by breaking up the integration in θ in Eq. (4.2) into a sum

of many integrations, each over a small range of θ . The local Cartesian coordinates are then defined for each of these small integration zones so that the local x axis is aligned with the axis of the zone (see Fig. 4.3). The azimuthal size of each zone is chosen to be small compared to the Fresnel-zone size so that the above theory is locally valid in each integration. The modified Bragg-scattering theory then states that the backscatter radar is sensitive to all ocean waves of length $\lambda/2$ and propagating in directions that fall within the antenna beam.

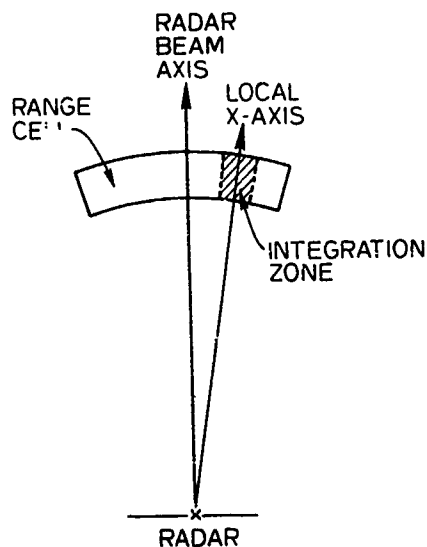


Fig. 4.3. INTEGRATION ZONES.

When Eq. (4.4) is valid and the width of the backscattering spatial filter is zero, the radar will detect only two ocean wave trains--one propagating toward the radar along its beam axis and the other propagating away from the radar. Both wave trains have a wavelength of $L = \lambda/2$, and their wave height can be represented as

$$\eta(x,y,t) = B_+(2\beta,0) \exp(i2\pi f_+ t + i2\beta x) + B_-(2\beta,0) \exp(i2\pi f_- t + i2\beta x) \quad (4.5)$$

Here, the subscripts + and - denote wave propagation toward and away from the radar, respectively, and B_+ and B_- designate the respective crest heights of the wave trains above the mean sea level. The frequencies f_+ and f_- are defined in Eq. (2.34) as

$$f_{\pm} = \pm f_B + \Delta \quad (4.6a)$$

$$f_B = \frac{(2g\beta)^{1/2}}{2\pi} \quad (4.6b)$$

$$\Delta = \frac{2}{\lambda} (4\beta) \int_{-\infty}^0 U_x(z) \exp(4\beta z) dz \quad (4.6c)$$

As discussed in Chapter II, f_B is the frequency of oscillation of the gravity waves in the absence of ocean current, Δ is induced by the current and, because the wave with positive frequency is propagating in the negative x direction according to Eq. (4.5), U_x is the current component in this same direction (pointing toward the radar).

Substituting the expression for the ocean wave height in Eq. (4.5) into (4.4) and ignoring the finite-resolution effect and some constants of proportionality, the following expression for the received signal is obtained:

$$s(t) = \exp\left[i2\pi(f_c + \Delta) t\right] \left[B_+(2\beta,0) \exp(i2\pi f_B t) + B_-(2\beta,0) \exp(-i2\pi f_B t) \right] \quad (4.7)$$

B. First-Order Doppler Spectrum

The Doppler spectrum of the received signal $s(t)$ is determined by taking a finite-time Fourier transform [see Eq. (3.4)] over a coherent integration time T of $s(t)$ and forming the magnitude squared of the result. Here, T is chosen to be large so that T^{-1} is not the limiting resolution in the spectrum.

In the absence of ocean current, the Doppler spectrum consists of two lines (of width T^{-1}) located at $f_c + f_B$ and $f_c - f_B$ (see Fig. 4.4a). Because the line at the higher frequency is the result of Bragg scattering from ocean wave trains propagating toward the radar, it is referred to as the approaching Bragg line and f_B as Bragg frequency.

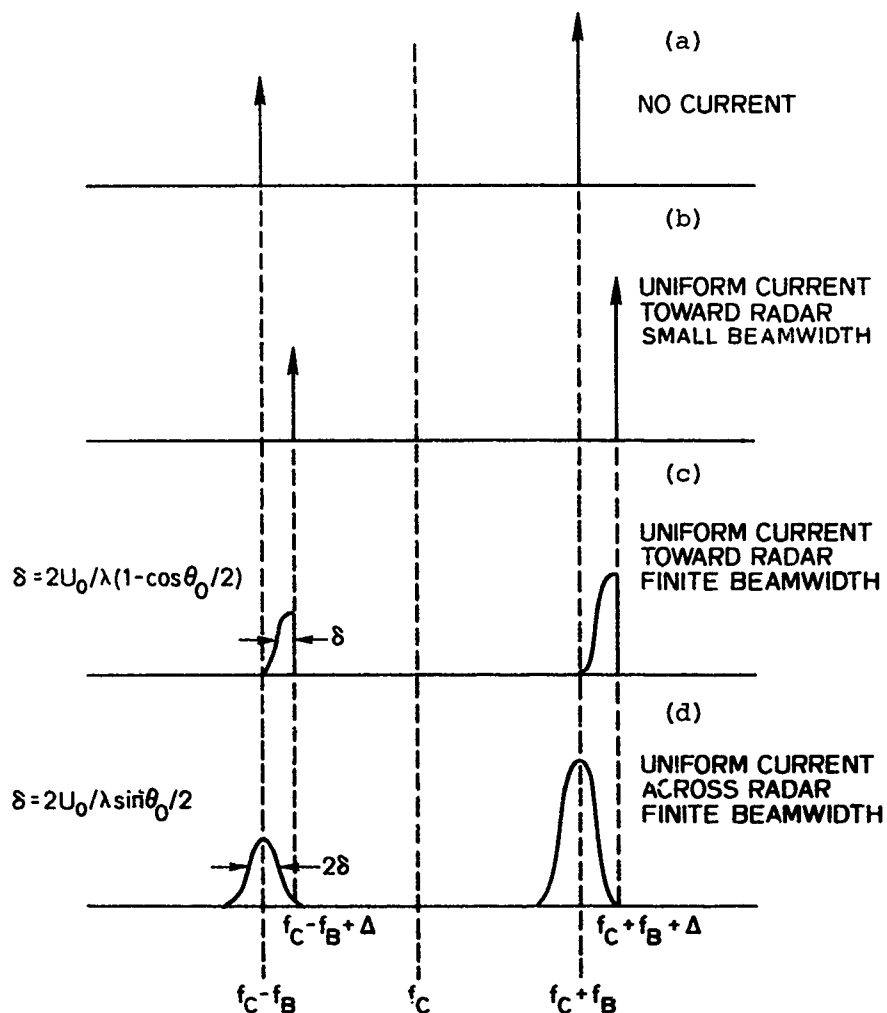


Fig. 4.4. THEORETICAL DOPPLER SPECTRA OF RADAR RETURN.

Based on the same reasoning, the line at the lower frequency is called the receding Bragg line. The ratio of the strength of the first Bragg line to that of the second is the ratio of the mean-squared wave height of the approaching wave train to that of the receding wave train.

In the presence of ocean current, both Bragg lines are Doppler shifted by the amount Δ which is proportional to the ocean-current component U_x (in the direction toward the radar) averaged over depth with an exponential weighting function. The problem of detecting ocean current that varies with depth z will be discussed in Chapter VII. To simplify in this section, U_x is assumed to be uniform with depth, and $\Delta = 2U_x/\lambda$. The displaced Bragg lines are illustrated in Fig. 4.4b.

As discussed in Section A, the above model is valid if L_y is smaller than the Fresnel-zone size. It has been demonstrated that, when L_y is many times this limiting size, $s(t)$ is the sum total of all contributions of backscatter from ocean waves of wavelength $\lambda/2$ propagating in all directions that fall within the antenna beam,

$$s(t) = \exp(i2\pi f_c t) \int G(\theta) \left\{ B_+ \exp[i2\pi(f_B + \Delta)t] + B_- \exp[-i2\pi(f_B - \Delta)t] \right\} d\theta \quad (4.8)$$

Here, $\Delta = -2\hat{r} \cdot \underline{U}/\lambda$, where \hat{r} is the unit vector along the radial direction from the radar. The current vector \underline{U} is the total horizontal current which is considered uniform with depth. The ocean-wave directional spectrum (defined in Chapter III) is assumed to be omnidirectional within the radar beam so that $|B_{\pm}|^2$ are independent of θ .

If \underline{U} is uniform within the ocean patch probed by the radar, the shape of the broadened Bragg lines can be predicted if the direction of current flow is known. For a uniform current of magnitude U_0 flowing down the radar beam (in the negative x direction in Fig. 4.2), the current-induced Doppler frequency Δ will take on values ranging from $(2U_0/\lambda) \cos \theta_0$ to $2U_0/\lambda$, where θ_0 is the half-width of the radar beam. Assuming a gaussian beam, the Doppler spectrum is illustrated in Fig. 4.4c. For the same current flowing across the radar beam (in the y direction in Fig. 4.2), Δ then takes on values from $-(2U_0/\lambda) \sin \theta_0$ to $(2U_0/\lambda) \sin \theta_0$. The resulting spectrum is shown in Fig. 4.4d.

Observed with a finite radar beamwidth, the maximum width of each Bragg line attributed to \underline{U} is $(4U_0/\lambda) \sin \theta_0$. If the ocean current is random and has a statistical standard deviation σ_v , the Bragg width resulting from this random component is on the order of $2\sigma_v/\lambda$.

Two other aspects of the ocean-surface processes that can cause broadening of the Bragg lines are the coherent length of the long-crested waves and higher order ocean-wave interactions.

1. Effects of Finite Coherent Length of Long-Crested Waves

As the pulsed radar interrogates the surface of an inhomogeneous sea within a range cell of finite size for a finite duration T , long-crested waves with different heights may move into view. For waves with a wave number of 2β , group velocity is $v_g = 1/2(g/2\beta)^{1/2}$ and the time required for them to move through the entire patch of length L_x is $t_c = L_x/v_g$. During this interval, the radar essentially samples the same ocean patch and the spectral amplitude B_{\pm} should be approximately constant; that is, the correlation time of the Bragg amplitude should be larger than t_c . The width of the Bragg line is therefore narrower than t_c^{-1} if t_c is smaller than the coherent integration time T . Actually, t_c^{-1} is the limiting resolution of the finite-space transform because v_g is the ratio of the resolution in radian frequency to the resolution in wave number.

Implicit in the above discussion is the use of the first-order dispersion relationship which states that, for a particular wavelength, there can be only two frequencies $\pm f_B$ in the absence of current; the variation of the Bragg-selected wave amplitude with time is deterministically sinusoidal. It should be emphasized that this dispersion relationship is valid only for steady-state conditions. If the wind changes significantly within the coherent integration time T , an additional temporal variation in the wave amplitude can be expected.

2. Higher Order Ocean-Wave Interactions

The derivation of the ocean-wave dispersion relationship in Chapter II considered only the terms linear in the wave height η . Stokes [1847], Longuet-Higgins and Phillips [1962], Johnstone [1975], Huang and

Tung [1976], and Weber and Barrick [1977] have investigated the effects of higher order terms in the hydrodynamic equations. Some of their relevant results are summarized in this section.

Second-order interactions produce a dispersion relationship $\omega = \omega(\underline{k})$ that has a continuum of roots at the specific Bragg-selected wave-number vector $\underline{k} = (2\beta, 0)$. Fortunately, this continuum excludes a region centered at the first-order Bragg frequencies $\omega_B = \pm\sqrt{2g\beta}$ because of the low-frequency cutoff in the wave-height spectrum of the ocean. The second-order energies thus spread themselves in a continuous frequency range outside the first-order Bragg lines.

Third-order interactions change the phase speed of all long-crested waves, including the Bragg-selected wave of wave number $(2\beta, 0)$. The self-effect (the nonlinear effect in the presence of only the Bragg wave itself) is an increase in its phase speed by a fraction equal to $1/2(2\beta a)^2$ where a is its height. This is called "Stokes current." Waves with various wave numbers moving in parallel or opposite to this Bragg wave increase or reduce its phase velocity, respectively.

Barrick and Weber [1977c] postulate that, because this phase-speed change is dependent on the ocean wave-height which can be considered a random variable, it has a finite variance that will manifest itself as the width of the Bragg line. By considering only the effects of colinear waves (long-crested waves moving parallel or antiparallel to the Bragg-selected wave), they simplified their general but complicated results to a tractable form. For a 30 knot wind and a 5 m ocean wave, they obtained a phase-velocity correction of 5 percent and a standard deviation (normalized by the first-order velocity) of 0.05 percent. This correction based on mutual interactions will have a sign that depends on the wave direction relative to the wind; waves moving with the wind are speeded up, and waves moving against the wind are slowed. The radar cannot distinguish this correction from ocean current. The 0.05 percent standard deviation is also too small to be resolvable by the radar.

Chapter V

PESCADERO EXPERIMENTS

Since May 1975, ocean backscatter experiments have been conducted at a site located near Pescadero on the northern California coast. From May through December 1975, the experiments were run approximately four times each month, and a typical day consisted of four half-hour runs, each with a different radar pulse width. Similar experiments were carried out during June 1976 and January 1977 with nominal radar frequencies of 4.8, 6.6, 13.3, and 21.7 MHz. Based on the decision to examine second-order interactions at higher frequencies, 4.8 MHz was changed to 29.8 MHz. Several experiments followed during August and September 1977 and January 1978 and, at that time, the radar pulse width was fixed at 50 μ sec as a trade-off between the signal-to-noise ratio and spatial resolution. Approximately four hours of data were collected daily, and concurrent in-situ measurements of ocean-current shear were obtained by deploying spar buoys of various lengths and then tracking their motions.

The Stanford four-frequency radar system used for data collection is described in Section A. The data-processing procedure by which the sea-echo Doppler spectrum was obtained and the subsequent scheme developed to retain only the first-order Bragg signal are discussed in Section B. Possible artifacts introduced by the radar system will be examined in Section C, and the in-situ measurements are analyzed briefly in Section D.

A. Stanford Four-Frequency Radar

The Stanford radar system is coherent in that both the transmitter and receiver are driven by the same free-running stabilized oscillator at a frequency of 30 MHz. Four separate phase-locked-loop frequency synthesizers generate the transmitted radar frequencies which can be changed in steps of 10 kHz from the front panel over a range of approximately 100 kHz. These frequencies can be adjusted to minimize man-made interference.

The transmit antenna is a vertical half-rhombic, approximately 250 m long and 45 m high at the apex, supported by a helium-filled balloon. It is located on a flat piece of land 40 m above sea level. The vertical

plane containing the half-rhombic (referred to as the antenna plane) is in the direction of $315^{\circ}T$, along which the radar system is about 1200 m from shore. The antenna wire at its fixed ends has roughly 1 m of slack, and the tension is taken up by surgical tubing; motion of this wire in the antenna plane is thus limited. The half-rhombic is supported by two guy wires transverse to the antenna plane. Motion in this transverse plane is again limited; however, the lack of elastic support permits larger motions here than in the antenna plane. The advantage of this transmitter system is its relatively high gain and small beamwidth over a wide range of frequencies.

The receive antenna is a 1 m wideband loop located 50 yards downhill from the transmit antenna in the direction transverse to the plane of the half-rhombic. The plane of the loop is approximately parallel to the plane of the rhombic so that, coupled with shielding by the landscape, the direct effect of the transmitted pulses is minimized although not completely eliminated (see Section C).

In Fig. 5.1, the measured 3 dB beamwidth of the combined receive-transmit system is plotted vs frequency. At 5 MHz, the beamwidth is approximately 25 degrees; at 30 MHz, it is roughly 12 degrees. The measured beam center moves from $320^{\circ}T$ at 30 MHz to $290^{\circ}T$ at 4 MHz as the result, most likely, of the wavelength-dependent guiding effect of the surrounding landscape and the effective attenuation of the radio wave as it propagates over land. As illustrated in Fig. 5.2, the radio wave propagates over greater stretches of land on the north side of the antenna beam axis than it does on the south side. At the lower frequency where the antenna beamwidth is large which highly accentuates this asymmetry, the direction of maximum antenna gain thus appears to have moved south from $315^{\circ}T$.

The radar is pulsed; a trapezoidal pulse is transmitted every 400 μ sec. The nominal pulse width T_{pw} (defined as the width between the half-power points) is selectable from the front panel to be 10, 25, 50, 100, or 200 μ sec. Four different carrier frequencies in the HF band of 3 to 30 MHz are time multiplexed in the pulse train so that a pulse of the same frequency repeats every 1.6 msec (see Fig. 5.3). The peak RF power output is approximately 40 W.

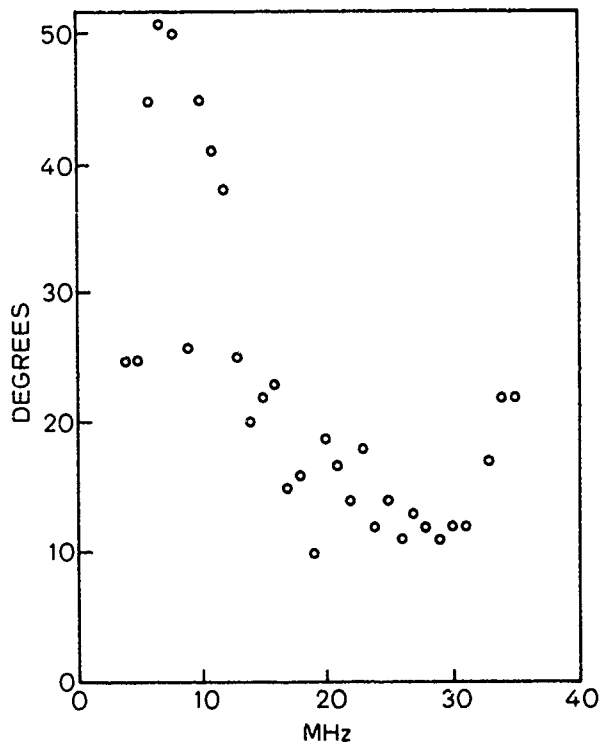


Fig. 5.1. MEASURED 3 dB FULL WIDTH OF COMPOSITE ANTENNA BEAM VS RADAR OPERATING FREQUENCIES.

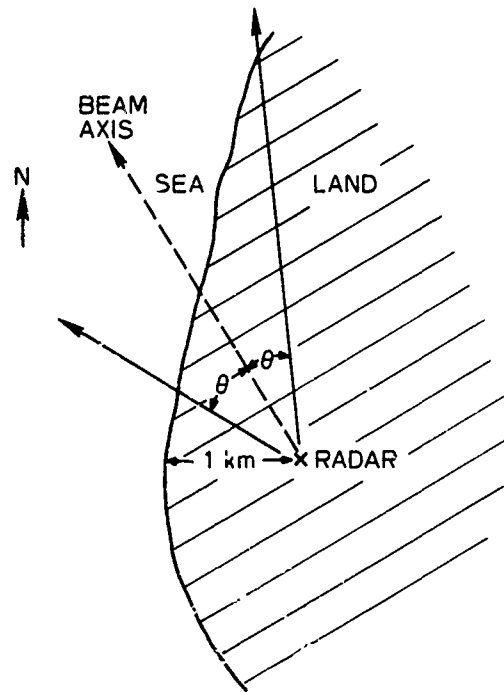


Fig. 5.2. PROPAGATION PATHS OVER LAND. This is a rough sketch of the actual coastline; small-scale details are ignored.

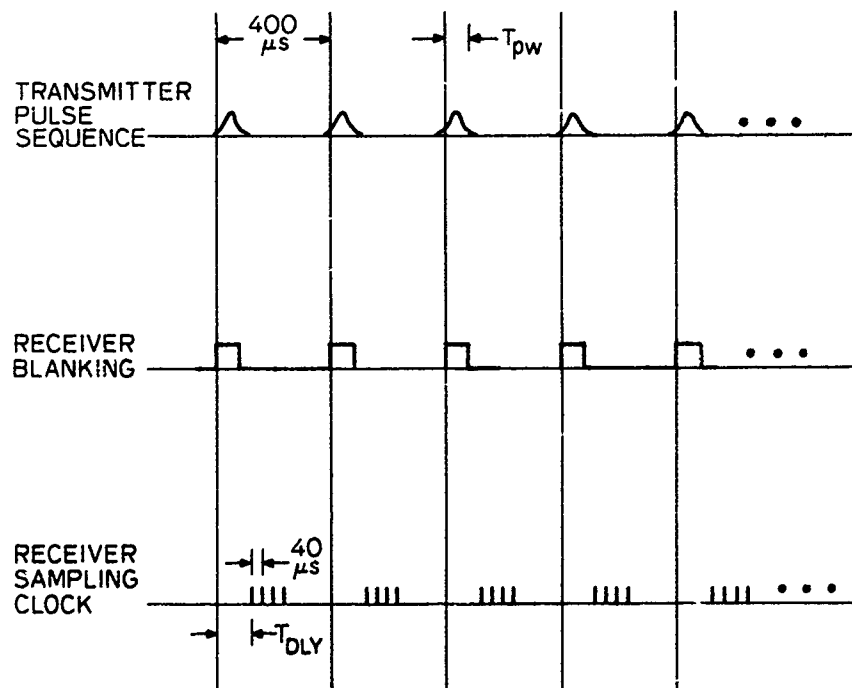
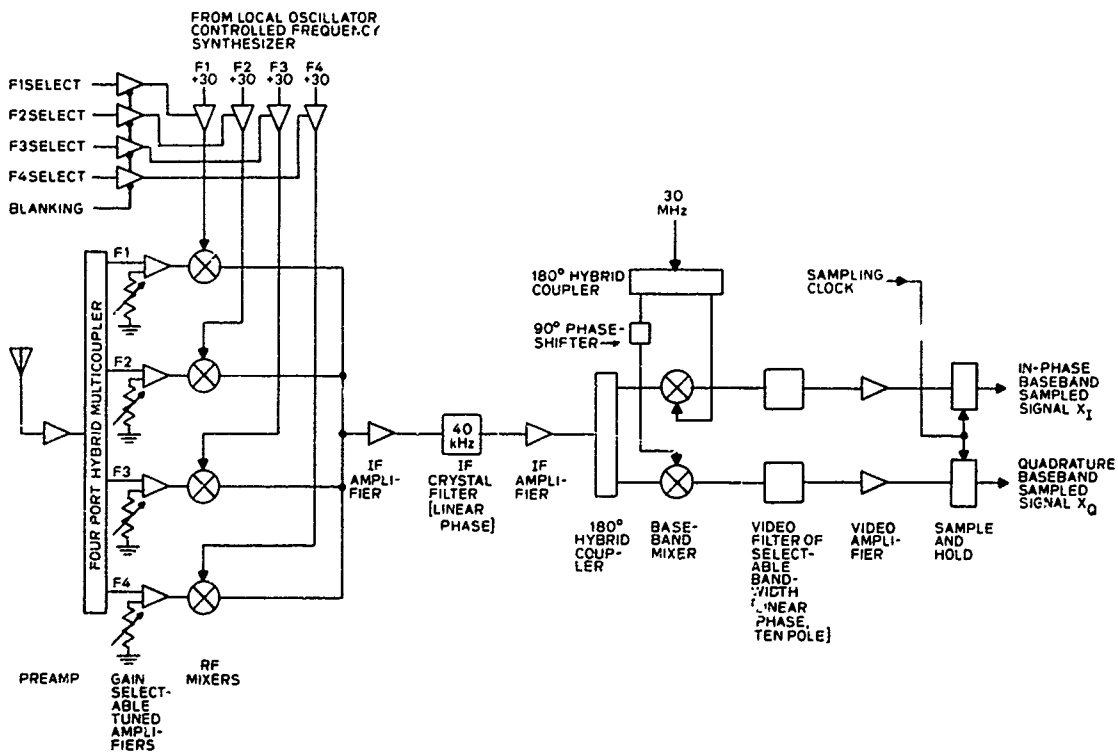
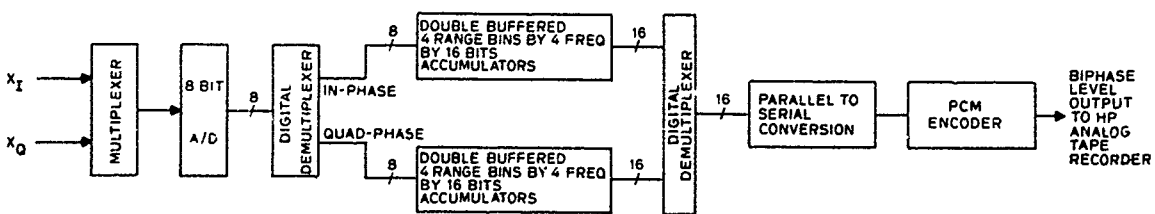


Fig. 5.3. TIMING SEQUENCE OF THE RADAR.

The receiver system is shown in Fig. 5.4. The first stage of amplification and mixing requires four channels--one for each radar frequency. The local-oscillator signal for each channel is turned off during a blanking period lasting through the width of the transmitted pulse and is turned on once every 1.6 msec when the preceding carrier frequency is 30 MHz below the oscillator frequency.



a. Dual-conversion superheterodyne analog system



b. Digital system

Fig. 5.4. RECEIVER SYSTEM FOR THE STANFORD FOUR-FREQUENCY RADAR.

The signal at the intermediate frequency is then passed through an amplifier chain and a crystal filter whose width is approximately 40 kHz. The second conversion stage mixes the signal to the final intermediate frequency of 0 MHz. Two parallel mixers driven by local oscillators that differ in phase by 90° are used to distinguish between the return signal Doppler shifted below and above the transmitted frequency. The two channels are designated the in-phase channel (I) and quadrature-phase channel (Q).

After passing through identical filters and amplifiers, these signals are sampled simultaneously at time delays of typically 90, 130, 170, and 210 μsec measured from the leading edge of the transmitted pulse. Each delay corresponds to $t - t_n$, as discussed in Chapter IV. Based on Eq. (4.1), the centers of the four range cells interrogated are at 9.75, 15.75, 21.25, and 27.75 km, respectively, from the radar, assuming a pulse width of 50 μsec .

The two samples at each range bin are digitized sequentially by an 8-bit A/D converter. Each sample is then stored in a 16-bit accumulator designated for the in-phase or quadrature-phase channel and a specific range bin and radar frequency. There are two sets of 32 accumulators each; in each accumulator, N (typically 140, set from front panel) samples are added together. While one set is waiting for N time samples to accumulate, the contents of the second set will be encoded into a digital waveform and recorded on an analog tape recorder. Included in the data stream are the settings of all the front-panel selector switches and an internal clock.

The summing of 140 time samples lowers the sampling rate to $(140 \times 1.6 \times 10^{-3})^{-1} = 4.464$ Hz and reduces the effect of white noise because the operation is equivalent to a lowpass filtering process. The filter function is periodic with period $(1.6 \times 10^{-3})^{-1} = 625$ Hz. Each period contains a sinc function with its first zeros at ± 4.464 Hz, and the signal falls within the mainlobe of that function. The effect of this filter is thus to reduce the white-noise power by a factor of 140.

If the model in Eq. (4.7) is used to denote the signal arriving at the receiver front end, the first-stage and final-stage IF signals $s_1(t)$ and $s_2(t)$ can be written as

$$s_1(t) = \exp\left[i2\pi(3 \times 10^7) t\right] \left\{ B_+ \exp\left[i2\pi(f_B + \Delta) t\right] + B_- \exp\left[-i2\pi(f_B - \Delta) t\right] \right\}$$

+ complex conjugate (5.1a)

$$s_2(t) = B_+ \exp\left[i2\pi(f_B + \Delta) t\right] + B_- \exp\left[-i2\pi(f_B - \Delta) t\right] \quad (5.1b)$$

Here, B_+ and B_- are the amplitudes of the ocean wave train at wavelength $\lambda/2$ propagating toward and receding from the radar, respectively, and Δ is the current-induced Doppler shift given by Eq. (4.6c). The in-phase channel is assumed to be the real part of a complex number and the quadrature phase channel is the imaginary part.

From Eq. (4.6b), the Bragg frequency f_B is

$$f_B = 0.102023 \sqrt{f_C} \text{ Hz} \quad (5.2)$$

where f_C is the radar carrier frequency in megahertz. The values of f_B for the five nominal radar frequencies used in the experiments are tabulated in Table 5.1, together with the wavelength and phase velocity of the Bragg-resonant ocean surface waves.

Table 5.1

CHARACTERISTICS OF BRAGG-SELECTED OCEAN WAVES.
Bragg frequency f_B is from Eq. (5.2).

Radar Frequency (MHz)	Ocean-Wave Wavelength (m)	Phase Velocity (m/sec)	Bragg Frequency (Hz)
4.8	31.25	6.99	0.224
6.7	22.39	5.91	0.264
13.3	11.28	4.20	0.372
21.7	6.91	3.29	0.475
29.8	5.03	2.80	0.557

B. Data Reduction

To obtain the first-order signal from the recorded data, these data are reduced through the following steps.

Step 1

The recorded signal is played back through a PCM decoder that recovers the clock signals and converts the serial data stream into 8-bit data words. These data words include, for example, front-panel settings, radar frequencies, and pulse width. The decoded data are stored on a nine-track magnetic tape.

Step 2

Depending on the frequency resolution desired, a corresponding number of data samples are extracted from the magnetic tape for each range bin and carrier frequency and are stored temporarily as 16 sets of data on the disk. The observed current-induced Doppler shift ranges from a few cm/sec to 40 cm/sec. To resolve the small current and still retain reasonable time resolution requires a coherent integration time of 917.504 sec which corresponds to $2^{12} = 4096$ complex pairs of time samples for each Fourier transform. Because of computer-memory limitations, the number of samples is reduced by a factor of 2 by replacing every two adjacent time-sample pairs by their sum; the effective sampling rate therefore becomes 2.232 Hz. The data sets are then retrieved from the disk storage, one set at a time, and the following processing is performed on the selected data set.

Step 3

The temporary loss of synchronization in step 1 will result in erroneous data values. The frequency of occurrence of this event is minimized by selecting a unique synchronization pattern. When this loss occurs, it affects only the associated data frame consisting of 16 time-sample pairs--one for each range bin and each radar carrier frequency. To remove such data spikes, an algorithm is devised whereby the mean \bar{s} and standard deviation σ of the channel (in-phase or quadrature-phase) are computed,

the data in that channel are searched, and all data points that deviate from the mean \bar{s} by more than 3 σ are eliminated. In this step, the mean is removed from each channel.

Step 4

A Hamming window is then applied to the in-phase and quadrature-phase channels in the data set of 2048 complex pairs. This window produces a spectral resolution of approximately one-half that of a rectangular window (2.2 millihertz); however, the spectral sidelobes are lower than that of the rectangular window by 30 dB [Harris, 1978].

Step 5

This set of windowed data is then Fourier transformed, using the Cooley-Tukey algorithm of the fast Fourier transform (see, for example, Rabiner and Gold, p. 367). The power (Doppler) spectrum is obtained by taking the sum of the squares of real and imaginary parts of the transformed data. The results are stored on a nine-track magnetic tape.

Step 6

The processing steps 3 through 5 are repeated for each of the data sets stored on the disk.

Step 7

Power spectra are obtained at time increments of one-half the coherent integration time (approximately 7-1/2 min). This is possible because of the 50 percent overlap in the data used in the transform; that is, the latter half of the data used in obtaining the power spectrum of a previous time interval becomes the first half of the data for the present time interval. Preferential weighting of the Hamming window suppresses information contained at the outer edges of the window, and the 50 percent time overlap recovers this lost information.

Step 8

The large variability (or jaggedness) of the individual power spectra indicates the randomness of the ocean-surface process. In fact, the power spectral estimate behaves as a chi-square with four degrees of freedom (see Appendix A). To reduce this variability, a smoothed spectrum is obtained by convolving it with a gaussian window whose width at $1/e$ (or 4.34 dB) is chosen to be proportional to the square root of the carrier frequency. This frequency dependence is based on the observed behavior of the Bragg width (see Chapter VIII). In terms of frequency bins, each 1.09 millihertz in size, this window width is 8 bins at 4.8, 10 bins at 6.8, 13 bins at 13.3, 17 bins at 21.8, and 21 bins at 29.75 MHz. Because the original unsmoothed spectrum is used in the actual determination of the Bragg-line position, these smoothing widths are not critical.

In the typical smoothed spectra in Fig. 5.5, narrow bands of strong signals can be observed at frequencies to within a few percent of $\pm f_B$. As discussed in Chapter IV, the band of signals near $+f_B$ is energy scattered from ocean waves propagating toward the radar and, for brevity, are called the approaching Bragg line; the band near $-f_B$ is called the receding Bragg line for similar reasons. In the immediate neighborhood of each band, a continuum of lower level signals attributed to second-order electromagnetic and hydrodynamic effects [Tyler et al, 1974; Barrick, 1972; Johnstone, 1975] is frequently found and, most often, it is separated from the first-order band by a sharp null. On days of relatively calm sea and particularly at the farthest range cells, this second-order continuum is completely submerged in system noise which is approximately white. In either case, further analysis of the first-order bands is necessary, and this is made possible by a frequency-domain filtering scheme that can be applied to either first-order band.

Step 9

Examination of the Doppler spectra derived from the entire Pescadero data set reveals that the current-induced Doppler shift corresponds to an effective uniform current having a magnitude of no more than 50 cm/sec. This fact is used in the search for the peaks of the Bragg signals.

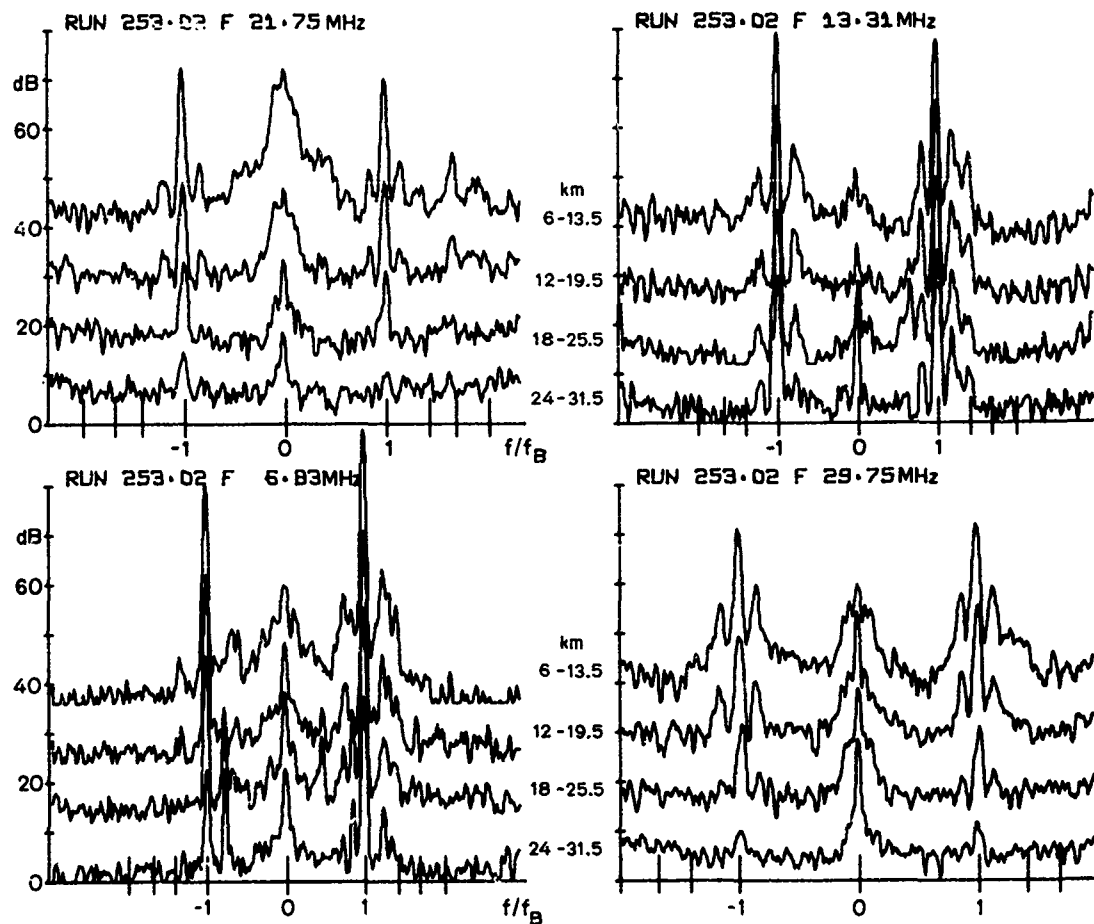


Fig. 5.5. SMOOTHED DOPPLER SPECTRA AT FOUR RADAR FREQUENCIES AND FOUR RANGE CELLS. Data were collected on 25 January 1978.

The purpose of the frequency-domain filtering scheme is to determine the cutoff points on either side of the band peak. An algorithm has been developed that looks at the local slopes of the logarithm of the smoothed spectrum. Each is computed as the slope of the linear fit to a number of spectral points, and the number is the same as that for the smoothing window. On one side of the peak, the slope must be positive and on the other side it should be negative. This scheme establishes the point on the positive-slope side at which the local slope becomes smaller than a positive preselected cutoff value and the point on the negative-slope side where the local slope becomes larger than a negative cutoff value. These two points then define the limits of the first-order band. The magnitude of the cutoff value is 0.3 dB/millihertz.

Note that the smoothed spectrum is used to obtain the cutoff points. These can then be considered as the lower and upper frequency cutoffs of a rectangular filter to be applied to the original unsmoothed spectrum; that is, they define the first-order band in the unsmoothed spectrum. Figure 5.6 is a block diagram of this process.

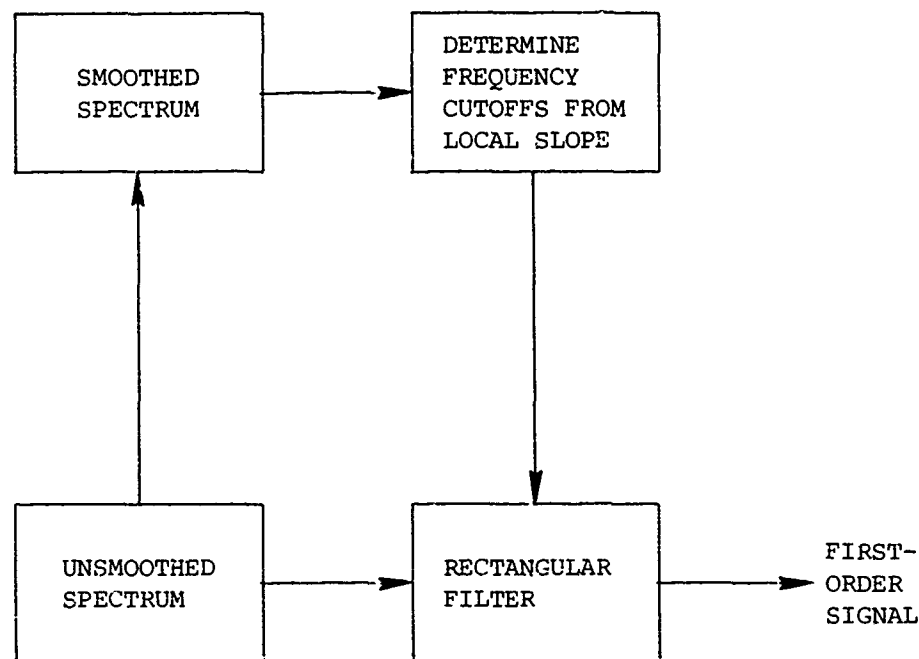


Fig. 5.6. RETRIEVAL OF FIRST-ORDER SIGNAL FROM DOPPLER SPECTRUM OF SEA ECHO.

C. System-Introduced Artifacts

1. Effects of Transmit-Antenna Motion

A disadvantage of a balloon-supported antenna is that its motions may broaden the spectral lines. To understand this, the following extension of Eq. (5.1b) is used as a model for the postdetection signal:

$$\begin{aligned}
 s_2(t) = & A_P(t) \left\{ B_+ \exp \left[i2\pi(f_B + \Delta) t \right] + B_- \exp \left[-i2\pi(f_B - \Delta) t \right] \right\} \\
 & + A_D(t) + A_L(t) + D
 \end{aligned} \tag{5.3}$$

Here, $A_p(t)$ is the transmitted signal whose amplitude slowly varies with time because of the motions of the antenna in the vertical plane containing the beam axis. The receive antenna is inevitably sensitive to the tail of the transmitted pulse that continues through the receive period. This results in a detected direct signal $A_D(t)$ whose time variation is caused by the motion of the half-rhombic in a vertical plane transverse to the beam axis. This signal is expected to decay with range as the transmit pulse tapers off with time. The component $A_L(t)$ is caused by the direct reflection from stationary targets; its temporal variation follows the antenna motion along the line-of-sight path to the stationary target. The constant term D is entirely the result of leakage of the 30 MHz local-oscillator frequency into the signal path within the radar box; this appears as a line in the Doppler spectrum at zero frequency, and its magnitude is several orders higher than $A_D(t)$ and $A_L(t)$.

The general modulation function $A(t)$ is proportional to $\exp[j2\pi L(t)/\lambda]$, where $L(t)$ is the time-varying component of the path-length from the source to the receiver, and λ is the radio wavelength. If $L(t)$ has amplitude L_0 and frequency of oscillation f_A then, for small L_0/λ , the spectrum of $A(t)$ consists of lines with amplitudes on the order of $(L_0/\lambda)^n$ at frequencies of $f_n = \pm n f_A$, $n = 0, 1, \dots, \infty$. For actual random antenna motions, the spectral width of $A(t)$ is roughly $(\bar{L}/\lambda) \cdot 1/T_A$, where \bar{L} is the average amplitude and T_A is a representative time scale. The effect of antenna motions, therefore, increases with radar frequency.

The resulting Doppler spectrum from Eq. (5.3) will consist of bands of energy at $\pm f_B$ and at dc where width is dictated by transverse motions with higher amplitude, as discussed in Section A; this is very apparent at higher radar frequencies under moderate-to-high wind conditions (see Fig. 5.5). Note that the effect of D has been removed. At $\pm f_B$, there is a convolution of the antenna motion-induced spectrum and the ocean wave-induced and current-induced spectrum. If the system artifact is dominant, the bands at $\pm f_B$ are expected to exhibit structures similar to that of the spectrum of antenna motions in the plane of the half-rhombic, and the following statements should then be true of the observed energy bands at $\pm f_B$.

- The structures of the spectral bands at $\pm f_B$ must be similar.
- Band structures must not vary with range from the radar.

In Fig. 5.7, the fine-scale structures of the approaching and receding Bragg lines are shown by plotting the portions of the unsmoothed spectra centered at $\pm f_B$. Note that, at either of the two radar frequencies, the spectra are dissimilar at different ranges and that the approaching and receding lines do not exhibit the same characteristics. For example, at 21.75 MHz, the widths of the receding Bragg lines are significantly larger than those of the approaching lines and, at 29.75 MHz, the width of the approaching lines at the near range is much smaller than that at the farther range. Such dissimilarities between the receding and approaching Bragg lines and between those at various range cells are continuously observed in the Doppler spectra obtained from the Pescadero data. As a result, it is unlikely that antenna motions in the plane of the half-rhombic are large enough to increase significantly the width of the Bragg lines.

Even if antenna motions are large enough to increase the width of the Bragg line, they cannot change the mean position of that line because they are zero-mean random motions.

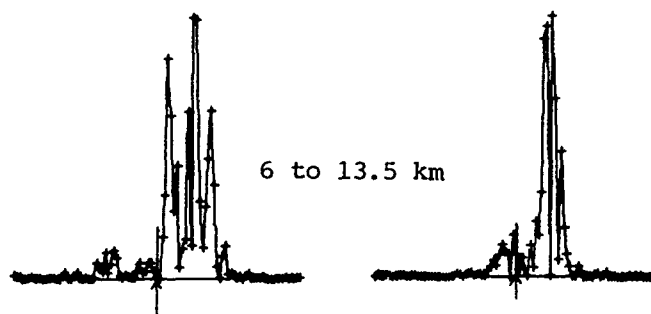
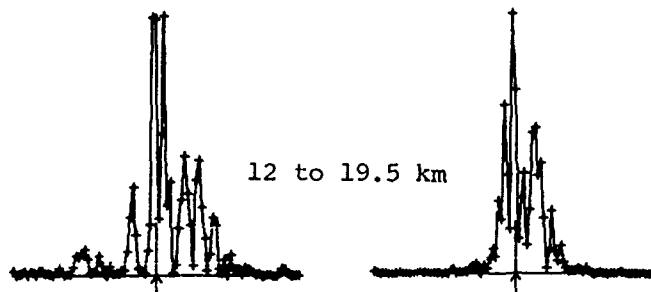
2. Local-Oscillator Instability

It has been suggested that the spectral width of the land echo is a measure of the local-oscillator (LO) stability. This echo, reflected from a stationary object, is at the frequency of the transmitted signal. It thus appears at zero frequency (dc) after IF conversion, and its width is determined by the stability of the local oscillator over its time of flight which is on the order of tens of microseconds.

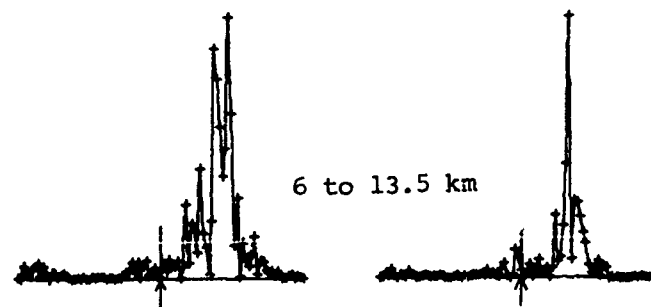
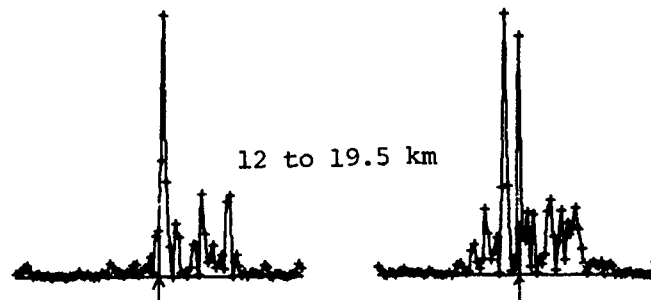
As evident from Eqs. (5.1b) and (5.2), the Bragg signal will be affected by the variation of the oscillator frequency over the integration time of 15 min required to produce the Doppler spectra. By differentiating Eq. (5.2), it can be shown that the percentage change in the carrier frequency is twice that in the Bragg frequency. Typical values for the Bragg frequency and Bragg width are 500 and 10 millihertz, respectively. If this

RECEDING LINES

APPROACHING LINES



a. At 21.75 MHz from first two range cells



b. At 29.75 MHz from first two range cells

Fig. 5.7. FINE-SCALE STRUCTURES OF RECEDING AND APPROACHING BRAGG LINES. Frequency spacing between adjacent points is 1.09 millihertz. Data taken on 20 January 1978 at approximately 12:00 local time.

width is caused by LO instability, the oscillator frequency must have drifted by 4 percent in 15 min, an amount exceeding typical LO stability specifications by several orders of magnitude.

The long-term frequency stability of the Stanford radar system has actually been checked by feeding through it a CW signal generated by an independent HP synthesizer. The resolution of the detected signal was found to be limited by the finite transform length.

3. Nonlinear Amplification

During the initial experiments, spectra at the first range cell frequently displayed Bragg lines symmetrically positioned about dc (but not at $\pm f_B$) and of identical structures. This cannot be a real effect because the receding waves are not expected to be highly correlated with the approaching waves. Initially, an imbalance between the in-phase and quadrature-phase channels was suspected, but this imbalance was found to be too small to be significant. The actual source was nonlinear amplification in the first IF stage. The signal at the first range cell coupled with the directly received tail of the transmit pulse drove the second IF amplifier into the nonlinear region. Consider a signal $s_1(t)$ where

$$s_1(t) = A \exp(i2\pi f_{IF} t) + A^* \exp(-i2\pi f_{IF} t) \\ + B \exp[i2\pi(f_{IF} + f_B) t] + B^* \exp[-i2\pi(f_{IF} + f_B) t] \quad (5.4)$$

The second-order products of this nonlinear amplification will contain terms that can be converted into a signal at $2f_B$ in the final IF stage. The third-order products include $A^2 B^* \exp[i2\pi(f_{IF} - f_B) t]$ which translates into a signal at $-f_B$ after quadrature detection. This illustrates how part of the energy of a signal that normally appears at $+f_B$ can leak into $-f_B$.

This problem has been corrected by modifying the IF amplifiers. It affected only some data at the first range cell and, even then, the higher energy Bragg line should not be influenced.

4. Finite Range-Cell Size

As discussed in Chapter IV, the finite range-cell size $L_x \times L_y$ implies that the width of the two-dimensional spatial Bragg filter is $\Delta k_x \times \Delta k_y$ where, to a good approximation, $\Delta k_x = 2\pi/L_x$ and $\Delta k_y = 2\pi/L_y$. To translate this spatial-frequency width into $\Delta f = \Delta\omega/2\pi$ in the frequency domain, a small change Δk in the wave number is related to a small change $\Delta\omega$ in the wave frequency through the wave group velocity v_g ,

$$\Delta\omega = (\Delta k) v_g$$

where Δk is the magnitude of the vector with components $\Delta k_x, \Delta k_y$. If

$$L = \left(L_x^{-2} + L_y^{-2} \right)^{-1/2}$$

the expression for Δf is

$$\Delta f = \frac{v_g}{L} = \frac{1}{2} \frac{v_p}{L} \quad (5.5)$$

where v_p is the wave phase velocity tabulated in Table 5.1. The worst-case Δf occurs at the lowest radar frequency of 4.8 MHz and the shortest pulse width of 25 μ sec. For a distance of 15 km and a beamwidth of 30° (see Fig. 5.1), $L_y \approx 7.5$ km and $L_x \approx 3.8$ km so that $f \approx 1$ millihertz. This worst-case Δf is slightly smaller than the resolution cell of the 918 sec transform. The effect of finite range-cell size, therefore, is not observable in the data.

D. In-Situ Measurements of Ocean Current by Spar Buoys

Concurrent in-situ drifter measurements of the ocean current were obtained during several of the radar experiments. The drifters were four lengths of spar buoys built of plastic pipes loaded with an appropriate amount of lead shot so that they immersed upright in water to predetermined depths of 1, 3, 6, and 12 m, respectively.

The locations of the buoys were determined by a microwave tracking system whose range resolution was on the order of a few meters. As

illustrated in Fig. 5.8, two microwave transponder (or range) stations were located at Pillar Point and Pescadero, respectively. A boat used to deploy the buoys also housed the master station that continuously interrogated the two transponders on the coast and determined the distance of the boat from each range station by monitoring the round-trip time delay of the microwave signals. The position of each buoy was measured by carefully pulling the boat to within a few meters of it and then noting the distances displayed on the tracking system. These measurements, taken at time intervals of an hour or longer, determined the mean drift velocity of each buoy. Because this drift was typically on the order of 1 km, the uncertainty introduced was less than 1 percent.

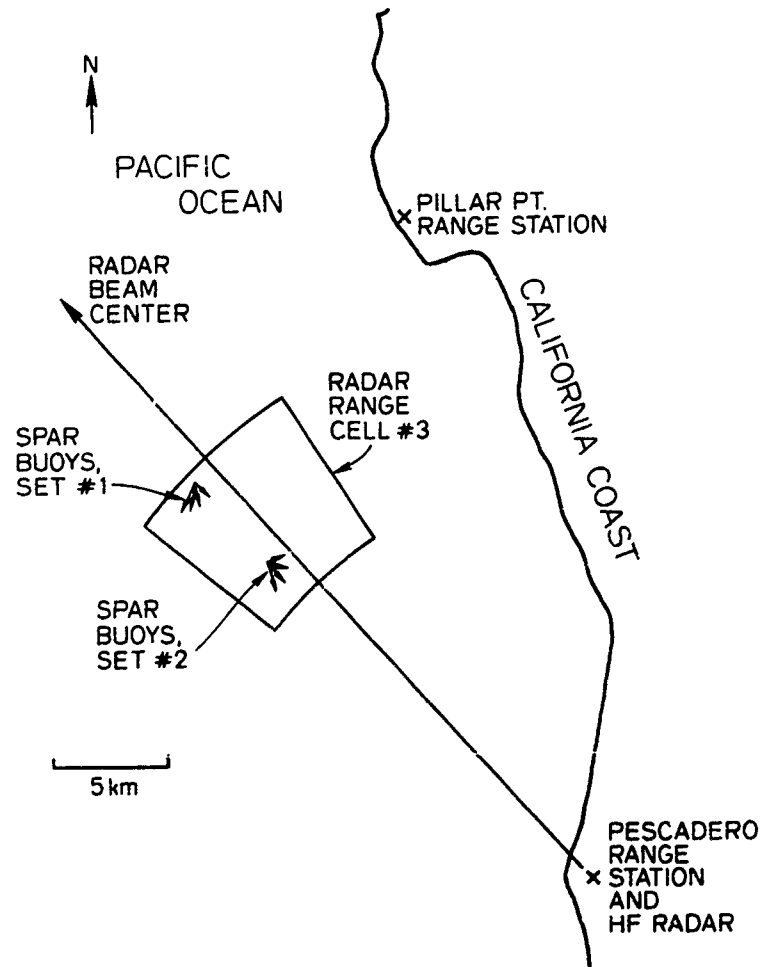


Fig. 5.8. LOCATIONS OF SPAR BUOYS AND RANGE STATIONS.

The buoys were not completely immersed in water so that they would be visible to the human eye. The length ℓ_a remaining above the sea surface is approximately 25 percent of the total length for the shortest buoy and 10 percent for the longest. The effect of wind drag on the drift velocity U_D of the buoys is estimated as follows. The component of wind in the direction of current flow is denoted by U_a , current speed by U_w , air and water densities by ρ_a and ρ_w , respectively, and the immersed buoy length by ℓ_w . At equilibrium, $U_w < U_D < U_a$ and, because the accelerating force from the wind is balanced by the retarding force from the water,

$$\rho_a \ell_a (U_D - U_a)^2 = \rho_w \ell_w (U_D - U_w)^2$$

The ratio ρ_w/ρ_a is 1.2×10^3 . The effect of wind drag is largest at the shortest buoy where $\ell_w/\ell_a = 1/3$. The buoy drift U_{Dr} relative to water current, therefore, is

$$U_{Dr} \approx \left(\frac{10^{-3}}{1.2 \times 3} \right)^{1/2} U_a$$

where U_D is assumed to be small compared to U_a . The maximum wind speed at a 10 m height was approximately 5 m/sec (10 knots) during the January 1978 experiments. At the elevation of the exposed buoy, the wind speed is expected to be lower by a factor of 2. The maximum U_{Dr} is thus ≈ 4 cm/sec which is smaller than the statistical uncertainty in the buoy-inferred drift (see Chapter VII).

It will be demonstrated in Appendix B that, in a current that varies with depth, a buoy immersed to depth ℓ will drift with a speed equal to the current at depth $\alpha\ell$, where $\alpha = 0.5$ and 0.27 for current varying linearly and logarithmically with depth, respectively. With four buoy lengths, current can be probed at four different depths if it has one of the above profiles. There is no general solution to the nonlinear problem of determining the ocean-current profile from the buoy drifts.

To obtain some indication of the variation in ocean current over a radar range cell, two sets of buoys separated by approximately 5 km were deployed within the third range cell (see Fig. 5.8). Because only one

boat was used, the measurements of current at these two points were also separated by the time required by the boat to move from one location to the next and to search for the buoys--typically, 30 to 60 min.

Chapter VI

DETERMINATION OF AVERAGED OCEAN CURRENT FROM DOPPLER SPECTRA

In Chapter V, a procedure was described by which the Doppler spectrum of the sea-returned signal was obtained. An algorithm was developed to determine the spectral points associated with first-order backscatter. These spectral points from the first-order band at either the positive or negative Bragg frequency f_B are used in this chapter to determine the averaged current at the various range cells probed by the HF radar at four frequencies. The results obtained in the previous chapters indicated that the first-order band at the positive Bragg frequency is Bragg-scattered energy from ocean waves moving toward the ocean. When this energy band is of infinitesimal width, its displacement Δ from position f_B has been shown [Eq. (4.6b)] to be

$$\frac{2\pi}{2\beta} \Delta = 4\beta \int_0^{\infty} U_{\beta}(z) \exp(-4\beta z) dz \quad (6.1)$$

where $U_{\beta}(z)$ is the component of current in the direction toward the radar and z is depth below the ocean surface. The quantity on the left-hand side is called the current-induced Doppler velocity $\hat{U}(\beta)$. Introducing the nondimensional variable $\hat{z} = 4\beta z$, Eq. (6.1) can be rewritten as

$$\hat{U}(\beta) = \int_0^{\infty} U_{\beta}\left(\frac{\hat{z}}{4\beta}\right) \exp(-\hat{z}) d\hat{z} \quad (6.2)$$

The measured Doppler velocity, therefore, is a weighted average of the actual current profile, and it varies with the probing radio wave number because the weighting function has a scale length inversely proportional to β .

As has been demonstrated in Chapter V, the observed Bragg line is always of finite width which is assumed to be a manifestation of the turbulent character of the current field; that is, current varies nondeterministically both temporally and spatially within the radar range cell. This assumption is experimentally verified in Chapters VII and VIII.

The centroid of the first-order energy band will be used as an estimate of the position of the Bragg line, and its deviation from f_B is an estimate of Δ . The Doppler velocity $\hat{U}(\beta)$ thus derived will be shown to be the space-time average of the underlying current profile.

A similar argument applies to the first-order band at $-f_B$. A space-time average of the current profile can also be obtained from energy scattered by ocean waves receding from the radar.

A. Estimator of Current-Induced Doppler Velocity

The centroid of the first-order band is applied in this section to estimate the position of the Bragg line. Specifically, if m_U and m_L are the upper and lower cutoff points as determined from the algorithm in Chapter V, the Bragg position is

$$f_0 = \frac{\sum f_m P_m}{\sum P_m} \quad (6.3)$$

where the sums are taken from $m = m_L$ to $m = m_U$, and P_m is the spectral value at the Doppler frequency f_m . The current-induced Doppler velocity $U_c(\beta)$ is obtained through

$$U_c(\beta) = \left[f_0 - (\pm f_B) \right] \frac{\lambda}{2} \quad (6.4)$$

where λ is the radio-wave wavelength $2\pi/\beta$, and the + or - applies to the approaching line (first-order band near f_B) or receding line, respectively.

B. Statistical Analysis of the Doppler-Velocity Estimator

The purpose of this section is to determine whether the estimator is unbiased (its expected value is the mean current) or consistent (its variance about the mean value diminishes as the coherent integration time T increases). Only the approaching line is analyzed because analysis of the receding line is similar. Combining Eqs. (6.3) and (6.4),

$$U_c = \frac{\lambda}{2} \frac{\sum (f_m - f_B) P_m}{\sum P_m}$$

or, equivalently,

$$U_c = \frac{\lambda}{2} \frac{\sum f_m \hat{P}_m}{\sum \hat{P}_m}$$

where \hat{P}_m is the power spectrum of P_m shifted down in frequency by the amount f_B . Extension of the Parseval theorem (see Appendix C for the proof) yields

$$U_c = \frac{\lambda}{4\pi} \frac{\langle \hat{s}(t) i \frac{\partial \hat{s}^*(t)}{\partial t} \rangle}{\langle \hat{s}(t) \hat{s}^*(t) \rangle} \quad (6.5)$$

where the * denotes the complex conjugate and the angular brackets represent a time average over the coherent integration time T . Here, $\hat{s}(t)$ is the Bragg signal near positive f_B multiplied by $\exp(-i2\pi f_B t)$. From Eq. (5.2), therefore,

$$\hat{s}(t) = B_+ \exp(i2\pi\Delta t)$$

where Δ is the current-induced Doppler frequency and B_+ is the amplitude of the Bragg-selected wave component traveling toward the radar. As has been observed, Δ is related to the actual depth-averaged current component $\hat{U}(\beta)$ through

$$\Delta = \frac{2\hat{U}}{\lambda}$$

so that

$$\hat{s}(t) = B \exp[i4\pi(\hat{U}/\lambda) t] \quad (6.6)$$

The subscript of B has been dropped for simplicity.

Equation (6.6) can be extended to the condition wherein \hat{U} varies within the range cell probed by the radar by separating the cell into various domains within each of which \hat{U} is approximately constant. The

linear dimension of each domain must be large compared to the Bragg-selected wavelength L for the following reasons.

- The wave-number selectivity of each domain must remain sharp; otherwise, the Doppler spectrum will be highly smeared--a result contradicted by observation.
- If the size of each domain is smaller or comparable to L , the horizontal shear of the current cannot be neglected in the hydrodynamics and dispersion relationship derived in Chapter II is not valid.

The signal $\hat{S}(t)$ contains contributions from all the domains,

$$\hat{S}(t) = \sum_{\ell} a_{\ell} B_{\ell} \exp(i2\beta \hat{U}_{\ell} t) \quad (6.7)$$

where the dependence of each domain on area a_{ℓ} is explicit. Substituting this model of $\hat{S}(t)$ into the expression for the centroid estimator in Eq. (6.5) yields

$$U_c = \frac{\left\langle \sum_{\ell} \sum_{k} a_{\ell} A_{\ell} a_k A_k^* \hat{U}_k \right\rangle}{\left\langle \sum_{\ell} \sum_{k} a_{\ell} a_k A_{\ell} A_k^* \right\rangle} \quad (6.8)$$

Here, A_k replaces $B_k \exp(i2\beta \hat{U}_k t)$. Because the currents in the different domains will impart a large differential phase to the product term $A_{\ell} A_k^*$, the time-averaged result is negligible for $\ell \neq k$; therefore,

$$U_c \approx \frac{1/T \int dt \sum_k a_k^2 P_k \hat{U}_k}{1/T \int dt \sum_k a_k^2 P_k} \quad (6.9)$$

where $P_k = |A_k|^2$.

A straightforward interpretation of the current estimate is now the weighted average of the depth-averaged current field over the range cell and over the coherent integration time T . To make this interpretation more explicit,

$$U_c = \frac{1}{T} \int dt \sum_k w_k \hat{U}_k \quad (6.10)$$

where

$$w_m = \frac{a_{m m}^2 P_m}{1/T \int dt \sum_k a_k^2 P_k}$$

In a practical context, the answer to the question of an unbiased estimator depends on the desired measurement of the current field; it is apparent that this measurement should correspond to the current averaged over the range cell and over T . If the mean wave-height spectrum is not uniform over the cell, the above weighted average will differ from the desired average as the result of preferential weighting in areas of large mean-squared height. If the spatial variation of P_m is random (uncorrelated with the temporal variation of P_m) then, over a long observation period, U_c will tend toward the desired quantity.

Reduction in the random variation of U_c from one measurement to another as a result of the centroid estimator will now be demonstrated. For this purpose, spatial averaging can be ignored which will greatly simplify the following derivations; therefore,

$$U_c = \frac{1}{T} \int_{-T/2}^{T/2} dt w(t) \hat{U}(t) \quad (6.11)$$

where

$$w(t) = \frac{P(t)}{1/T \int P(t) dt}$$

Assume that the random process $\hat{U}(t)$ is statistically independent of the normalized spectral process $w(t)$. Now, $w(t)$ is a quotient of two random variables; the denominator is a time-averaged version of the numerator. Assuming that w is a stationary process, then, based on the following definitions

$$E[P(t)] \stackrel{\Delta}{=} P_0$$

$$\text{Var}[P(t)] \triangleq \sigma_p^2$$

$$E\{[P(t) - P_0][P(t + \tau) - P_0]\} \triangleq R_p(\tau)$$

and, after some standard manipulations,

$$E\left[\frac{1}{T} \int P(t) dt\right] = P_0 \quad (6.12a)$$

$$\text{Var}\left[\frac{1}{T} \int P(t) dt\right] = \frac{2}{T} \int_0^T R_p(\tau) \left(1 - \frac{\tau}{T}\right) d\tau \quad (6.12b)$$

If P has a correlation time t_p small compared to T , then

$$\text{Var}\left[\frac{1}{T} \int P(t) dt\right] = 2\sigma_p^2 \frac{t_p}{T} \quad (6.13)$$

Because the power spectrum of the gaussian process (with a rectangular window) is a chi-square of two degrees of freedom, its variance-to-squared-mean ratio is unity. The variance of the denominator of $w(t)$, therefore, is small compared to P_0^2 and, following Barrick [1978b],

$$w(t) = \frac{P(t)}{P_0(1+D)} \approx \frac{P(t)}{P_0} (1-D) \quad (6.14)$$

where

$$D = \frac{1}{P_0} \left[\frac{1}{T} \int P(t) dt - P_0 \right]$$

After some lengthy but straightforward manipulations, an expression for the variance of U_c is

$$\text{var}[U_c] = \frac{2}{T} \int_0^T \left(1 - \frac{t}{T}\right) R_U(t) \left[1 + \frac{R_p(t)}{P_0^2}\right] dt \quad (6.15)$$

where $R_U(t)$ is the autocovariance function at lag t of the random process \hat{U} . If the correlation times T_U, T_P for the processes \hat{U} and P , respectively, are small compared to T , then

$$\text{Var}[U_c] \approx 2 \left(\frac{t_U}{T} \right) \sigma_U^2$$

when $t_U > t_P$. If $t_U \ll t_P$, the variance of U_c is approximately doubled.

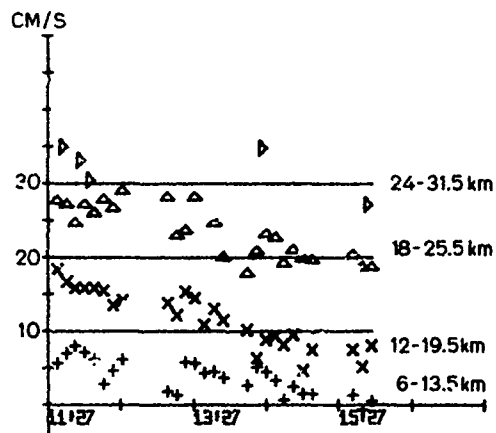
The above calculations demonstrate the variance reduction by the centroid estimator. It has been assumed that the Bragg width is caused by the statistical character of the current field and wave-height spectral amplitude.

C. Experimental Results and Interpretations

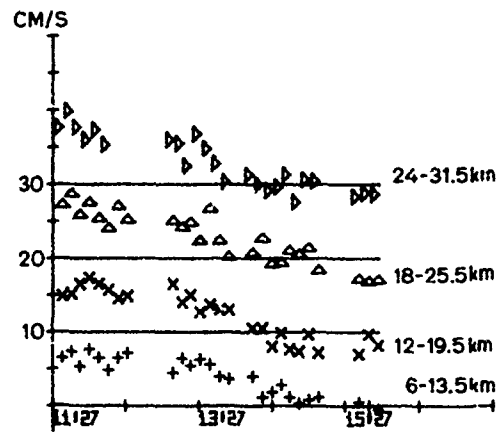
It has been demonstrated that the centroid estimator in Eq. (6.3) can be used to produce estimates $\hat{U}(\beta)$ of the depth-averaged current in the direction of the radar. Each $\hat{U}(\beta)$ is actually an average of the current component over the coherent integration time T and over the entire range cell probed by the radar.

In Figs. 6.1 through 6.4, \hat{U} is plotted vs time. The data were collected during four days in January 1978, and the estimates of \hat{U} were obtained using the approaching Bragg lines because the receding lines during those days had much less signal strength. Data points derived from Bragg lines with a signal-to-noise ratio lower than 6 dB are not plotted. The symbols +, x, Δ, and ▷ denote data obtained from the four range cells centered at 9.75, 15.75, 21.75, and 27.75 km, respectively. Note that the baselines ($\hat{U} = 0$) for data from these range cells are all different; each has been displaced upward by 10 cm/sec for each increment in range, as indicated by the solid horizontal lines.

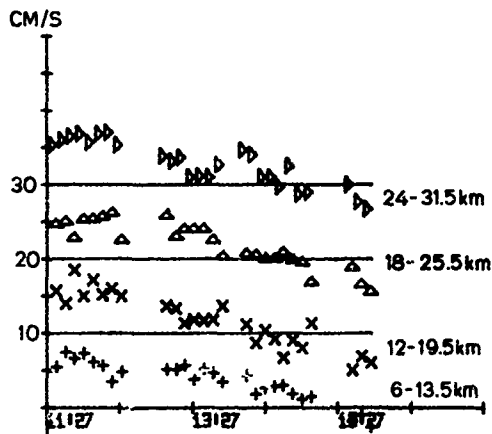
On January 19, the estimated averaged current \hat{U} was observed to decrease consistently with time at all four range cells and radar frequencies during the four hours of the experiment. Current magnitude dropped from 5 cm/sec at 11:27 local time to zero cm/sec at 15:27; superimposed on this trend was a small statistical variation of 1 to 3 cm/sec.



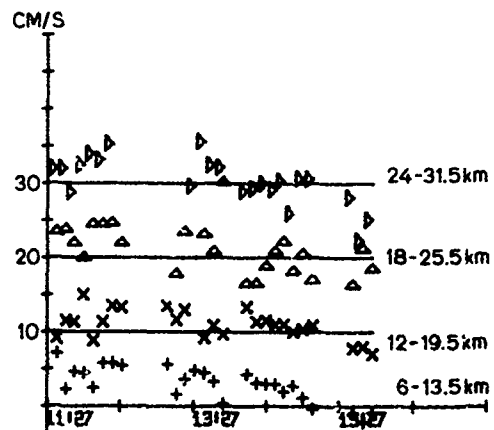
a. 29.75 MHz



b. 21.8 MHz

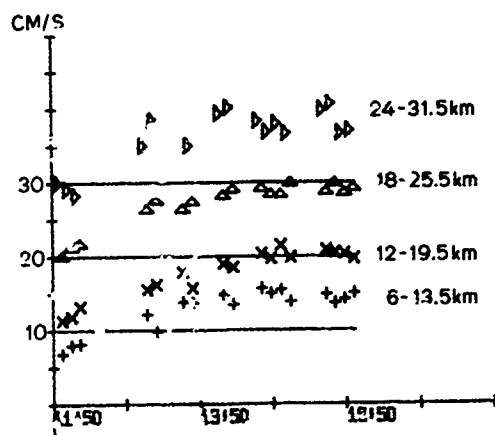


c. 13.4 MHz

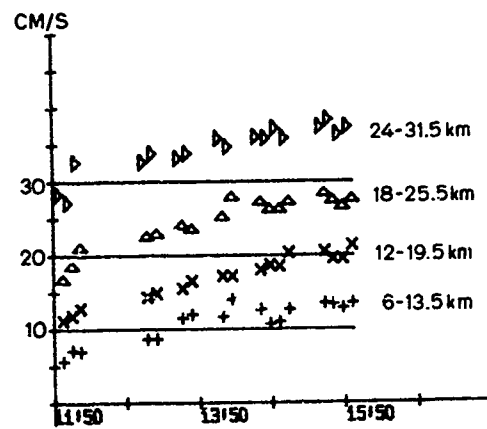


d. 6.8 MHz

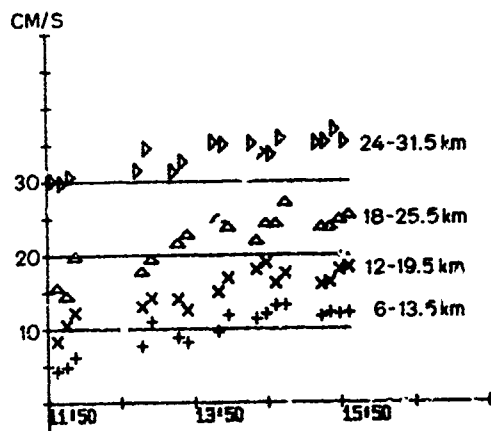
Fig. 6.1. RADAR-INFERRED DEPTH-AVERAGED CURRENT AT FOUR RANGE CELLS VS TIME DURING 19 JANUARY 1978. Horizontal lines are the baselines for the different range cells.



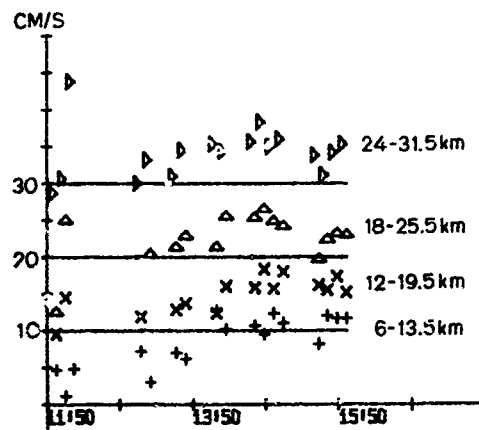
a. 29.75 MHz



b. 21.7 MHz

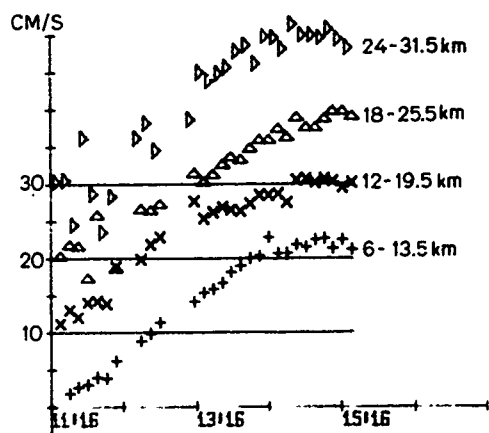


c. 13.3 MHz

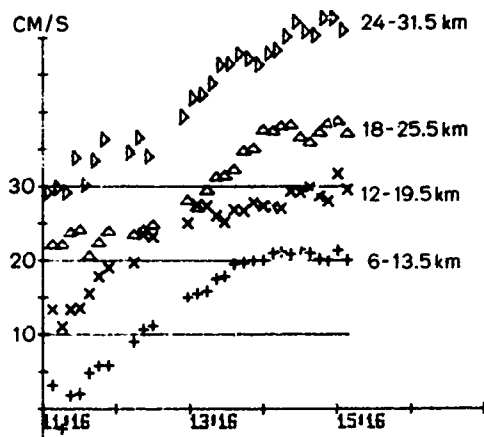


d. 6.8 MHz

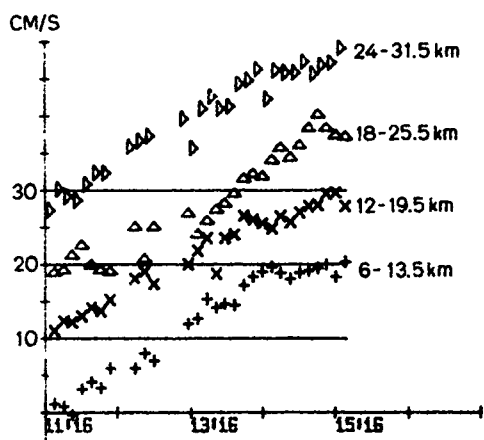
Fig. 6.2. RADAR-INFERRED DEPTH-AVERAGED CURRENT AT FOUR RANGE CELLS VS TIME DURING 20 JANUARY 1978. Horizontal lines are the baselines for the different range cells.



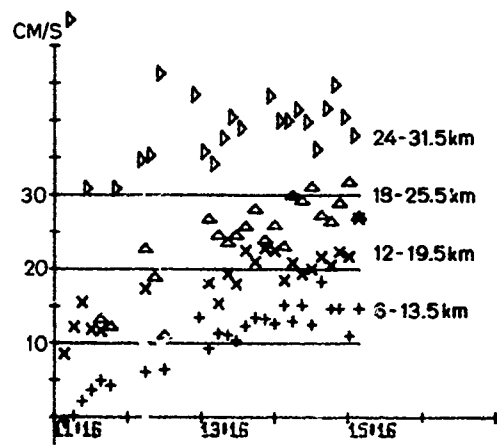
a. 29.75 MHz



b. 21.7 MHz

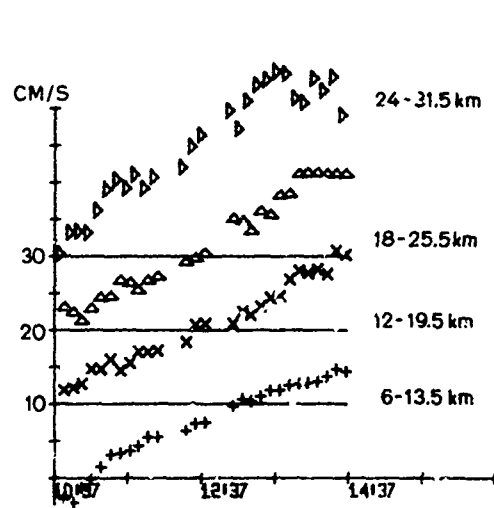


c. 13.3 MHz

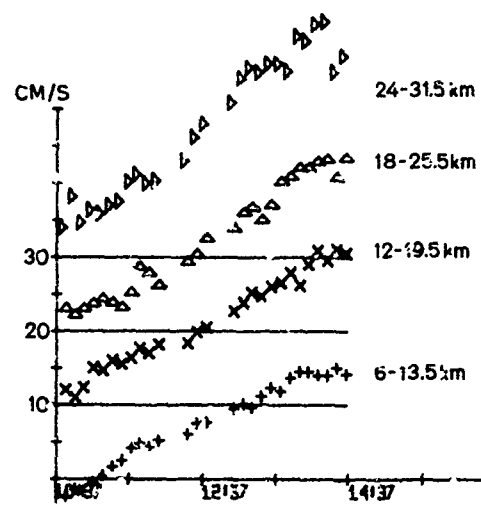


d. 6.8 MHz

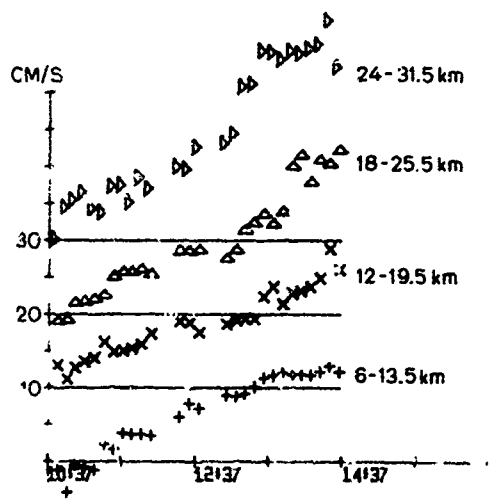
Fig. 6.3. RADAR-INFERRED DEPTH-AVERAGED CURRENT AT FOUR RANGE CELLS VS TIME DURING 24 JANUARY 1978. Horizontal lines are the baselines for the different range cells.



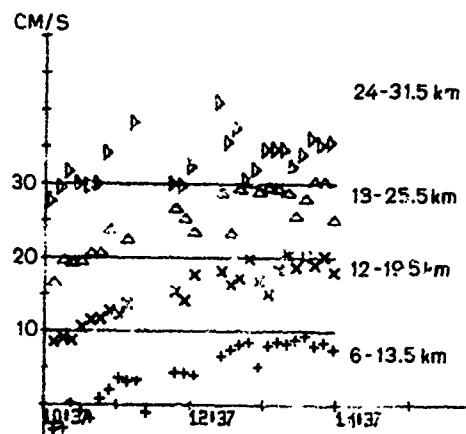
a. 29.75 MHz



b. 21.7 MHz



c. 13.3 MHz



d. 6.8 MHz

Fig. 6.4. RADAR-INFERRED DEPTH-AVERAGED CURRENT AT FOUR RANGE CELLS VS TIME DURING 25 JANUARY 1978. Horizontal lines are the baselines for the different range cells.

The 6.8 MHz data were noisy because the transmitted pulse was reflected from the ionosphere directly overhead and experienced Doppler shifts caused by random ionospheric motions. The resulting Doppler spectrum was relatively broad (a few tenths of a hertz) and, at times, the Bragg lines were submerged in the ionospheric signals. At higher radar frequencies, the ionosphere is transparent to the radio waves.

On January 20, the radar-inferred averaged-current increased steadily with time at all range cells and radar frequencies; the total increase was approximately 5 cm/sec over the four hours of the experiment. Ionospheric interference again contaminated the data at 6.8 MHz. The statistical fluctuation superimposed on the temporal trend was roughly 1 cm/sec.

On January 24 and 25, \hat{U} again consistently increased with time at all range cells and radar frequencies during the first two to three hours and then remained constant to the end of the experiment; the total increase was approximately 20 cm/sec on January 24 and 15 cm/sec on January 25. The increase of current with radar frequency was apparent on those two days. The fluctuation superimposed on the temporal trends in the estimated current was again roughly 1 cm/sec.

The observed temporal trend in the depth-averaged current is attributed to two sources--diurnal and semidiurnal variations in the tidal current component [Sverdrup, 1942] and wind speed. On January 19, the wind was less than 5 m/sec and came from the west; the most probable explanation for the steady decrease in current, therefore, is tidal variation. On January 24, the wind rose from 3 m/sec at 11:20 local time to 6 m/sec at 15:40, and its direction shifted from 030° to 300° T. These measurements were sporadic, but they were sufficient to indicate a rise in the wind component toward the radar. The increasing wind drag on the ocean surface may have been partly the cause of the increase in current observed by the radar. The same trend occurred on January 25; the wind rose from 4 m/sec at 11:00 local time to 6 m/sec at 14:28, and its direction shifted from 230° to 300° T.

To examine the correlation between tidal currents and the radar-measured current, local time can be converted into a phase angle from the nearest tidal peak as recorded in the tide table at Point Fort in San Francisco, assuming a tidal period of 12 hours. For example, the data for January 19 covered phase angles from approximately 100° to 240° and

the data for January 24 covered phase angles from 0° to 125° . It is extremely difficult to relate water movement caused by tides to tidal current [Lisitzin, 1974]; however, the nonoverlapping phase-angle ranges during January 19 and 24 may account for part of the observed reversal in temporal trends in the currents.

Chapter VII

ESTIMATION OF DRIFT PROFILE FROM CURRENT-INDUCED DOPPLER VELOCITIES

As has been discussed in the previous chapters, the estimated current-induced Doppler velocity is a weighted average of the ocean current over depth. To be precise, the radar-inferred Doppler velocity $\hat{U}(\beta)$ at radio-wave wave number β has been shown [Eq. (6.1)] to be

$$\hat{U}(\beta) = 4\beta \int_0^{\infty} U_{\beta}(z) \exp(-4\beta z) dz \quad (7.1)$$

where $U_{\beta}(z)$ is the component of the horizontal ocean current in the direction down the radar beam at depth z . In this chapter, the depth variation of this component will be deduced from $\hat{U}(\beta)$ measured at four radio-wave wave numbers (β).

Theoretical considerations and experimental observations [Bye, 1965; Shemdin, 1972; Wu, 1975] have indicated that the drift profile induced by wind drag is logarithmic,

$$U_{\beta}(z) = U_s - \frac{U_*}{K} \ln \left(\frac{z}{z_0} \right) \quad (7.2)$$

where

U_s = surface drift

U_* = friction velocity

K = universal Von Karman's constant

z_0 = roughness length

This expression is not valid in the very top layer of the ocean where viscous effects cannot be neglected. The thickness of this layer is on the order of millimeters [Bye, 1965]. The importance of this logarithmic profile in the understanding of air/sea interactions leads to the assumption of its validity in a first attempt to invert the relationship in Eq. (7.1). This assumption also enables determination of the drift profile from in-situ measurements (see Chapter V) so that comparisons to radar-inferred current can be made.

The data obtained from the experiments, however, indicate that such assumptions are not always valid. An algorithm is derived, therefore, for inversion of the Laplace relation in Eq. (7.1).

A. Comparisons between Radar-Inferred Drift Profile and In-Situ Drift Measurements for Logarithmic Profile

The logarithmic profile in Eq. (7.2) is assumed to be valid except for a very thin surface layer of thickness δ from which the contribution to the integral in Eq. (7.1) is negligible. Introducing a variable $s = 4\beta z$,

$$\hat{U}(\beta) = U_s - \frac{U_*}{K} \left[\ln \left(\frac{1}{4\beta z_o} \right) \exp(-4\beta\delta) - \int_{4\beta\delta}^{\infty} \ln(s) \exp(-s) ds \right]$$

Because δ is much smaller than the radio wavelength, $4\beta\delta$ is approximately zero and the integral (with the minus sign) in the above equation is then a constant; actually, it is equal to the Euler constant $\gamma = 0.5772$ [Carrier et al, p. 186]. If $\gamma = \ln(r)$, then

$$\hat{U}(\beta) = U_s - \frac{U_*}{K} \ln \left(\frac{z_p}{z_o} \right) \quad (7.3)$$

where $z_p = 1/(4\beta r) \approx 0.022 \lambda$, and λ is the radio-wave wavelength. In other words, the radar probes the logarithmic current at a depth of approximately 2 percent of the radio-wave wavelength. If a linear profile had been assumed as it was by Stewart and Joy [1974], the depth probed by the radar would be larger than z_p by a factor of $r = 1.78$.

Based on this result, the current-induced Doppler-velocity estimates \hat{U} at four radar frequencies discussed in Chapter VI can be interpreted as the actual ocean current component U at four different depths. To compare these estimates to the in-situ measurements obtained by drifters, the radar-inferred drifts available at 7-1/2 min intervals are averaged over a time period covered by the available drifter measurements. The results are plotted in Figs. 7.1, 7.2, 7.3, and 7.4 from data collected during January 1978. Note that these plots are derived from positive

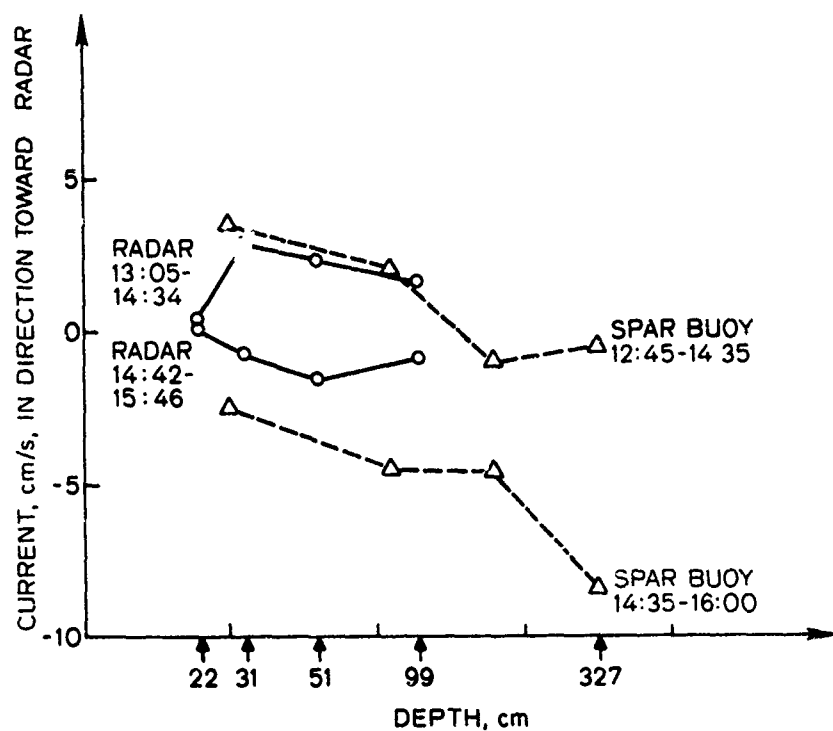


Fig. 7.1. COMPARISON OF RADAR-INFERRED DRIFT AND SPAR-BUOY DRIFT (CLUSTER 2) OBTAINED ON 19 JANUARY 1978. Horizontal axis is logarithmic in depth, and a logarithmic profile is assumed. The approaching Bragg line was used.

Bragg lines (approaching lines) because they were stronger than the receding lines. Superimposed on each figure are the currents inferred from in-situ measurements by drifters at four depths of immersion. By assuming a logarithmic current profile, the measured drifts can again be interpreted as the actual current at four different depths (see Appendix B).

From these plots, the following consistencies between the radar-inferred drifts and the in-situ measurements can be observed.

- The same change of current with time (decreasing the first day and increasing on the other days) is detected in both measurements at the various depths probed.
- The decrease of current with depth, in most cases, is seen in both measurements.
- On January 25, the vertical gradient in the measured current increases with time from both the radar and buoy data. This

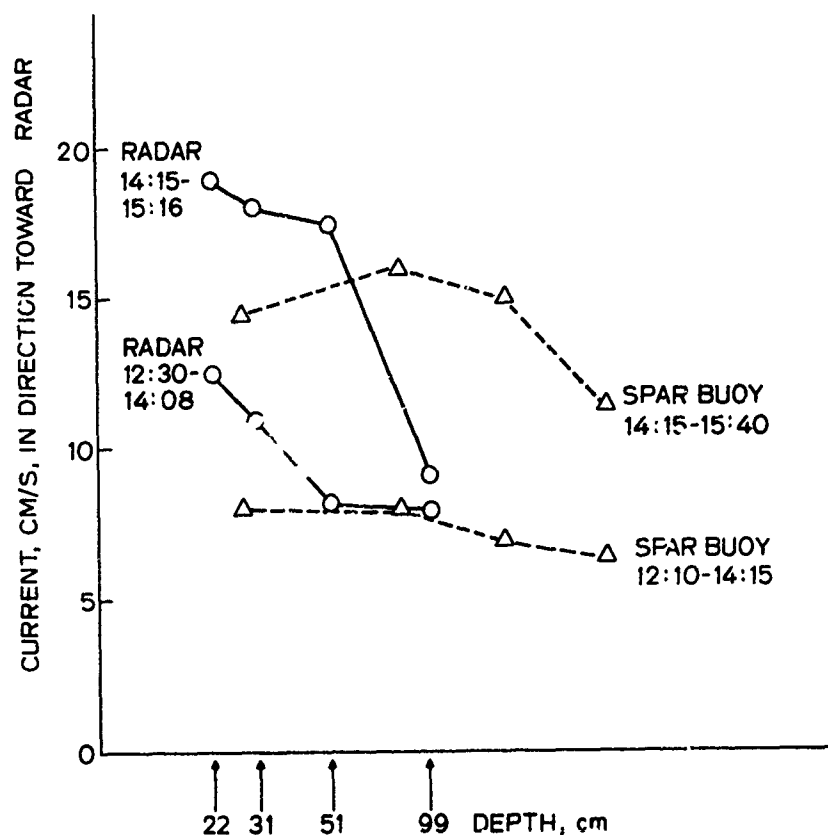


Fig. 7.2. COMPARISON OF RADAR-INFERRED DRIFT AND SPAR-BUOY DRIFT (CLUSTER 1) OBTAINED ON 24 JANUARY 1978. Horizontal axis is logarithmic in depth, and a logarithmic profile is assumed.

can be explained in part by the rise in wind in the direction toward the radar, as described in Chapter VI.

It is also apparent from these plots that the radar-inferred current does not match the in-situ measurements in every detail; for example, the discrepancy between the two types of measurements varies from less than 1 cm/sec to approximately 5 cm/sec. Possible reasons for this discrepancy are explained below.

1. Resolution Limitations

The resolution of the radar measurements is limited by the frequency resolution of the Doppler spectra. As discussed in Chapter V, the

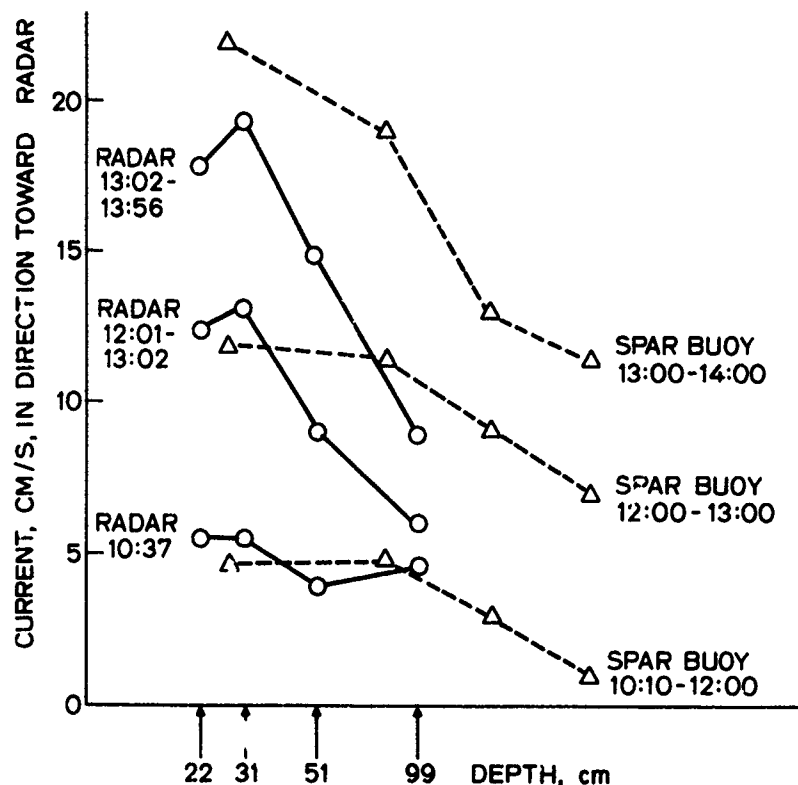


Fig. 7.3. COMPARISON OF RADAR-INFERRED DRIFT AND SPAR-BUOY DRIFT (CLUSTER 1) OBTAINED ON 25 JANUARY 1978. Horizontal axis is logarithmic in depth, and a logarithmic profile is assumed.

nominal frequency resolution is approximately 1 millihertz which results in a current resolution of 2.4, 1.2, 0.8, and 0.6 cm/sec for radar frequencies at 6.8, 13.3, 21.7, and 29.8 MHz, respectively. This inability to resolve smaller current may account for some of the differences observed in the two types of measurements.

The resolution of the drifter measurements is determined by the accuracy of the range measurements which are a few meters. Because, over an interval of an hour, this range uncertainty results in a velocity uncertainty very much less than 1 cm/sec, it is not the limiting factor in the overall accuracy of the drifter measurements.

2. Statistical Uncertainties

Because of the temporal and spatial averaging inherent in the radar-inferred current estimator, the resulting estimator is highly

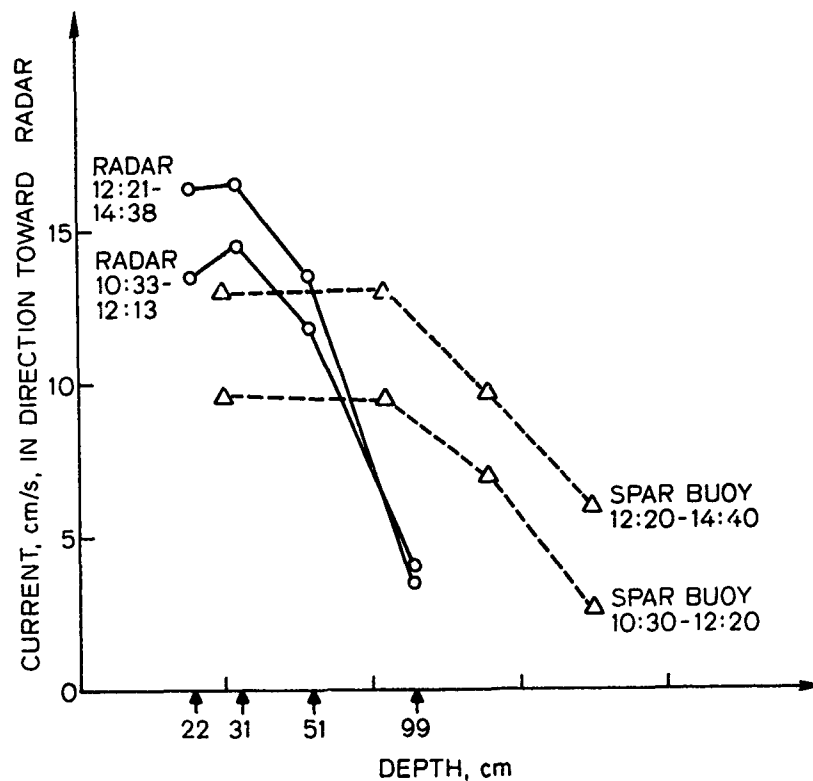


Fig. 7.4. COMPARISON OF RADAR-INFERRED DRIFT AND SPAR-BUOY DRIFT (CLUSTER 1) OBTAINED ON 27 JANUARY 1978. Horizontal axis is logarithmic in depth, and a logarithmic profile is assumed.

consistent; the residual statistical fluctuation after the temporal trend is removed from the data plotted in Figs. 6.1 through 6.3 is on the order of 1 cm/sec. The drifter, however, senses only the current field along a specific trajectory. In a highly variable current field, drifter measurements can differ significantly from the averaged current measured by the radar. An indication of current-field variability is the finite width of the Bragg lines in the Doppler spectra. In-situ evidence of this variability is apparent in the discrepancy between the motions of buoys deployed 6 km apart in the experiments. The current profile measured by the two sets of spar buoys is plotted in Fig. 7.5. It can be seen that the current magnitude at the nearer end of the range cell is smaller than that at the farther end by at least 5 cm/sec. Larger variability in drifter measurements and a greater discrepancy between radar-inferred and buoy-inferred currents have been reported [Barrick et al, 1977b].

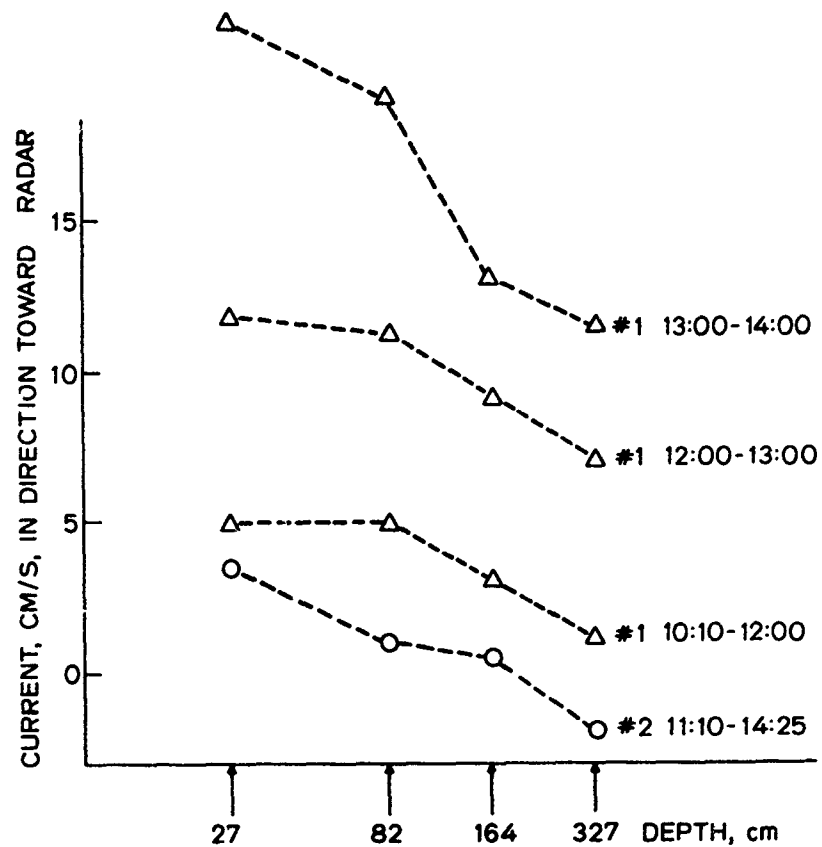


Fig. 7.5. VARIANCE IN DRIFTS OF SPAR BUOYS RELEASED IN THE SAME RANGE CELL. Cluster 1 was released at 25.8 km from Pescadero, and cluster 2 was released at 20.5 km. Data were collected on 25 January 1978.

This current-field variability in the horizontal plane can generate errors in estimating the vertical gradient (or shear) of the current from the in-situ measurements. Assume that a wind-shear flow produces a current shear that is uniform over the range cell. Buoys of varying lengths released at the same location will drift simultaneously with different velocities because of the current shear. As they drift apart, they will be influenced by current at different locations and times. Variations in the drift of the buoys are then the result of current variability in the horizontal plane and vertical current shear. This may explain why the shear observed in the radar data differs from that in the drifter data.

B. Estimate of Friction Velocity U_*

It is evident from Eq. (7.2) that friction velocity U_* can be estimated from the slope of the curve U_β vs $\ln(z)$. The radar data obtained from the closest range cell on 24 January 1978 are used here as an illustration because, as can be seen in Fig. 7.6, they are especially consistent with the assumption of the logarithmic profile [Eq. (7.2)]. The slope of the visual fit yields $U_* = 1.6$ cm/sec based on the value of 0.4 for the von Karman constant K .

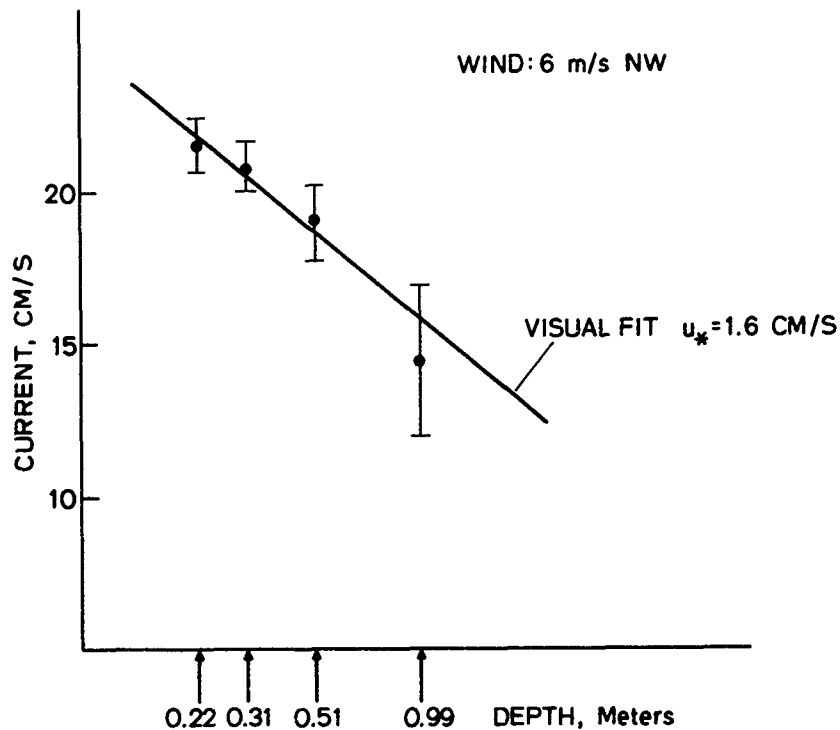


Fig. 7.6. LOGARITHMIC CURRENT SHEAR MEASURED BY THE FOUR-FREQUENCY RADAR. Horizontal axis is logarithmic in depth, and the logarithmic profile is assumed in the inversion. Vertical bar indicates resolution limited by a finite-time Fourier transform. Data obtained at Pescadero at approximately 14:15 to 15:15 LT on 24 January 1978; range 6 to 13.5 km.

During this particular experiment, the wind speed V down the radar beam was approximately 6 m/sec which resulted in a wind stress of $(1/2) \rho_a V^2$, where ρ_a is the air density ($\approx 1.2 \times 10^{-3}$ gm/cc). The drag coefficient C_D defined by

$$\rho_W U_*^2 = C_D \rho_a V^2 \quad (7.4)$$

has been found experimentally to be approximately 1.3×10^{-3} [Stewart, private communication], where ρ_W is water density and V is wind speed at an anemometer height of 10 m. The anemometer was located on the top of the mast of the boat used to deploy and track the buoys. Its height was comparable to that required for the empirical formula [Eq. (7.4)]. If $V = 6$ m/sec, friction velocity is $U_* \approx 0.8$ cm/sec which is one-half that measured by the radar. This difference may be caused by the uncertainties in the wind measurements and in the determination of the drag coefficient.

C. Drift-Profile Estimation from Numerical Inversion

Inverting the integral relation in Eq. (7.1) without assuming any specific functional form of current vs depth distribution is complicated by two factors. First, the value of the current-induced Doppler velocity $\hat{U}(\beta)$ is known only at four values of the argument β and, second, these known values are inevitably contaminated with measurement noise. The first factor constrains the number of quadrature points to four that can be used to approximate the integral by a finite sum. To minimize the truncation error resulting from this quadrature approximation, the gaussian quadrature method [Lanczos, Chapter VI; Bellman et al, Chapter II] is employed. Both truncation error and measurement noise will be severely amplified in the inversion, and this always occurs when inverting the Fredholm integral equation of the first kind, of which the Laplace relation here is an example [Phillips, 1962]. This problem is solved by a stabilized inversion technique.

1. Reduction to Gaussian Quadratures

An integral can be approximated by summing over a finite number of terms; that is,

$$\int_{-1}^1 f(x) dx \approx \sum_{i=1}^n f(x_i) w_i \quad (7.5)$$

where x_i are the quadrature points and w_i are the weights. In the method introduced by Gauss, both x_i and w_i are chosen by requiring that Eq. (7.5) must be exact for any polynomial of order $\leq 2n-1$.

An explicit formula for w_i is first obtained by fitting a polynomial $p_{n-1}(x)$ of order $n-1$ to the "data" $f(x)$ at all n quadrature points. This can be accomplished by forming polynomials $Q_i(x)$ ($i = 1, 2, \dots, n$), each of order $n-1$ and having the property that it is zero at all quadrature points except x_i ; that is,

$$Q_i(x_j) = \delta_{ij} \quad (7.6)$$

where δ_{ij} is the Kronecker delta. Then,

$$p_{n-1}(x) = \sum_{i=1}^n f(x_i) Q_i(x) \quad (7.7)$$

will match $f(x)$ at all quadrature points. The following expression for $Q_i(x)$ will have the desirable sampling property of Eq. (7.6):

$$Q_i(x) = \frac{q_i(x)}{q_i(x_i)} \quad (7.8a)$$

where $q_i(x) = (x-x_1)(x-x_2)\dots(x-x_{i-1})(x-x_{i+1})\dots(x-x_n)$. Note that $q_i(x)$ is a polynomial of order $n-1$ because the term $x-x_i$ is missing from the product chain. If the n^{th} -order polynomial $F_n(x)$ is defined as

$$F_n(x) = (x-x_i) q_i(x)$$

an equivalent expression for $Q_i(x)$ is

$$Q_i(x) = \frac{1}{F'_n(x_i)} \frac{F_n(x)}{x-x_i} \quad (7.8b)$$

which is the Lagrange interpolation formula that yields exact values of $f(x)$ at any point x if $f(x)$ is a polynomial of order $n-1$. Here,

the prime indicates differentiation with respect to x , and $F_n(x)$ has n zeros located at the n quadrature points x_i .

Based on the condition that Eq. (7.5) must be exact for $p_{n-1}(x)$, the following expression for the gaussian weights w_i is obtained:

$$w_i = \int_{-1}^1 Q_i(x) dx \quad i = 1, 2, \dots, n \quad (7.9)$$

This equation depends on the exact form of $Q_i(x)$ which, in turn, depends on the specification of the quadrature points x_i . The precise values of these n points can now be optimally chosen by requiring that Eq. (7.5) is exact for all polynomials of order $2n-1$. Equivalently, $Q_i(x)$ should be such that

$$w_i = \int_{-1}^1 Q_i(x) dx = 0 \quad i = n+1, \dots, 2n$$

which will result in an n -point quadrature formula whose accuracy equals that of a $2n$ -point quadrature formula. This condition is analogous to requiring [Bellman, 1966, Chapter II] that

$$\int_{-1}^1 x^i F_n(x) dx = 0 \quad i = 0, 1, \dots, n-1$$

and this orthogonality condition is satisfied by the Legendre polynomial of order n . The n quadrature points are thus identified as the n zeros of the n^{th} -order Legendre polynomial. With x_i defined, $Q_i(x)$ can be computed and used to determine w_i . The results for both x_i and w_i are, in fact, well tabulated [see, for example, Abramowitz et al, p. 916].

To reduce the integral in Eq. (7.1) to quadratures, the transformation $x = 2 \exp(-4k_0 z) - 1$ is first introduced to map the interval $[0, \infty]$ into $[-1, 1]$. Here, k_0 is an arbitrary wave number chosen to minimize the quadrature error. The transformed integral can then be reduced to quadratures as described above. The resulting matrix equation is

$$\underline{f} = \underline{Ac} \quad (7.10a)$$

where

\underline{f} is the vector with components

$$f_i = \frac{2\hat{U}(s_i k_0)}{s_i} \quad i = 1, 2, 3, 4 \quad (7.10b)$$

\underline{c} is the vector with components

$$c_j = U_\beta [z(x_j)] w_j \quad j = 1, 2, 3, 4 \quad (7.10c)$$

A is the matrix with elements

$$a_{ij} = \left(\frac{1}{2} + \frac{1}{2} x_j \right) s_i^{-1} \quad (7.10d)$$

s_i is the normalized wave number β_i/k_0

$z(x_j)$ is the depth defined as

$$z(x_j) = - \frac{\ln \left(\frac{1}{2} + \frac{1}{2} x_j \right)}{4k_0} \quad (7.10e)$$

The quadrature points x_j and weights w_j are as follows:

\underline{i}	\underline{x}_i	\underline{w}_i
1	0.8611363116	0.3478548451
2	0.3399810436	0.6521451548
3	$-x_2$	w_2
4	$-x_1$	w_1

Because k_0 is chosen as the smallest of the four wave numbers used in the experiments, every matrix element a_{ij} is bounded. In all the experiments discussed in this chapter, $k_0 = 0.568 \text{ m}^{-1}$ which corresponds to the radar frequency of 6.78 MHz. From Eq. (7.10e), therefore, the

depths corresponding to the gaussian quadrature points x_j are 0.127, 0.705, 1.952, and 4.696 m.

The numerical integration indicated in Eq. (7.10a) was programmed on a 32-bit computer for a few selected drift profiles, and the results are listed in Table 7.1. It can be seen that the quadrature errors are no more than 3 percent except when the rapidly varying linear drift profile was detected to a relatively great depth at the lowest radar frequency.

Table 7.1

COMPARISON OF NUMERICAL-INTEGRATION RESULTS OBTAINED BY GAUSSIAN QUADRATURE AND EXACT CALCULATIONS

β (m^{-1})	$\hat{U}(\beta)$ by Quadrature	Exact $\hat{U}(\beta)$	Percent Error
Uniform Current $U_{\beta}(z) = 20$ cm/sec			
0.568	20.00	20.00	0
1.118	20.00	20.00	0
1.824	20.00	20.00	0
2.492	20.00	20.00	0
Linear Profile $U_{\beta}(z) = 20 * (1 - z)$ cm/sec			
0.568	-14.10	-15.21	7
1.118	2.05	2.10	3
1.824	9.04	9.03	0
2.492	11.98	11.98	0
Exponential Profile $U_{\beta}(z) = 20 * \exp(-z)$ cm/sec			
0.568	7.24	7.24	0
1.118	10.56	10.56	0
1.824	12.92	12.92	0
2.492	14.27	14.27	0
Logarithmic Profile $U_{\beta}(z) = 20 + 2.5 * \ln(10z)$ cm/sec			
0.568	14.21	14.27	0
1.118	15.81	15.96	1
1.824	16.92	17.19	2
2.492	17.60	17.97	2

2. Direct Inversion and the Instability Problem

In the absence of truncation errors and measurement noise, the drift profile $U_{\beta}(z)$ can be recovered from the measured Doppler velocities $\hat{U}(\beta)$ at the four radio wave numbers by directly inverting Eq. (7.10a); if the inverse of the matrix A is found to be B , then

$$U_{\beta}\left[z(x_i)\right] = \frac{\sum_{j=1}^4 B_{ij} f_j}{w_i} \quad i = 1, \dots, 4 \quad (7.11)$$

For the matrix inversion, the gaussian elimination method [Dahlquist and Bjorck, 1974] is applied and, to verify the algorithm, the numerical-integration results in Table 7.1 are used as simulated Doppler-velocity data for the inversion. The results of the inversion are exactly the assumed current data used as input to the integration routine, as expected, which indicates that the finite register length of the computer does not introduce significant error.

The measured Doppler velocities can never be free of measurement noise $\underline{\epsilon}$ which may be caused by the statistical fluctuations inherent in the random nature of the ocean superimposed on noise introduced by the radar equipment. The quadrature error will also appear as a noise component. The total $\underline{\epsilon}$ will be transmitted to the inferred profile $U_{\beta}(z)$ through the matrix inversion. For all Fredholm integral equations of the first kind, the matrix A associated with the kernel is unstable because, in $\underline{f} = A\underline{c}$, the solution vector \underline{c} is very sensitive to small perturbations in \underline{f} [Phillips, 1962]. All measurement noise, therefore, will be highly amplified in the inversion process, and the inferred profile will be severely distorted.

To demonstrate the instability problem, error is intentionally introduced into the simulated Doppler velocities in the following manner:

$$f_j = f_j \cdot \left[1 - \text{error} \cdot (-1)^j \right]$$

where the error is 0.01 in the first case and 0.1 in the second. As can be seen in Table 7.2, 1 percent noise introduces error as large as 70 percent in the estimated profile, and 10 percent noise distorts the drift profile beyond recognition.

Table 7.2

EXAMPLES OF INSTABILITY IN DIRECT INVERSION. Logarithmic profile $U_{\beta}(z) = 20 - 2.5 * \ln(10z)$ is assumed.

z (m)	Actual U_{β} (cm/sec)	U_{β} from Direct Inversion		
		Noise Free	1% Noise	10% Noise
0.13	19.41	19.41	15.78	-16.91
0.71	15.12	15.12	21.34	77.36
1.95	12.57	12.57	3.66	-76.50
4.70	10.38	10.38	19.85	105.16

3. Stabilized Inversion

The matrix equation to be inverted in the presence of measurement noise $\underline{\epsilon}$ is

$$\underline{f} = \underline{A}\underline{c} + \underline{\epsilon}$$

whose least-square-error solution is obtained by the inversion

$${}^t A \underline{A} \underline{c} = A {}^t \underline{f}$$

where t indicates that the matrix A is transposed. Because $A {}^t$ is a square matrix that has an inverse, this least-square solution is reduced to solving $\underline{f} = \underline{A}\underline{c}$ --again an unstable procedure.

Further restrictions imposed on \underline{c} are required to produce a stable solution. Phillips [1962] was the first to propose imposing the condition of minimum second difference of \underline{c} in solving the Fredholm integral equation of the first kind. Twomey [1963] simplified this approach and suggested minimizing the mean-squared difference between \underline{c} and a known a priori profile \underline{c}_0 . Bellman et al [1966] devised algorithms for the above constraints but from a dynamic-programming standpoint based on an iterative approach to inverting the matrix equations considered by Phillips and Twomey. In a more recent survey, Westwater et al [1972] described a statistical technique that requires as inputs the covariance matrices of the unknown vector \underline{c} and measurement noise $\underline{\epsilon}$.

In the method employed here, a specific functional form (either logarithmic or linear) is first assumed for the current vs depth distribution, and a first estimate of the current at four depths is obtained. Based on a least-square fit, the current is then extrapolated at the four depths dictated by the numerical quadrature method. This extrapolated profile is then converted to a vector \underline{c}_0 according to Eq. (7.10c), which is then used to stabilize the numerical inversion as described below.

The formula for this stabilized inversion can be derived as follows. A solution \underline{c} is sought wherein the transformed vector \underline{Ac} is as close to the measurement vector \underline{f} as possible and the deviation of \underline{c} from the initial solution \underline{c}_0 is small. This is achieved by minimizing the weighted sum of the mean-squared errors,

$$Q = \sum_i \left(\sum_j A_{ij} c_j - f_i \right)^2 + \lambda \sum_i (c_i - c_{0i})^2$$

Here, the weighting factor λ can be appropriately called a Lagrange multiplier, and Q is a quadrature form whose minimum is attained by differentiating with respect to any component c_k of \underline{c} and setting the result to zero. Therefore,

$$\sum_i \left(\sum_j A_{ij} c_j - f_i \right) \left(\sum_l A_{il} \delta_{lk} \right) + \lambda \sum_l (c_l - c_{0l}) \delta_{lk} = 0$$

where δ_{lk} is the Kronecker delta whose sampling property can be used to remove the summation over l . As a result,

$$\sum_i \sum_j A_{ki}^t A_{ij} c_j + \lambda c_k = \sum_i A_{ki}^t f_i + \lambda c_{0k}$$

In matrix form, the above system of linear equations can be written as

$$(A^t A + \lambda I) \underline{c} = A^t \underline{f} + \lambda \underline{c}_0 \quad (7.12)$$

Through gaussian elimination, \underline{c} can thus be obtained. Note that, when λ vanishes, Eq. (7.12) reduces to that of direct inversion; when λ is exceedingly large, \underline{c} approaches \underline{c}_0 . It is apparent that an intermediate value of λ is required to stabilize the inversion to improve the initial estimate of the solution. To obtain an optimal value of λ , Phillips [1962] proposed a method in which \underline{c} is determined from Eq. (7.12) and the root-mean-squared error $e = (\underline{Ac} - \underline{f})^t (\underline{Ac} - \underline{f})$ is compared to the root-mean-squared noise ϵ in the measurement vector \underline{f} . The value of λ that results in e closest to the noise level ϵ is then the optimal value. Phillips reported, however, that this technique was not always effective.

In the approach taken here, after conversion to a Doppler-velocity unit through Eq. (7.10b), e is never larger than 1 cm/sec in both the simulated and real data; it increases slowly from zero at $\lambda = 0$ to a saturation value of less than 1 cm/sec at λ larger than unity. The transition at $\lambda \approx 0.001$ is fairly sharp. Although the inverted vector solution \underline{c} may have undergone magnitude changes from a few to a few hundred cm/sec as λ drops from very large to very small values, the deduced measurement \underline{Ac} varies little from the actual measurement \underline{f} . The reason for this behavior is the unstable nature of the matrix A . As the inverse of A amplifies measurement noise, the matrix itself attenuates any variations in \underline{c} . From the data presented in Chapter VI and the resolution calculations in Section A, measurement noise here is also on the order of 1 cm/sec. Based on Phillip's method, a value of $\lambda = 0.1$ or larger is required. The need for a value of λ much larger than unity implies that stabilized inversion will not significantly improve the initial estimates obtained by assuming a specific functional form for current distribution vs depth.

To examine in detail the properties of the inversion algorithm, the current-induced Doppler velocity $\hat{U}(\beta)$ is simulated by using a logarithmic or linear current profile $U_\beta(z)$ in Eq. (7.1) for which the induced Doppler velocities at the four radio-wave wave numbers are the actual current at known depths, as discussed in Section A. A fixed-percentage noise can be added to the Doppler-velocity data by alternating the sign of the percentage added to the data at the four wave numbers. To generate \underline{c}_0 , one of the two profiles is assumed and the relationships

in Section A are applied to relate the data to current at four depths. Least-square extrapolation then yields \underline{c}_0 at the quadrature points.

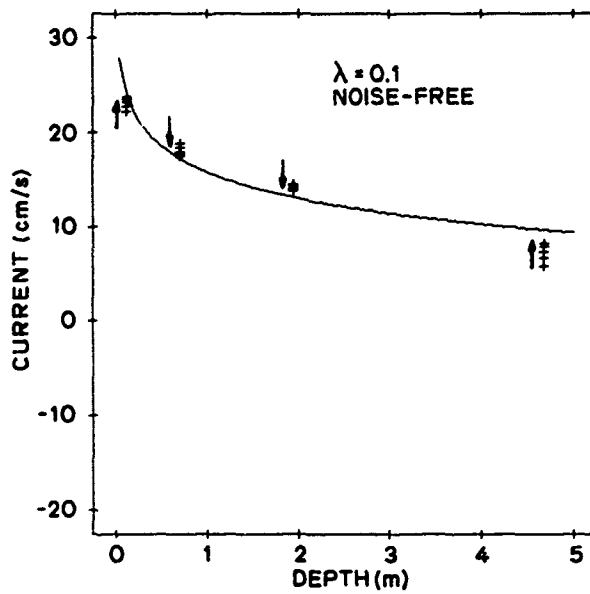
In Fig. 7.7, the inversion algorithm is used iteratively to check convergence when \underline{c}_0 is intentionally chosen incorrectly by assuming the wrong profile. In Fig. 7.7a, the Doppler data contain no noise and the convergence to the actual current profile is fairly rapid. In Fig. 7.7b, 5 percent noise was added to the data, and the iterative approach increased the deviation of the derived profile from the actual profile. It is apparent, therefore, that the best approach is inversion without iteration.

Figure 7.8a serves as a check for the algorithm. Because the data are free of noise and \underline{c}_0 has zero weight, the inversion is essentially perfect; the small difference between the resulting current profile and actual profile is caused by propagation of the quadrature error which must have been even smaller.

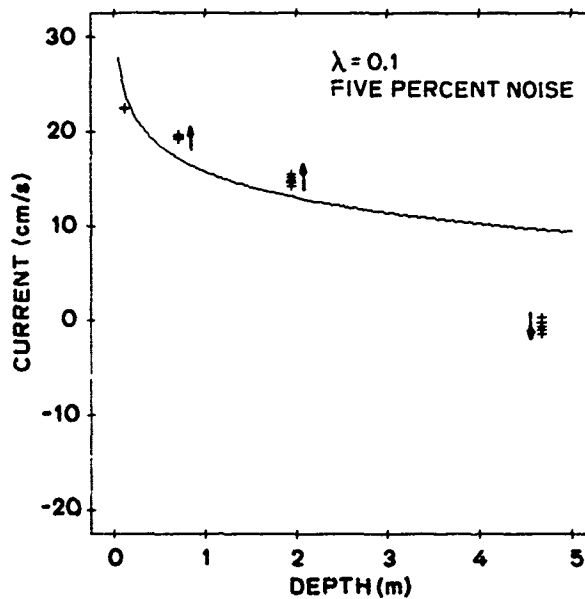
In Fig. 7.8b, 5 percent noise was introduced into the Doppler data. Although \underline{c}_0 has the correct functional form, it is not a replica of the actual current because of the added noise. The inversion output for $\lambda = 0.1$ does not improve the extrapolated profile; in fact, at the last quadrature point (4.7 m), the extrapolated result is significantly closer to the actual profile because it is based on a priori knowledge of the functional form of the current distribution.

Figure 7.9 demonstrates how the correct choice of λ can improve the extrapolation results based on the assumption of a wrong profile. This is encouraging because the purpose of the inversion approach is to eliminate the need for a priori knowledge of the functional form of current distribution vs depth.

In Fig. 7.10, the inversion method is applied to the Doppler-velocity data derived from the radar backscatter signal. In both of these figures, current is again assumed initially to be proportional to logarithmic depth. In the January 20 data, the logarithmic assumption is good, and the inversion result is highly consistent with the extrapolated profile. In the January 24 data, however, there is a sudden departure from the logarithmic trend at the longest wavelength, and the deduced current profile increases slightly with depth after its initial sharp decrease.

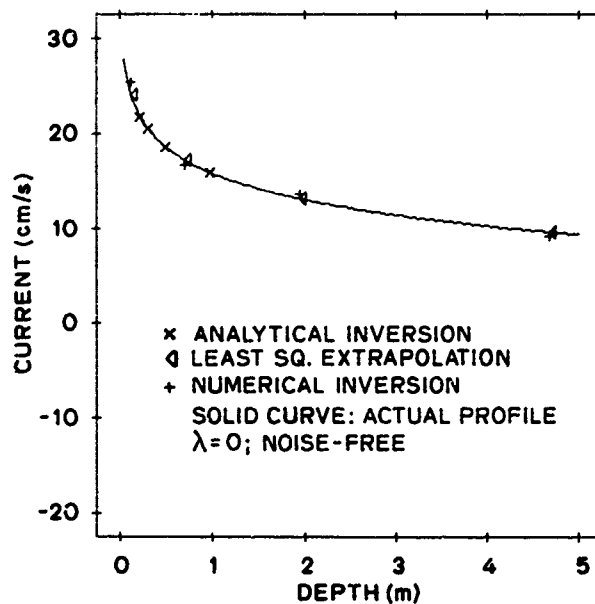


a. Noise-free data

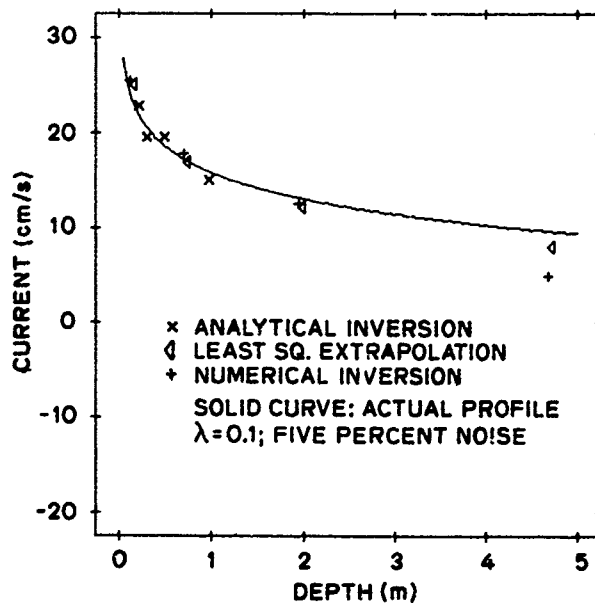


b. Five percent noise added

Fig. 7.7. INVERSION OF SIMULATED DOPPLER DATA, LINEAR PROFILE ASSUMED IN THE INITIAL ESTIMATES. The plus denotes iterative stabilized inversion, and the arrow indicates direction of movement of results as iteration progresses.

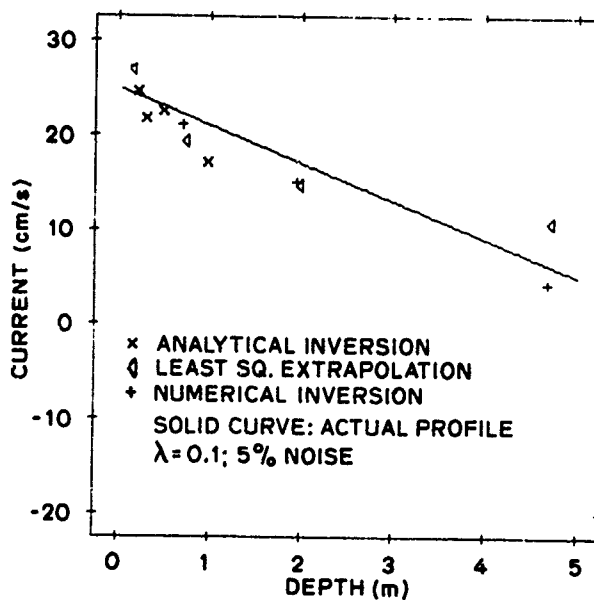


a. Noise-free data

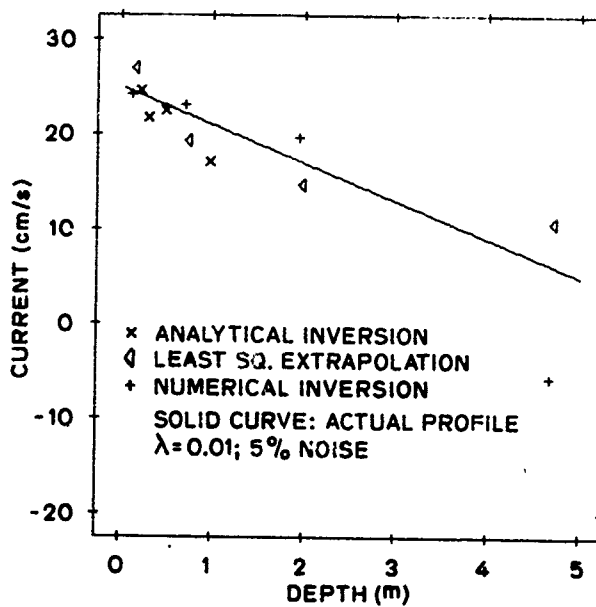


b. Five percent noise added and Lagrange multiplier increased to 0.1

Fig. 7.8. INVERSION OF SIMULATED DOPPLER DATA, LOGARITHMIC PROFILE ASSUMED IN THE INITIAL ESTIMATES.

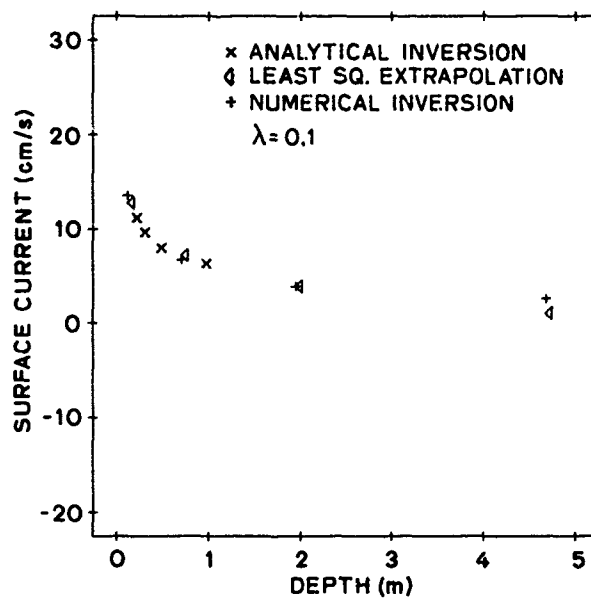


a. Lagrangian multiplier $\lambda = 0.1$

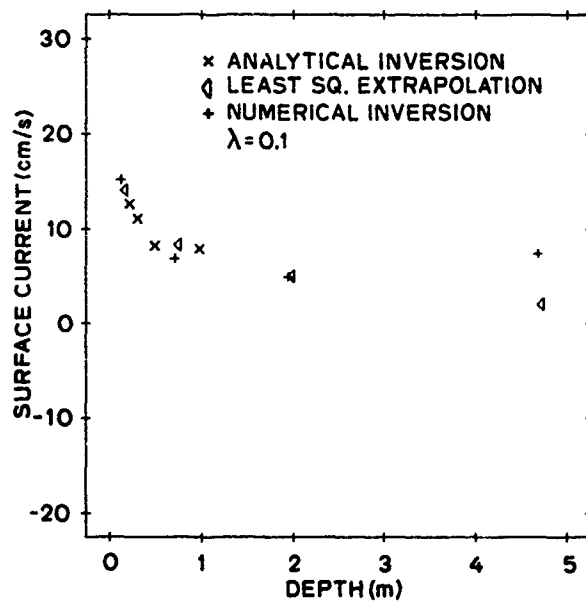


b. Lagrangian multiplier $\lambda = 0.01$

Fig. 7.9. INVERSION OF SIMULATED DOPPLER DATA WITH 5 PERCENT NOISE, LOGARITHMIC PROFILE ASSUMED IN THE INITIAL ESTIMATES.



a. 11:50 to 14:09 LT, 20 January 1978;
6 to 13.5 km range



b. 12:30 to 14:08 LT, 24 January 1978;
18 to 25.5 km range

Fig. 7.10. INVERSION OF RADAR DOPPLER-VELOCITY DATA AVERAGED OVER TIME.

In conclusion, the inversion method appears to work reasonably well given the fact that there are only four data points. If a significantly larger number of data points were to become available (a radar capable of transmitting and receiving sequentially many more than four frequencies), the inversion will be more reliable because the random component in the data can be removed.

Chapter VIII

BANDWIDTH OF THE BRAGG SIGNAL

As has been noted, the bandwidth of the first-order Bragg signal in the radar return typically ranges in units of current from 5 to 15 cm/sec which is significantly larger than the resolution limits of both the temporal transform and spatial filtering that result from the backscattering process. This chapter investigates two practical methods for computing this bandwidth and analyzes its behavior as such radar parameters as pulse width, frequency, and time of sampling and other uncontrolled conditions (such as wind speed) vary. This study will yield valuable insight into the ocean processes that lead to Bragg-line broadening.

A. Bandwidth Estimators

The power spectral density of the Bragg signal is represented by P_i at $f_i = i \cdot \Delta f$, where Δf is the frequency separation between adjacent spectral points. This first-order signal is assumed to be nonzero only in the frequency region determined by $m_1 \leq i \leq m_2$; all summations to be discussed in this chapter will cover only this finite range. A second-moment bandwidth w_1 can then be computed as follows:

$$w_1 = 2 \left(\frac{S}{A} \right)^{1/2} \Delta f \quad (\text{Hz}) \quad (8.1)$$

where

$$S = \sum_i (i - c)^2 P_i = \text{second moment of the spectrum about the centroid}$$

$$c = \sum_i i P_i / A = \text{centroid of the spectrum}$$

$$A = \sum_i P_i = \text{area of power spectral density curve}$$

This estimated width is the frequency separation between the points 2.17 dB down from the peak if the power spectrum is exactly gaussian in shape. The major weakness in this estimate is its sensitivity to noise present at the frequency bins located a long distance away from the signal peak. This is evident in the weighting factor $(i-c)^2$ which increases as the square of the distance from the centroid c .

Area bandwidth w_2 is a much less sensitive estimator,

$$w_2 = \frac{A}{P_{\max}} \cdot \Delta f \quad (\text{Hz}) \quad (8.2)$$

where A is the area of the spectral curve and P_{\max} is the peak value of the power spectrum. This estimate is the exact width of a rectangular spectrum,

$$P_i = \begin{cases} P_{\max} & m_1 \leq i \leq m_2 \\ 0 & \text{otherwise} \end{cases}$$

The principal drawback of this estimator is its sensitivity to the actual spectral shape. For example, when a band of signals has an standing peak, w_2 will be much less than the visual width; when the band is fairly uniform, w_2 will be approximately equal to it.

The relation between w_1 and w_2 can be derived for any given spectrum. For example, in a gaussian curve,

$$\frac{w_2}{w_1} = \left(\frac{\pi}{2}\right)^{1/2} = 1.25$$

and, in a rectangular spectrum,

$$\frac{w_2}{w_1} = 2.45$$

In the gaussian spectrum, the 3 dB width is larger than w_1 by a factor of 1.18 and, as a result, it is well approximated by w_2 .

B. Determination of First-Order Region

The method used here for determining the cutoff points m_1 and m_2 that define the first-order Bragg signal differs from that used in Chapter V. It was chosen for its simplicity and because it yields cutoff points that are less sensitive to spurious signals near the Bragg lines.

The algorithm on which this method is based is as follows.

- Obtain a smoothed version of the Doppler spectrum by convolution with a rectangular window whose width is 10 frequency bins.
- Search for the peak of the smoothed spectrum near the Bragg frequencies $\pm f_B$, assuming a maximum current magnitude of 50 cm/sec.
- Locate the cutoff points 10 dB down on either side of the peak.

As before, these cutoff points are then used to determine the desired parameters from the unsmoothed spectrum. As a check, this algorithm was applied to the data set discussed in Chapter VI to obtain the radar-inferred current, and the resulting current estimates differed by no more than 1 cm/sec from the estimated currents described in Chapter VI. Width estimates, however, are more sensitive to the actual locations of the cutoff points.

C. Results

The set of radar data available for this study is divided into the following two groups:

- data collected from January 1975 through January 1977
- data collected during January 1978

In the first set, the four radar frequencies employed were 4.8, 6.8, 13.3, and 21.7 MHz over approximately 50 days of experiments. During each day, four 1/2 hr experiments were performed, one for each radar pulse width of 25, 50, 100, and 200 μ sec. This large data set is used to study the behavior of the Bragg width as a function of wind speed and direction, radar pulse width, distance (range) of the illuminated ocean patch from the radar, and the radar carrier frequency, respectively.

The second set has the same data base used in Chapters VI and VII. The four carrier frequencies were 6.8, 13.3, 21.7, and 29.7 MHz over five days of experiments (January 19, 20, 24, 25, and 27). Approximately four hours of data were collected each day at a fixed radar pulse width of 50 μ sec. With the exception of January 20, these experiments were

conducted in conjunction with simultaneous in-situ measurements obtained by spar buoys as described in Chapter V.

This second smaller data set is used to determine the frequency dependence of the Bragg width over a slightly different range of frequencies, and the temporal trend observed in the ocean-current estimate (see Chapter VI) is compared to the temporal behavior of the Bragg width deduced from this data set. The in-situ measurements of the total current vector are also employed to compute the Bragg width caused by the finite radar beamwidth, and compatibility between the computed and observed widths is examined.

The estimated width is denoted by $w(a_i, f_j, L_k, r_m)$. The arguments are the variables defined below.

a_i = wind speed classified in four categories

$i=1$ from 0 to 4 knots

$i=2$ from 5 to 9 knots

$i=3$ from 10 to 14 knots

$i=4$ higher than 15 knots

f_j = radar carrier frequencies, increasing with index j

L_k = radar pulse widths, increasing with index k

r_m = range of illuminated ocean patch from the radar, increasing with index m

For convenience, the estimated width w in units of frequency is converted to w_c in units of current via

$$w_c \text{ (cm/sec)} = w \text{ (Hz)} \cdot 15000/f_c \text{ (MHz)}$$

The wind conditions were measured at the Pescadero radar site where an anemometer was located approximately 5 m above ground level, at the S.E. Farallon Island, and at Pigeon Point where they were normally reported at two-hour intervals by the weather bureau (Fig. 8.1). The wind speeds at these three locations were averaged to approximate the prevailing winds in the open sea covered by the radar. Variability in the width estimates was reduced by averaging over those obtained on different days

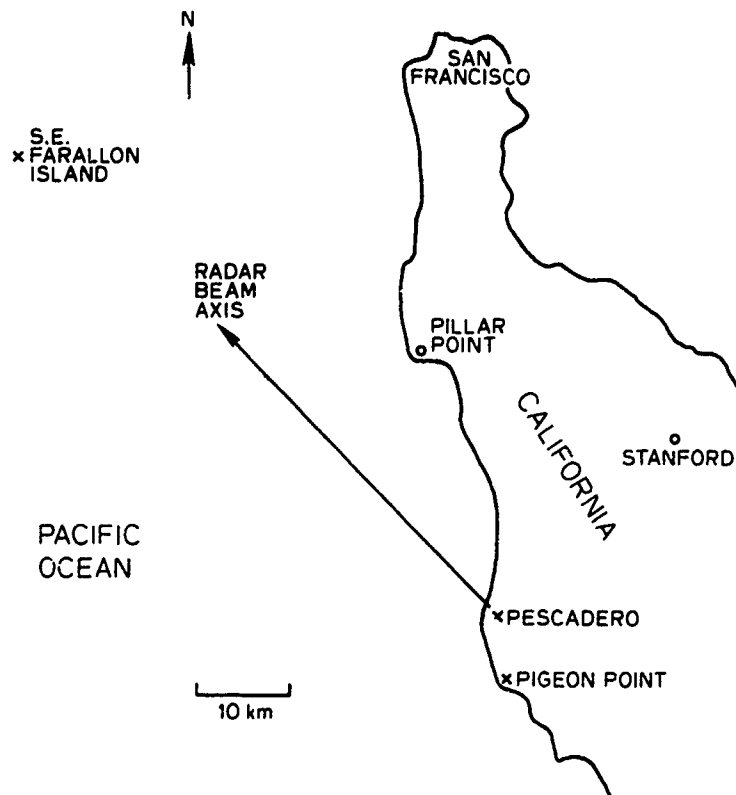


Fig. 8.1. LOCATIONS OF ANEMOMETERS. These are indicated by x at the Farallons, Pescadero, and Pigeon Point.

but under the same classification; the resulting width is denoted by \bar{w}_c . To detect trends in the results, further analysis was based on the assumption that the variation of width $\bar{w}_c(a, f_c, L, r)$ with each of its arguments was separable from its variation with the other arguments in the following manner:

$$\bar{w}_c(a, f, L, r) = \bar{w}_a(a) \bar{w}_f(f_c) \bar{w}_L(L) \bar{w}_r(r) \quad (8.3)$$

Note that the exact functional dependence of \bar{w} on each of the four variables is not specified and, as will be demonstrated, this dependence on most of the variables is very weak.

By normalizing and averaging, assumption (8.3) enables elimination of the dependence of \bar{w}_c on any three of its arguments so that its variation with the remaining argument can be studied. For example, the variation of Bragg width with radar frequency f_j is

$$\hat{w}_c(f_j) = \frac{1}{64} \sum_{i,k,m} \hat{w}_{ikm}(f_j) \quad (8.4)$$

where

$$\hat{w}_{ikm}(f_j) = \frac{\overline{w}_c(a_i, f_j, L_k, r_m)}{\overline{w}_c(a_i, f_1, L_k, r_m)}$$

Normalization is always done with respect to the width at the index value of 1 for the chosen variable. Associated with each of these width estimates is a computed standard deviation s ; for example, the value of s at f_j is

$$s(f_j) = \left\{ \frac{1}{64} \sum_{i,k,m} \left[\hat{w}_{ikm}(f_j) - \hat{w}_c(f_j) \right]^2 \right\}^{1/2} \quad (8.5)$$

In Table 8.1, all the width estimates in the first column are equal to unity because of the specific normalizing constant. The first entry in each cell is the normalized area width derived from Eq. (8.2); the second entry is the second-moment width derived from Eq. (8.1). The bounds of each estimate are established by the standard deviation s . Note that both the area and second-moment widths generally yield similar values. The most outstanding exceptions are observed in the row for the frequency-dependence calculation [third row for $\hat{w}_c(f_1)$]; these discrepancies are presumably caused by the significant fine-scale differences in the Bragg-line structures at the different carrier frequencies.

The standard deviations are large compared to the width variations with wind speed, range-cell size, and range. Conclusions to be drawn concerning such variations are determined from the observed average behavior. The statistical significance of these conclusions may be limited; however, width variation with radar frequency exceeds the associated standard deviation which indicates a conclusive trend.

The behavior of the Bragg width is determined from both data sets, and the results are discussed below.

Table 8.1

NORMALIZED WIDTHS OF BRAGG LINES. These widths are derived from the radar data collected from May 1975 through January 1977. All data with less than a 20 dB signal-to-noise ratio have been rejected. Either the receding or approaching Bragg line was used, depending on which had a higher signal level. The first entry is normalized area width, and the second entry is normalized second-moment width. The bounds are set by the standard deviation in each estimate.

i	1	2	3	4
$\hat{w}_c(a_i)^\dagger$	1.00 1.00	1.03 ± 0.15 1.03 ± 0.18	0.99 ± 0.18 0.98 ± 0.22	1.05 ± 0.22 1.11 ± 0.26
$\hat{w}_c(L_i)^\ddagger$	1.00 1.00	1.08 ± 0.18 1.07 ± 0.17	1.04 ± 0.17 1.05 ± 0.20	1.03 ± 0.22 1.04 ± 0.28
$\hat{w}_c(f_i)^*$	1.00 1.00	0.91 ± 0.16 0.97 ± 0.17	0.59 ± 0.09 0.76 ± 0.14	0.45 ± 0.08 0.62 ± 0.11
$\hat{w}_c(r_i)^\S$	1.00 1.00	1.01 ± 0.18 1.02 ± 0.17	1.07 ± 0.19 1.07 ± 0.18	1.10 ± 0.23 1.13 ± 0.24

$^\dagger a_i$ = wind-speed categories (0 to 4, 5 to 9, 10 to 14, and ≥ 15 knots).

$^\ddagger L_i$ = radial sizes of range cell (3.75, 7.5, 15, and 30 km).

* f_i = radar frequencies (6.8, 13.3, 21.8, and 29.8 MHz).

$^\S r_i$ = ranges from radar ($\approx 10, 15, 20,$ and 25 km).

1. Dependence on Wind Conditions (First Data Set)

Although the last wind-speed category ($i = 4$) was set aside for all velocities higher than 15 knots, difficulty in maneuvering the rhombic antenna at speeds higher than 20 knots set an upper limit on the range of wind conditions observed. The results indicate that the width of the Bragg line increases with wind speed except for an anomalous small decrease in the range from 10 to 14 knots. The total variation is actually only approximately 10 percent from category 1 ($i = 1$) to category 4 ($i = 4$).

The data have also been reclassified according to wind direction, irrespective of its speed. The reference direction is the radar

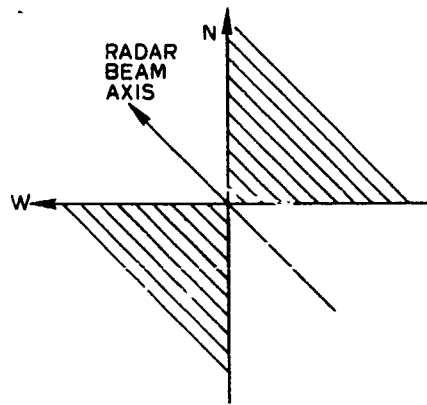


Fig. 8.2. WIND-DIRECTION CLASSIFICATIONS.

beam axis (approximately 315° T). In Fig. 8.2, a cross wind is indicated when the wind-velocity vector lies in the two shaded quadrants, and an up/down wind is indicated when the vector falls in the unshaded quadrants. Analysis of the large data set reveals that the Bragg width for the up/down wind is approximately 2 percent larger than that for the cross wind.

2. Dependence on Radar Pulse Width (First Data Set)

For the radar pulse widths used in the experiments, the corresponding radial sizes of the illuminated ocean patch are 3.75, 7.5, 15, and 30 km. The results in Table 8.1 show that the width of the first-order line increases by 8 percent when the radial extent of the illuminated area increases from 3.75 to 7.5 km; a further increase apparently causes a small reduction in the Bragg width.

3. Dependence on Range from Radar (First Data Set)

The four range cells sampled by the receiver are approximately 10, 15, 20, and 25 km away from the radar. Analyses indicate that the Bragg width increases gradually with range.

4. Dependence on Radar Frequency

a. First Data Set

Both area and second-moment widths decrease sharply with increasing radar frequency although the second-moment estimate indicates a relatively weaker frequency dependence. Note that the width estimates prior to normalization are in units of cm/sec. If the frequency dependence of the Bragg width is approximated by a power law ($w_c \sim f_c^{-\alpha}$), the data in Table 8.1 can be used to estimate α . Based on the tabulated results, $\alpha = 0.5$ for area width and 0.3 for the second-moment width.

b. Second Data Set

The nominal values of the radar carrier frequencies used in these experiments were 6.8, 13.3, 21.7, and 29.75 MHz. After analyzing the data from the first range cell, an approximate power-law dependence ($w_c \sim f_c^{-\alpha}$) was observed with $\alpha \approx 0.4$.

5. Correlation with Radar-Inferred Current (Second Data Set)

Although the radar-inferred current component examined in Chapter VI showed a consistent trend with time during each of the five days of experiments, the Bragg width did not exhibit the same behavior. For example, on January 25, the estimated radial current increased from 0 to 20 cm/sec during the four hours of experiments, and the Bragg width [estimated using Eq. (8.2)] fluctuated about the mean value of 5.7 cm/sec at the radar frequency of 13.3 MHz.

6. Correlation with Width Estimated from In-Situ Current Measurements (Second Data Set)

If the ocean surface current is uniform within the area illuminated by the radar beam, the width of the Bragg line resulting entirely from the finite beamwidth can be estimated. As illustrated in Fig. 8.3, the x axis is directed down the radar boresight toward the radar system and the y axis is transverse to that direction. The uniform current \underline{U}

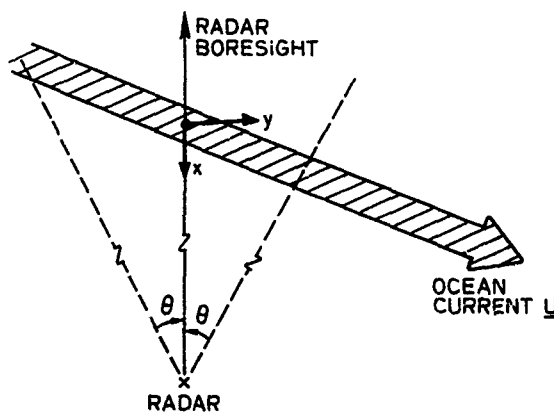


Fig. 8.3. BACKSCATTER GEOMETRY.

has components U_x, U_y . If the 3 dB width of the radar beam is θ , then the 3 dB width of the Bragg line in units of current is

$$\Delta_c = \begin{cases} 2|U_y| \sin \theta & |U_x| \cos \theta + |U_y| \sin \theta > |U_x| \\ |U_x|(1 - \cos \theta) + |U_y| \sin \theta & \text{otherwise} \end{cases} \quad (8.6)$$

Although the in-situ measurements of the ocean current did not support the assumption of uniform current, they are used to calculate Δ_c for completeness. In January 1978, the in-situ measurements indicated that the maximum magnitude of both U_x and U_y was approximately 10 cm/sec which, when combined with the beamwidth information in Fig. 5.1, can be used to estimate the upper bounds of Δ_c at the various radar frequencies. The results are presented in Table 8.2 plus the average width \bar{w}_c of the Bragg line computed by means of the area estimator in Eq. (8.2). If the actual spectral shape is assumed to be gaussian, the 3 dB width will be larger than \bar{w}_c by a factor of 1.06; the small difference introduced by this factor will be ignored. The rapid decrease in Δ_c with radar frequency is the result of the reduction in beamwidth. It can be seen that the beamwidth effect cannot account for the observed width of the Bragg line and that the observed variation with radar frequency is also smaller than predicted.

The in-situ measurements obtained from the two sets of spar buoys deployed at two different locations showed that the ocean current

Table 8.2

COMPARISON OF WIDTH Δ_c ESTIMATED FROM BEAMWIDTH EFFECT (uniform current is assumed) AND WIDTH \bar{w}_c ESTIMATED FROM RADAR DATA (third range cell, 19 January 1978)

Frequency (MHz)	\bar{w}_c (cm/sec)	Δ_c (cm/sec)
6.8	9.3	8.5
13.3	6.2	4.5
21.8	5.6	3.2
29.75	6.4	2.1

in the area illuminated by the radar beam was not uniform (see Fig. 7.5); the turbulent nature of these currents has also been reported by Sverdrup [1942]. Assuming that the ocean current within a given range cell is turbulent and that a standard deviation σ_v is associated with its probability distribution function, the width of the Bragg line is also approximately σ_v . The in-situ measurements did not provide sufficient data from which a statistically significant estimate of σ_v could be extracted; however, the difference in the measurements by the two sets of buoys was of the same order of magnitude as the width of the Bragg line.

D. Summary

This section summarizes the characteristics of the Bragg-line width (in units of cm/sec) as obtained from processing the HF ocean-backscatter radar data consisting of nearly 10,000 Doppler spectra.

- It is inversely proportional to radar carrier frequency f_c ; a power-law fit to the data yielded a frequency dependence of $\approx f_c^{-0.4}$.
- It is a weak function of the prevailing wind speed in the range from 0 to 20 knots. Only up to a 10 percent increase was observed when the wind speed rose at least threefold.
- When wind blows across the radar beam, the Bragg width is approximately 2 percent larger than when wind blows along the beam.
- It increases by 8 percent when the radial extent of the illuminated ocean patch increases from 3.75 to 7.5 km; further increases to 15 and then to 30 km apparently will reduce the Bragg width by a few percent.
- It increases by approximately 10 percent as the center of the range cell sampled by the radar recedes from 10 to 25 km as measured from the radar. This broadening is most likely caused by a reduction in the signal-to-noise ratio with range which results in a higher probability of noise corruption in the width estimator.
- It is uncorrelated with the radial component of the ocean current detected by the radar.

Any attempt to explain the above observed features of the Bragg signal will require a model of the underlying processes that cause the Bragg width. The possibility that broadening is the result of radar system artifacts (such as antenna motion) has been considered in Chapter V; however, experimental evidence indicated that very little broadening could be accounted for in this manner. The effect of a finite beamwidth illuminating a uniform current has also been examined, and experimental evidence revealed that this accounted for part of the observed width and also part of the width reduction with frequency.

In-situ measurements showed that the waters off the San Francisco peninsula have an eddy-current component which is random in nature. If this component does broaden the Bragg line, the following characteristics must be inherent in the eddy-current structure.

- The radial correlation length of the random current field must be much less than 3 km to account for the small change in the Bragg width with the radial extent of the observed ocean patch.
- The dependence of the Bragg width on carrier frequency indicates one or both of the following possibilities.
 - The turbulent current field has a standard deviation that increases with depth. As radar frequency drops, the effective depth probed by the radar increases and the Bragg line broadens.
 - The azimuthal correlation length of the random current field is comparable to the azimuthal size of the illuminated ocean surface. At 15 km, the azimuthal size ranges from 3 to 13 km for the radar frequencies used.
- The weak correlation of the Bragg width with wind speed suggests that the principal mechanism for the generation of current turbulence is not interactions with the prevailing wind.

Further experimental work is required to validate the above observations. Theoretical studies of the effect of small-scale horizontal variations of ocean current on wave phase velocity may also clarify the broadening phenomenon of the Bragg line.

Chapter IX

CONCLUSIONS AND RECOMMENDATIONS

A. Conclusions

The feasibility of remotely sensing ocean surface current and its distribution with depth using a four-frequency HF backscatter radar has been studied theoretically and experimentally. Theoretical investigations indicated that the result obtained by Stewart and Joy [1974] for ocean-wave phase velocity in the presence of surface current with a non-zero vertical gradient is valid if the vertical gradient is small. Their result was extended to second order for an exponential current profile; however, for conditions prevailing during the experiments reported here, this second-order effect was not important. A Bragg-scattering theory based on simple wave-propagation concepts was derived, and it was demonstrated that the current component in the direction of the radar can be estimated from the position of the Bragg signal in the ocean Doppler spectrum.

Data collected by the Stanford four-frequency radar located at Pescadero on the California coast were analyzed to generate an estimate of the ocean current component in the direction of the radar. A 15 min coherent integration time produced resolutions of 2.4, 1.2, 0.8, and 0.6 cm/sec at the radar frequencies of 6.8, 13.3, 21.7, and 29.8 MHz. Experiments during January 1978 revealed that fluctuations in the current estimates were generally no more than 1 to 3 cm/sec superimposed on steady temporal trends.

Spar buoys 1, 3, 6, and 12 m long were deployed and tracked by a microwave system to obtain in-situ measurements of the ocean surface current which were then compared to the radar-inferred current component by assuming that it varies in proportion to logarithmic depth. The discrepancy between the two types of measurements was no larger than the discrepancy between the in-situ measurements made along two different trajectories within the same range cell probed by the radar. The general behavior of the ocean current with time and depth measured by the spar buoys agreed with that measured by the radar.

Reconstruction of the ocean-current distribution with depth from the radar Doppler measurements without assuming an explicit functional form of the current profile requires inversion of a Fredholm integral equation of the first kind. A numerical inversion technique was investigated, using a stabilization scheme based on an initial estimate of the current profile. The implemented algorithm indicated improvement of this estimate when applied to simulated Doppler data.

From a large set of radar data collected from May 1975 through January 1978, several characteristics of the Bragg width were analyzed. This width (in units of current) was observed to vary with radar frequency f as $f^{-\alpha}$ (with $\alpha \approx 0.3$ to 0.5), and its dependence on radar pulsewidth, wind speed, or wind direction was much weaker--up to a few percent change for the various conditions encountered.

This research has shown that HF backscatter with average RF power of a few watts can probe the radial component of horizontal current and its distribution with depth in an ocean patch tens of kilometers away. Resolutions of a few cm/sec can be obtained during time intervals of a few minutes in an ocean patch of linear dimension on the order of kilometers. The current component orthogonal to the radar beam can be monitored by a similar radar deployed at a different location. The ocean surface can be scanned by range gating and beam steering to achieve simultaneous coverage of large areas. These features of the radio technique are very attractive when compared to conventional oceanographic measurements.

B. Recommendations

The radar system considered here employed a fixed beam. To map ocean current within a full 180° field of view, the radar has been modified to receive the signal on an array of eight loop antennas, and data have been collected by this new system [Teague et al, 1978]. A challenging area of research is in devising an optimal scheme for combining the signals on the eight antennas so that the antenna beam can be steered. Beam forming by conventional spatial Fourier transform and by maximum entropy [Burg, 1975] should be compared. The method first suggested by Crombie [1972] and extended by Barrick [1976] to determine the angle of arrival by comparing the phases of signals from the various receiving-array antennas is also applicable here.

To further understand air/sea interactions, it is desirable to measure the distribution of ocean current with depth, especially when the prevailing wind speed is high (over 20 knots). Such data did not become available partly because of the prevailing weather conditions on the California coast during the experiments and partly because of the difficulty in handling the rhombic transmit antenna during high winds. The new system described by Teague [1978] replaces the balloon-supported rhombic antenna with vertical whips supported by a fixed mast. The radar system can now operate in high winds and obtain current-shear measurements as a function of wind conditions.

In this work, it was assumed that the variation of ocean current in the horizontal plane could be ignored. This assumption is violated when the scale of variation is comparable to or smaller than the wavelength of the ocean waves. To incorporate the effects of such horizontal current structures into the dispersion relation, tedious derivations are required; however, the results may account for part of the Bragg-line broadening phenomenon.

Appendix A

DEGREE OF FREEDOM OF HAMMING-WINDOWED SPECTRAL ESTIMATOR

Consider a real-time series $s(t)$ of duration T . Assume that $s(t)$ is a zero mean stationary process with an autocovariance function $\gamma(u)$ defined as

$$\gamma(u) = E[s(t) s(t + u)]$$

Denote the time window by $q(t)$. This function is zero outside the interval $[-T/2, T/2]$. The windowed power spectral density estimator $P(f)$ at frequency f is

$$P(f) = \frac{1}{T} \left| \int s(t) q(t) \exp(-i2\pi ft) dt \right|^2$$

The integration limits $[-\infty, \infty]$ are assumed. Taking the ensemble average,

$$\begin{aligned} E[P(f)] &= \frac{1}{T} \iint E[s(t) s(t')] q(t) q(t') \exp[-i2\pi f(t - t')] dt dt' \\ &= \int \gamma(u) \hat{w}(u) \exp(-i2\pi fu) du \end{aligned} \quad (\text{A.1})$$

where

$$\hat{w}(u) = \frac{1}{T} \int q(t) q(t - u) dt$$

The above manipulations establish the relationship between the lag window $w(u)$ used by Jenkins and Watts [1968] and the time window $q(t)$. By comparing Eq. (A.1) to their equations (6.3.28) and (6.3.29), it can be seen that $w(u)$ is simply $\hat{w}(u)$ normalized by $\hat{w}(0)$. The equivalent degree of freedom ν can be computed, therefore, by using their equation (6.4.17),

$$\nu = \frac{2T}{I}$$

where

$$I = \frac{\int \hat{w}^2(u) du}{\hat{w}^2(0)}$$

The Hamming window is a complete cycle of a cosine waveform on an 8 percent pedestal,

$$q(t) = \begin{cases} 0.54 + 0.46 \cos (2\pi t/T) & |t| < T/2 \\ 0 & \text{otherwise} \end{cases}$$

The equivalent lag window $\hat{w}(u)$ can thus be calculated by numerical integration, and the degree of freedom for the Hamming window is approximately 4.

Appendix B

SPAR-BUOY DRIFT IN A CURRENT THAT VARIES WITH DEPTH

The following analysis is based on the work of Bye [1965]. It is included here for completeness.

Let ℓ be the depth of immersion of the spar buoy and $U(z)$ be the horizontal current that varies with depth z below the ocean surface. Assume that the buoy will drift along with the current at a speed denoted by U_D .

For the type of flow here, the Reynold number is on the order of a few thousand, and the drag coefficient is independent of the velocities involved over this range [Kaufmann, 1963]. The drag force acting on any part of the spar buoy is thus proportional to $[U_D - U(z)]^2$, with a sign that follows the sign of $[U_D - U(z)]$.

For the buoy to remain in a vertical position (stable equilibrium), the drag force should distribute itself so that its effect on the buoy is zero. In this event, there must be a critical depth z_c within the interval $[0, \ell]$ at which the drag force is zero; in other words,

$$U(z_c) = U_D \quad (\text{B.1})$$

The requirement for equilibrium can thus be written as

$$\int_0^{z_c} [U_D - U(z)]^2 dz - \int_{z_c}^{\ell} [U_D - U(z)]^2 dz = 0 \quad (\text{B.2})$$

whose solutions are sought for both the linear and logarithmic profiles.

If the profile is linear $[U(z) = U_0 + \alpha z]$, direct substitution into Eq. (B.2) yields

$$\int_0^{z_c} (z_c - z)^2 dz = \int_{z_c}^{\ell} (z_c - z)^2 dz$$

or

$$z_c^3 = (\ell - z_c)^3$$

The obvious solution is $z_c = \ell/2$. (The other two solutions are imaginary.) For a linear current profile, therefore, the buoy drifts with a velocity equal to the current at a depth one-half of its immersed length.

If the profile is logarithmic [$U(z) = U_0 + U_1 \cdot \ln(z)$], direct substitution into Eq. (B.2) results in

$$\int_0^{z_c} \ln^2 \left(\frac{z_c}{z} \right) dz = \int_{z_c}^{\ell} \ln^2 \left(\frac{z_c}{z} \right) dz$$

which, if $r = z/z_c$ and $r_0 = \ell/z_c$, becomes

$$\int_0^{z_c} \ln^2(r) dr = \int_{z_c}^{\ell} \ln^2(r) dr$$

Two integrations by parts obtain

$$\frac{4}{r_0} = \ln^2(r_0) \left[\ln(r_0) - 2 \right] + 2$$

Solving by successive iterations, $r_0^{-1} = 0.2725$ or $z_c = 0.2725 \ell$. For a logarithmic current profile, therefore, the buoy drifts with a velocity equal to the current at a depth slightly over one-fourth of its immersed length.

Appendix C

PARSEVAL'S THEOREM AND ITS EXTENSIONS

Given a signal $s(t)$ in the time interval $[-T/2, T/2]$, a conventional assumption used in deriving its discrete Fourier transform (DFT) is that it repeats itself outside this interval. Based on this assumption, the signal can be written as a Fourier series with a fundamental frequency $\Delta_f = T^{-1}$. The sampling frequency f_s is assumed to be larger than twice the bandwidth of $s(t)$. Within the Nyquist frequency interval of $[-f_s/2, f_s/2]$, therefore, the Fourier series coefficients a_n are the same as the DFT coefficients $S(n\Delta_f)$, and the summations below are restricted to this interval. As a result,

$$s(t) = \sum_n S(n\Delta_f) \exp(i2\pi n\Delta_f t)$$

and

$$S(n\Delta_f) = \frac{1}{T} \int s(t) \exp(-i2\pi n\Delta_f t) dt$$

where the integration limits are assumed to be from $-T/2$ to $T/2$.

Parseval's theorem relates the energy in $s(t)$ to that in the DFT coefficients. The average energy in $s(t)$ is

$$T^{-1} \int |s(t)|^2 dt = T^{-1} \int dt \sum_{m,n} S(m\Delta_f) S^*(n\Delta_f) \exp[i2\pi(m-n)\Delta_f t]$$

where $*$ denotes the complex conjugate. Because the complex exponentials $\exp(i2\pi m\Delta_f t)$ (m is an integer) are orthogonal in $[-T/2, T/2]$, Parseval's theorem

$$T^{-1} \int |s(t)|^2 dt = \sum_n P(n\Delta_f)$$

follows, where $P(n\Delta_f) = |S(n\Delta_f)|^2$ is the power spectral density.

A second theorem relates the first moment of the power spectrum to an integral in the time domain. If differentiation with respect to time t is denoted by a prime, then

$$iT^{-1} \int s(t) s^{*'}(t) dt = T^{-1} \int dt \sum_{m,n} 2\pi n \Delta_f S(m\Delta_f) S^{*'}(n\Delta_f) \exp[i2\pi(m-n)\Delta_f t]$$

by direct manipulation of the Fourier expansion of $s(t)$. Again using the orthogonal relationship for the complex exponentials,

$$\sum_m m \Delta_f P(m\Delta_f) = (2\pi T)^{-1} \int i s(t) s^{*'}(t) dt$$

A third theorem relates the second moment of the power spectrum to an integral in the time domain. The following relation can be obtained from the above type of manipulations:

$$\sum_n (n\Delta_f)^2 P(n\Delta_f) = (2\pi)^{-2} T^{-1} \int s'(t) s^{*'}(t) dt$$

Appendix D

RELATIONSHIP BETWEEN THE WINDOWED TRANSFORMS OF A FUNCTION AND ITS DERIVATIVE

Let the function be $f(x)$ and define the windowed Fourier transform of its derivative $f'(x)$ by

$$F_1(s) = \int w(x) f'(x) \exp(-isx) dx$$

Here, the window is assumed to be zero outside the interval $[-L/2, L/2]$. The integration interval $[-\infty, \infty]$ is assumed. Integrating by parts,

$$\begin{aligned} F_1(s) &= w(x) f(x) \exp(-isx) \Big|_{-\infty}^{+\infty} \\ &\quad + is \int w(x) f(x) \exp(-isx) dx \\ &\quad - \int w'(x) f(x) \exp(-isx) dx \end{aligned}$$

The first term is zero because the window function $w(x)$ is nonzero only in $[-L/2, L/2]$. The third term is negligible compared to the second because the width of $w(x)$ is large compared to the wavelength $2\pi/s$ of the complex sinusoid. As a result,

$$F_1(s) = isF(s)$$

where $F(s)$ is the windowed Fourier transform of $f(x)$.

BIBLIOGRAPHY

- Abramowitz, M. and I. A. Stegun, Handbook of Mathematical Functions, National Bureau of Standards, Applied Math. Series No. 55, Washington, D.C., 1964.
- Barnum, J. R., J. W. Maresca, and S. M. Serebreny, "High-Resolution Mapping of Oceanic Wind Fields with Skywave Radar," IEEE Trans. on Antenna Propagation, AP-21, pp. 680-685, 1977.
- Barrick, D. E., "The Interactions of HF/VHF Radiowaves with the Sea Surface and Its Implications in Electromagnetics of the Sea," AGARD Conf. Proc. No. 77, pp. 18-1 to 18-25, 1970.
- Barrick, D. E., "Remote Sensing of Sea State by Radar," in Remote Sensing of the Troposphere (V. E. Derr, ed.), Chapter 12, US Government Printing Office, Washington, D.C., 1972.
- Barrick, D. E., J. M. Headrick, R. W. Bogle, and D. D. Crombie, "Sea Backscatter at HF: Interpretation and Utilization of the Echo," Proc. IEEE, 62, pp. 673-680, 1974.
- Barrick, D. E. and M. W. Evans, "Implementation of Coastal Current-Mapping HF Radar System Progress Report No. 1," NOAA Technical Report ERL 373-WPL 47, Jul 1976.
- Barrick, D. E., "Extraction of Wave Parameters from Measured HF Radar Sea Echo Doppler Spectra," Radioscience, 12, 1977a.
- Barrick, D. E., M. W. Evans, and B. L. Weber, "Ocean Surface Currents Mapped by Radar," Science, 198, pp. 138-144, 1977b.
- Barrick, D. E. and B. L. Weber, "On the Nonlinear Theory for Gravity Waves on the Ocean's Surface, Part II: Interpretation and Applications," J. Phys. Oceanogr., 7, pp. 11-21, 1977c.
- Barrick, D. E., "HF Surface-Current Mapping Radar 1977 Alaskan Operations - Lower Cook Inlet," Preliminary Report, 1978a.
- Barrick, D. E., "Parameter Extraction Accuracy from Random HF Sea-Echo Doppler Spectral Samples," to be published, 1978b.
- Batchelor, G. K., An Introduction to Fluid Mechanics, Cambridge University Press, London, p. 264, 1970.
- Bellman, R., R. E. Kalaba, and J. A. Lockett, Numerical Inversion of the Laplace Transform, American Elsevier Publishing Co., New York, Chapters Two and Five, 1966.
- Born, M. and E. Wolf, Principles of Optics (fifth edition), Pergamon Press, New York, Appendix IV, 1975.

- Brillouin, L., Wave Propagation in Periodic Structures (2nd edition), Dover Publications, New York, Chapter 4, 1953.
- Burg, J. P., "Maximum Entropy Spectral Analysis," Ph.D. dissertation, Department of Geophysics, Stanford University, Stanford, Calif., May 1975.
- Bye, J. A. T., "Wind-Driven Circulation in Unstratified Lakes," Limnology and Oceanography, 10, pp. 451-458, 1965.
- Carrier, G. F., M. Krook, and C. E. Pearson, Functions of a Complex Variable, McGraw-Hill Book Co., New York, 1966.
- Crombie, D. D., "Doppler Spectrum of the Sea Echo at 13.56 Mc/s," Nature, 175, pp. 681-682, 1955.
- Crombie, D. D., "Resonant Backscatter from the Sea and Its Application to Physical Oceanography," Proc. IEEE Ocean 1972 Conf., pp. 174-179, 1972.
- Dahlquist, G. and A. Bjorck, Numerical Methods (translation by N. Anderson), Prentice-Hall, Englewood Cliffs, N.J., Chapter 5, 1974.
- Harris, F. J., "On the Use of Windows for Harmonic Analysis with the Discrete Fourier Transform," Proc. IEEE, 66, 1978.
- Helstrom, C. W., Statistical Theory of Signal Detection, Pergamon Press, New York, pp. 32-37, 1960.
- Huang, N. E. and C. Tung, "The Dispersion Relation for a Nonlinear Random Gravity Wave Field," J. Fluid Mech., 75, pp. 337-345, 1976.
- Jenkins, G. M. and D. G. Watts, Spectral Analysis and Its Applications, Holden-Day Press, San Francisco, 1968.
- Johnstone, D. L., "Second-Order Electromagnetic and Hydromagnetic Effects in High Frequency Radiowave Scattering from The Sea," Tech. Rept. SEL-75-004, Radioscience Laboratory, Stanford University, Stanford, Calif., 1975.
- Kaufmann, W., Fluid Mechanics, McGraw-Hill Book Co., New York, p. 290, 1963.
- Kinsman, B., Wind Waves: Their Generation and Propagation on the Ocean Surface, Prentice-Hall, Englewood Cliffs, N.J., 1965.
- Lamb, H., Hydrodynamics, Cambridge University Press, London, 1932.
- Lanczos, C., Applied Analysis, Prentice-Hall, Englewood Cliffs, N.J., Chapter VI, 1956.
- Lipa, B., "Inversion of Second-Order Radar Echoes from the Sea," J. Geophys. Res., 83, 1978.

- Lisitzin, E., Sea Level Changes, Elsevier Scientific Publishing Co., p. 36, 1974.
- Longuet-Higgins, M. S. and O. M. Phillips, "Phase Velocity Effects in Tertiary Wave Interactions," J. Fluid Mech., 12, pp. 333-336, 1962.
- Longuet-Higgins, M. S., D. E. Cartwright, and N. D. Smith, "Observation of the Directional Spectrum of Sea Waves Using the Motions of a Floating Buoy," in Ocean Wave Spectra, Prentice-Hall, Englewood Cliffs, N.J., pp. 111-132, 1961.
- Long, A. E. and D. B. Trizna, "Mapping of North Atlantic Winds by HF Radar Sea Scatter Interpretation," IEEE Trans. on Antenna Propagation, AP-21, pp. 680-685, 1973.
- Phillips, D. L., "A Technique for the Numerical Solution of Certain Integral Equations of the First Kind," J. ACM, 9, pp. 84-97, 1962.
- Phillips, O. M., The Dynamics of the Upper Ocean, Cambridge University Press, London, 1966.
- Phillips, O. M., private communication.
- Rabiner, L. R. and B. Gold, Theory and Application of Digital Signal Processing, Prentice-Hall, Englewood Cliffs, N.J., 1975.
- Rice, S. O., "Reflection of Electromagnetic Waves from Slightly Rough Surfaces," Comm. Pure Appl. Math., 4, 1951.
- Shemdin, O. H., "Wind-Generated Current and Phase Speed of Wind Waves," J. Phys. Oceanogr., 2, pp. 411-419, 1972.
- Squires, H. B., "On the Stability of the Three-Dimensional Disturbances of Viscous Flow between Parallel Walls," Proc. Roy. Soc., 142, pp. 621-628, 1933.
- Stewart, R. H. and J. W. Joy, "HF Radio Measurement of Surface Currents," Deep Sea Research, 21, pp. 1039-1049, 1974.
- Stewart, R. H., private communication.
- Stokes, G. G., "On the Theory of Oscillatory Waves," Trans. Cambridge Phil. Soc., 8, pp. 441-445, 1847.
- Sverdrup, H. U., M. W. Johnson, and R. H. Fleming, The Oceans, Prentice-Hall, Englewood Cliffs, N.J., 1942.
- Teague, C. C., G. L. Tyler, and R. H. Stewart, "The Radar Cross Section of the Sea at 1.95 MHz: Comparison of In-Situ and Radar Determinations," Radioscience, 10, pp. 847-852, 1975.
- Teague, C. C. and R. H. Stewart, JASIN Cruise Report, Joint HF Radar/Wave Buoy Experiments, Sep 1978.

- Twomey, S., "On the Numerical Solution of Fredholm Integral Equations of the First Kind by the Inversion of Linear Systems Produced by Quadrature," J. ACM, 10, pp. 97-101, 1963.
- Tyler, G. L., C. C. Teague, R. H. Stewart, A. M. Peterson, W. H. Munk, and J. W. Joy, "Wave Directional Spectra from Synthetic Aperture Observations of Radio Scatter," Deep Sea Research, 21, pp. 989-1016, 1974.
- Weber, B. L. and D. E. Barrick, "On the Nonlinear Theory for Gravity Waves on the Ocean's Surface, Part I: Derivations," J. Phys. Oceanogr., 7, pp. 3-10, 1977.
- Westwater, E. R. and O. N. Strand, "Inversion Techniques," in Remote Sensing of the Troposphere (V. E. Derr, ed.), US Government Printing Office, Washington, D.C., Chapter 16, 1972.
- Wu, J., "Wind-Induced Drift Currents," J. Fluid Mech., 68, pp. 49-70, 1975.